



Multiscale modeling of granular materials in application to geotechnical engineering problems

Hao Xiong

► To cite this version:

Hao Xiong. Multiscale modeling of granular materials in application to geotechnical engineering problems. Mechanics of materials [physics.class-ph]. Université Grenoble Alpes, 2017. English. NNT : 2017GREAI096 . tel-02314614

HAL Id: tel-02314614

<https://theses.hal.science/tel-02314614>

Submitted on 13 Oct 2019

HAL is a multi-disciplinary open access archive for the deposit and dissemination of scientific research documents, whether they are published or not. The documents may come from teaching and research institutions in France or abroad, or from public or private research centers.

L'archive ouverte pluridisciplinaire **HAL**, est destinée au dépôt et à la diffusion de documents scientifiques de niveau recherche, publiés ou non, émanant des établissements d'enseignement et de recherche français ou étrangers, des laboratoires publics ou privés.

Multiscale modeling of granular materials in application to geotechnical engineering problems



Hao Xiong

IRSTEA

Université Grenoble Alpes

This dissertation is submitted for the degree of

Doctor of Civil Engineering

October 2017

Abstract

Granular materials exhibit a wide spectrum of constitutive features when submitted under various loading paths. Developing constitutive models which succeed in accounting for these features has been challenged by scientists for decades. A promising direction for achieving this can be the multi-scale approach. Through this approach, the constitutive model is formulated by relating material's macroscopic properties to their corresponding microstructure properties.

This thesis proposes a three-dimensional micro-mechanical model (the so-called 3D-H model) taking into account an intermediate scale (meso-scale) which makes it possible to describe a variety of constitutive features in a natural way. The comparison between experimental tests and numerical simulations reveals the predictive capability of this model. Particularly, several simulations are carried out with different confining pressures and initial void ratios, based on the fact that the critical state is quantitatively described without requiring any critical state formulations and parameter. The model is also analyzed from a microscopic view, wherein the evolution of some key microscopic parameters is investigated.

Then, a 3D multi-scale approach is presented to investigate the mechanical behavior of a macroscopic specimen consisting of a granular assembly, as a boundary value problem. The core of this approach is a multiscale coupling, wherein the finite element method is used to solve a boundary value problem and the 3D-H model is employed to build the micro constitutive relationship used at a representative volume element scale. This approach

provides a convenient way to link the macroscopic observations with intrinsic microscopic mechanisms. Plane-strain biaxial loading conditions are selected to simulate the occurrence of strain localization. A series of tests are performed, wherein distinct failure patterns are observed and analyzed. A system of shear band naturally appears in a homogeneous setting specimen. By defining the shear band area, microstructural mechanisms are separately investigated inside and outside the shear band. Moreover, a second-order work directional analysis is performed by applying strain probes at different stress-strain states along drained biaxial loading paths. The normalized second order work introduced as an indicator of an unstable trend of the system is analyzed not only on the macroscale but also on the microscale.

Finally, a second order work analysis in application to geotechnical problems by using the aforementioned multiscale approach is presented. The multiscale approach is used to simulate a homogeneous and a non-homogeneous BVP, opening a road to interpret and understand the micro mechanisms hiding behind the occurrence of failure in geotechnical issues. This multiscale approach utilizes an explicit-dynamic integral method so that the post-peak failure can be investigated without requiring over-sophisticated mathematical ingredients. Thus, by switching the loading method from a strain control to a stress control at the limit state, the collapse of the system can be reflected in an abrupt increase of kinetic energy, stemming from the difference between both internal and external second-order works.

Keywords: Constitutive modeling, Meso-scale, Multiscale, Micro-structure, Finite element method, Instability, Strain localization, Shear band, Second-order work

Résumé

Les matériaux granulaires présentent une large gamme de lois de comportement lorsqu'ils sont soumis à différents chemins de chargement. Le développement de modèles constitutifs permettant de rendre compte de ces caractéristiques a été une préoccupation constante de nombreux chercheurs depuis des décennies. Parmi les différentes options possibles, les approches par changement d'échelle semblent prometteuses. Dans ces approches, le modèle constitutif est formulé en reliant les propriétés macroscopiques du matériau aux propriétés micro-structurelles correspondantes.

Cette thèse propose un modèle micromécanique tridimensionnel (le modèle H-3D) prenant en compte une échelle intermédiaire (méso-échelle). Il permet ainsi de décrire de manière naturelle un grand nombre de caractéristiques constitutives des matériaux granulaires non cohésifs. La comparaison entre essais expérimentaux et simulations numériques révèle la capacité prédictive de ce modèle. En particulier, des simulations réalisées avec différentes pressions de confinement et différents rapports de vide initiaux ont permis de démontrer la capacité du modèle à rendre compte quantitativement de l'état critique sans nécessiter d'équation spécifique et de paramètre d'état critique. Le modèle est également analysé à l'échelle microscopique, où l'évolution de certains paramètres microscopiques clés est présentée.

Une approche multi-échelle 3D est ensuite présentée afin d'étudier le comportement mécanique d'un échantillon macroscopique constitué d'un assemblage granulaire, en tant que

problème aux conditions limites. Le cœur de cette approche est un couplage multi-échelle, où la méthode des éléments finis est utilisée pour résoudre le problème aux conditions limites et le modèle H-3D est utilisé pour calculer la loi de comportement à l'échelle d'un volume élémentaire représentatif. Cette approche fournit un moyen pratique de relier les observations macroscopiques avec les mécanismes microscopiques intrinsèques. Des conditions de chargement biaxiaux en déformations planes sont appliquées pour simuler le phénomène de localisation des déformations. Une série de tests est effectuée, où différents motifs de rupture sont observés et analysés. Un système de bande de cisaillement apparaît naturellement dans un spécimen initialement homogène. En définissant la zone de la bande de cisaillement, les mécanismes microstructuraux sont étudiés séparément à l'intérieur et à l'extérieur de celle-ci. En outre, une analyse directionnelle de travail du second ordre est effectuée en appliquant des petits incréments de contrainte à différents états de contrainte-déformation sur des chemins de chargement biaxiaux drainés. Le travail de second ordre normalisé, introduit comme un indicateur d'instabilité du système, est analysé non seulement à l'échelle macroscopique mais aussi à l'échelle microscopique.

Enfin, une analyse du travail de second ordre appliquée à des problèmes géotechniques et utilisant l'approche multi-échelle développée dans cette thèse est présentée. L'approche multi-échelle est utilisée afin de simuler des problèmes aux conditions limites homogènes et non homogènes, offrant ainsi la possibilité d'interpréter et de comprendre les micro-mécanismes qui à l'origine des phénomènes de rupture dans les problèmes géotechniques. Cette approche multi-échelle utilise un schéma numérique d'intégration dynamique-explicite afin de pouvoir étudier la rupture post-pic sans avoir à recourir à des outils mathématiques trop sophistiqués. Ainsi, en changeant le type de condition de chargement de déplacement à contrainte lorsque le système atteint son état limite, son effondrement se traduit par une augmentation soudaine de l'énergie cinétique découlant de la différence entre les travaux internes et externes du second ordre.

Mots clés: Loi de comportement, Méso-échelle, Multi-échelle , Microstructure, Méthode des éléments finis, instabilité, localisation de la déformation , bande de cisaillement, travail du second ordre

Contents

List of Figures	xv
List of Tables	xxi
1 General introduction	1
1.1 Motivation	2
1.2 Objectives	3
1.3 Methodology	4
1.4 Thesis outline	5
2 Background literature	9
2.1 Overall behavior of granular materials	10
2.1.1 Contractancy and dilatancy	10
2.1.2 Hardening and softening	12
2.1.3 Anisotropy	14
2.2 Micro-structure analysis in granular materials	15
2.2.1 Fabric	15

2.2.2	Force-chain	18
2.2.3	Meso-loops	20
2.3	Instability in granular materials	21
2.3.1	Experimental observations	22
2.3.2	Theoretical advances	27
2.4	Constitutive modeling of granular materials	30
2.5	Concluding remarks	34
3	An extended micromechanically-based model for granular materials	37
3.1	Reviews of the micro-directional models	38
3.1.1	The micro-directional model	39
3.1.2	From the micro-directional model to the H-model	42
3.1.3	The H-microdirectional model (H-model)	43
3.2	A 3D extension of the H-model	48
3.2.1	Kinematic localization	48
3.2.2	Meso-structure behavior	51
3.2.3	Stress averaging	55
3.2.4	Opening angle and void ratio	56
3.3	Performances of the 3D-H model	58
3.3.1	Parameter calibration and model prediction	58
3.3.2	Triaxial loading paths	60
3.4	Closing remarks	67

4	Finite element implementation of the 3D-H model	71
4.1	The Finite Element Method	72
4.2	Multi-scale approach implementation	75
4.3	Finite Element Model and benchmark	76
4.3.1	Finite Element Model	76
4.3.2	Calibration and verification	79
4.3.3	Mesh dependency	79
4.4	Drained triaxial tests	83
4.4.1	Model performance	83
4.4.2	Phases transition: from homogeneity to inhomogeneity	87
4.4.3	Inside and outside shear band	92
4.5	Directional analysis of second-order work	96
4.6	Closing remarks	101
5	Engineering applications based on the second-order work criterion	105
5.1	Second-order work criterion	106
5.2	Numerical applications	108
5.2.1	Laboratory test	108
5.2.2	Geotechnical engineering problem	113
5.3	Closing remarks	122
6	Conclusions and recommendations	125
6.1	Conclusions	126

6.1.1	Constitutive modeling of granular materials by considering microstructure	126
6.1.2	Finite element implementation procedure	128
6.1.3	The occurrence of strain localization	129
6.1.4	Simulation of geotechnical boundary value problems	130
6.2	Recommendations	132
Bibliography		135
Appendix A Detailed formulation in the 3D-H model		149
A.1	Inter-particle contact law	149
A.2	Stiffness matrix on the mesoscopic scale	150
Appendix B Abaqus and VUMAT		153
B.1	Framework	153
B.2	User Subroutine: VUMAT	155

List of Figures

2.1	Force chain and meso-loops	21
2.2	Localized strain under plane strain conditions: (a) Soil specimen before compression, (b) Deformed specimen after 9.6% and 19% axial strain (after (Alshibli et al., 2003))	23
2.3	Localized strain under triaxial drained compression: (a) Soil specimen at 25% axial strain, (b) CT scans at 25% axial strain (after (Alshibli et al., 2003))	23
2.4	Experimental results on dense Hostun sand for biaxial drained tests at different confining pressures (after (Desrues and Viggiani, 2004)).	25
2.5	Experimental results from several undrained triaxial compression tests for different initial void ratios (after (Chu et al., 2003)).	27
2.6	Principle of simple critical-state based model of sand (after (Wu et al., 2017)).	30
3.1	General homogenization scheme of the micro-directional model (Cambou et al., 1995).	40
3.2	The hexagonal element of the H-directional model.	45
3.3	Mechanical description of hexagon pattern.	46
3.4	Global and local coordinate systems.	49

3.5	The meso-structure of 3D-H model.	50
3.6	Mechanical description of hexagon pattern A.	52
3.7	Mechanical description of hexagon pattern B.	53
3.8	Evolution of initial void ratio as a function of initial opening angle.	57
3.9	Calibration phase of the model at 200 kPa of confining pressure.	59
3.10	Prediction capability of the model at 100 kPa and 300 kPa of confining pressures.	60
3.11	Effect of different initial confining pressures on model responses along an axisymmetric drained triaxial loading path.	62
3.12	Effect of different initial void ratios on the model response along an axisymmetric drained triaxial loading path.	63
3.13	Angular distributions of micro variables along θ at different strain states, with 200 kPa of the confining stress: the integrated micro stress $\iint \omega \tilde{\sigma}_n d\theta d\psi$, $\iint \omega \tilde{\sigma}_t d\theta d\psi$ and $\iint \omega \tilde{\sigma}_w d\theta d\psi$ (N) (left column); the percentage of plastic or buckling meso-structures (center column); the mean normalized of the opening angles $(\alpha_1/\alpha_0, \alpha_2/\alpha_0)$ (right column).	66
4.1	The schematic diagram of multi-scale approach based on the 3D H-model. .	77
4.2	Different scales involved in the multi-scale approach.	77
4.3	Model constraints and element type.	78
4.4	Parameters calibration and model verification using the triaxial compression test on Ticino sand ($D_R = 74\%$).	80
4.5	Mechanical response with different mesh patterns under the drained triaxial loading path at 200 kPa of confining stress.	81

4.6	Contours plotting of element strain ε_2 for the deformed configuration at the axial strain $\varepsilon_a = 6\%$	82
4.7	Failure patterns on deformed configuration in terms of ε_2 for distinct boundary conditions (T1-T4).	85
4.8	Failure patterns on deformed configuration in terms of ε_2 for distinct imperfection positions (T5-T8).	86
4.9	Mechanical response with different confining stresses for test T1.	88
4.10	Failure patterns on deformed configuration in terms of ε_2 for different confining stresses in test T1.	88
4.11	Mechanical and volumetric responses with different initial void ratios for test T1.	89
4.12	Failure patterns on deformed configuration in terms of ε_2 for different initial void ratios in test T1.	90
4.13	Mechanical and volumetric responses for all elements in the mesh.	91
4.14	The maps of normalized second-order work W_{2n} for the deformed configuration at different states (see Figure 4.13).	93
4.15	The maps of kinetic energy E_k (J) for the deformed configuration at different states corresponding to Figure 4.13	93
4.16	Shear band definition.	95
4.17	Evolution of the volumetric strain ε_v (%) and the second-order work W_2 (J) with respect to the overall axial strain ε_a (%) for test T1.	97
4.18	Strain probes and stress responses.	98

4.19	Mechanical and volumetric responses of T1 under triaxial loading at 200 kPa of confining stress.	99
4.20	Polar diagram of normalized W_{2n} in incremental stress space and strain space using strain probes at different loading states with 200 kPa of cofinning stress.	100
4.21	Angular distributions of micro variables when the strain probes are applied at 2% of axial strain.	102
5.1	Mesh, element type and boundary conditions for the 3D cylinder specimen.	110
5.2	Mechanical and volumetric responses for a 3D cylinder specimen and strain fields (ϵ_3) at the selected states $\epsilon_a = 2.7\%, 7\%, 8\%$ and 9% along a drained triaxial loading path under a confining pressure of 200kPa.	111
5.3	1	111
5.4	1	111
5.5	Evolution of external and internal second-order works versus axial strain ϵ_a (%) for a 3D cylinder specimen.	112
5.6	Evolution of kinetic energy E_c (J) versus axial strain ϵ_a (%) for 3D cylinder specimen.	113
5.7	Mesh, element type and boundary conditions for the footing problem. . . .	114
5.8	Undeformed mesh with geo-stress distribution at the end of geo-static stage.	115
5.9	Evolution of the vertical reaction force R_f (kN) versus the footing settlement normalized by the footing width d/B (%).	116
5.10	Displacement field $ \vec{u} $ at the state $d/B = 8\%$	116
5.11	Deformed meshes with distribution of plastic strain (ϵ_p) at different states: $d/B = 1\%, 2\%, 4\%$ and 8%	117

5.12	Evolution of internal and external second-order works versus the footing settlement normalized by the footing width d/B (%).	118
5.13	Evolution of kinetic energy E_c (kJ) of the whole system versus the footing settlement normalized by the footing width d/B (%).	119
5.14	Deformed meshes with normalized internal second-order work distribution at the state $d/B = 8\%$.	120
5.15	Evolution of deviatoric stress ratio versus normalized footing settlement corresponding to selected Gauss points seen in Figure 5.7 .	121
B.1	Abaqus framework.	154
B.2	User-material subroutine interface in FORTRAN language.	156

List of Tables

- 3.1 Parameters selected in calibration and prediction phases 59
- 4.1 Parameters selected in calibration and prediction phases 79
- 4.2 Imperfection positions and boundary conditions of different tests. 83
- 4.3 Schematic diagram of imperfection positions and boundary conditions given
in [Table 4.2](#). 84

Chapter 1

General introduction

With the development of human social civilization, the artificial structures in interaction with the soil are becoming more and more important. The soil, as a kind of porous granular material, is a significant material involved in various kinds of engineering, such as civil engineering, environmental engineering, mining engineering, shore engineering and etc. However, no fundamental theory is currently available to describe its properties. The behavior of one single grain is easily understood, but the properties of a granular collection are much more complex. Besides, the proper understanding of its behavior is essential to the formulation of realistic constitutive models and to the capturing of various failure patterns and instability modes in geomaterials. The main objective of this thesis is to contribute further to multiscale modeling of granular materials. Therefore, this thesis aims at developing a micromechanically-based constitutive model and at implementing this model within a multiscale approach in order to understand and investigate the complex phenomena taking place within granular materials.

1.1 Motivation

Granular materials, as a fundamental material involved in various engineering fields, experience a complex behavior, which is strongly influenced by loading history, initial density and microstructure evolution. Due to the complex behavior, a rich variety of deformational modes arises in granular materials including the well-known phenomena such as liquefaction, dilatancy, densification, diffuse and localized failure modes and instability. The notion of instability in mechanics has its origins back to the seminal work of (Hill, 1958), which raised the significantly theoretical issue as to the condition of material instability and beyond to the global (boundary value) level.

When granular materials are subjected to the external loading, various deformation modes can develop. For example, a sand specimen subjected to a drained triaxial loading path may either localize into shear bands or deform in a diffuse manner throughout its entire mass. In both cases, the problem underlies a material instability phenomenon that develops from initial disturbances of materially or spatially uniform regions of the granular material due to microstructural features on a small scale. Structural instability is in contrast related to external boundary effects rather than disturbances at the microstructure level. At such a microscale, mechanisms of energy dissipation and inter-granular force transmission lead to local instabilities that reflect at the larger macroscopic scale as shear dilatancy, localization of deformations and liquefaction, among others. Localization consists of different forms of concentrated deformations such as shear bands, compaction bands and dilation bands (Rice, 1976; Rudnicki and Rice, 1975; Sulem and Vardoulakis, 2004; Vardoulakis et al., 1978) or fractures where sharp discontinuities arise. These bands or strong discontinuities lead to an unstable response that is associated with a bifurcation problem triggered at or near plastic limit state.

1.2 Objectives

The main objective of this thesis is to contribute further to the study of the complex behavior of granular materials, especially from a multiscale point of view. As such, the intent of the present work is to propose a robust constitutive model, and thereafter implement it within a Finite Element Method, in which boundary value problems can be solved. Various aspects of the problem, such as those related to microstructure (fabric), propensity to stress-dilatancy and loading regime are addressed in order to evaluate their relationship to the occurrence of instability within granular materials. Thus, the specific objectives of this research are to:

- formulate an effective constitutive model by taking into account a meso-structure acting on an intermediate scale, linking the macro and micro scales, as an extension of the H-directional model earlier proposed by (Nicot and Darve, 2011b);
- calibrate the model parameter and examine the performance of the model in various of loading conditions at a material point level;
- implement the enhanced constitutive model within a finite element framework by using a multi-scale approach, where the finite element method is used to solve boundary value problem whereas the constitutive model applies at the Gauss points;
- analyze boundary value problems ranging from a lab specimen size to a field scale; and lastly
- analyze the instability occurrence of granular materials in geotechnical engineering problems by using the second-order work theory.

1.3 Methodology

As illustrated in many studies (Bagi, 1993; Krut and Rothenburg, 1996; Zhu, 2015), the evolution of material and force fabrics is significant for the macroscopic behavior of granular materials. In order to achieve the objective outlined above, a novel constitutive model called 3D-H model taken a meso-structure into account will be formulated under general three-dimensional conditions. This model is an extension of the H-microdirectional model earlier developed by (Nicot and Darve, 2011b). It is essential that such a model accounts for the complexity of not only the underlying granular material structure but also the deformation-loading process, for which the embedding meso-structure plays a significant role in the loading history, reflecting the local dilatancy and the rearrangement of the granular assembly. Particularly, the strong dependency of granular material behavior on mean stress, density and microstructure has to be properly addressed. Here, a model with adequate mechanical content is proposed, and because of the non-symmetry of the resulting constitutive tensor, a whole variety of material responses can be envisaged with the possible loss of uniqueness of solutions of the underlying constitutive equations. As a result, various types of bifurcations can be expected clearly before the plastic limit condition is reached.

The above-mentioned 3D-H model is then implemented within a finite element code called ABAQUS (see a brief view in Appendix B) by using a multiscale approach. A 3D multiscale approach is presented to investigate the mechanical behavior of a macroscopic specimen consisting of a granular assembly, as a boundary value problem. The core of this approach is a multiscale coupling, wherein the finite element method is used to solve a boundary value problem and the 3D-H model is employed to build the micro constitutive relationship used at a representative volume element scale. This approach provides a convenient way to link the macroscopic observations with intrinsic microscopic mechanisms.

It is now well established that the second-order criterion is convenient to detect and analyze the material instability occurrence. A certain class of instabilities, related to the occurrence of an outburst in kinetic energy, could be properly detected by the vanishing of the second-order work. Furthermore, the second-order work formalism was recently extended from the material point scale (or for homogeneous specimens under homogeneous loading conditions) to any material system. Both strain and stress fields may no longer be homogeneous such as for geotechnical engineering problems. A novel approach is employed in which internal and external second-order works are computed based on the mechanical parameters (forces, displacements) acting on the boundary of the system only, without requiring any internal information within the system.

1.4 Thesis outline

The thesis comprises three main parts: (1) developing a constitutive model, (2) implementing the constitutive model within a finite element code by using multiscale approach and (3) using this approach to analyze boundary value problems ranging over different scales. In terms of chapters, the work of the thesis is organized as below:

Chapter 2 conducts an extensive literature background on the behavior of granular materials, especially sands, and the instability-related phenomena in granular materials. The focus is on experimental and numerical analysis of localized and diffuse instability. On the other side, the necessity to investigate the micro-structure evolution and to develop the constitutive model for granular materials based on this evolution are emphasized at the beginning of this thesis.

Chapter 3 firstly reviews the micro-directional model (Nicot et al., 2005) and the H-directional model (Nicot and Darve, 2011b) in two-dimensional conditions. Based on the homogenization scheme of the H-directional model, a three-dimensional extension of the

H-directional model is developed. To examine the novel model capability, calibration is performed using drained triaxial experimental results from Ticino sand. Once calibrated, the performance of this 3D-H model is then analyzed in prediction. Afterwards, the model responses on confining stress dependent and void ratio dependent stress-strain relationships are examined, based on which the critical state seems naturally captured. Finally, the model mechanism is also inspected from a microscopic point of view. The evolution of micro variables is analyzed at different strain states along a drained triaxial loading path.

Chapter 4 presents a multi-scale approach, where the 3D-H model is implemented within an FEM code (ABAQUS), involving different scales spanning from microscale (grain scale) to macroscale (structure scale). Each cell of the finite element mesh represents a REV (intermediate scale). The 3D-H model acts on the elementary cell, to relate both local strain and stress by taking the microstructure (microscopic scale) into account. Afterwards, a series of drained biaxial tests are performed to analyze the occurrence of strain localization by considering a plane-strain problem. Finally, a directional analysis is performed at some selected material points of the BVPs, in order to carry out a stability analysis based on the vanishing of the second-order work.

Chapter 5 introduces the mathematical framework used for the stability analysis, in which the second-order work criterion is highlighted. Then, the effective multiscale approach presented in Chapter 4 is applied to analyze geotechnical BVPs. Two cases of BVPs are considered: a homogeneous specimen under homogeneous loading condition and a strip footing problem as a non-homogeneous BVP. The aforementioned second-order work criterion is applied to both cases to analyze the occurrence of instability. Finally, the stress-strain (force-displacement) relations are analyzed not only on the macro-scale but also at some selected Gauss points, highlighting the nature of failure mode (diffuse vs. localized failure).

Chapter 6 closes the thesis by pointing out the main findings of the research. Suggestions for further investigations are also made.

Chapter 2

Background literature

This chapter briefly introduces the most salient aspects of the behavior of granular materials. These characteristics include the contractancy-dilatancy, anisotropy and hardening-softening mechanisms from a macroscopic point of view. In contrast, the features include material and force fabrics, force-chain and meso-loops from a microscopic viewpoint. In addition, this chapter presents a short but rather comprehensive review on current and past works on instability from both experimental and theoretical viewpoints. Finally, this chapter highlights the importance of developing micromechanically-based constitutive models, as the macroscopic behavior stems essentially from microscopic features.

2.1 Overall behavior of granular materials

Granular materials, as the object of this thesis, can be defined as a collection of (sometimes) negligibly deformable particles whose microstructure is continuously evolving in terms of deformation under a given loading path. Engineers and scientists have been investigating granular material physics for centuries as evidenced by the pioneering works of (Reynolds, 1885) on particle interactions. Geomaterials, referring to granular materials like sand, show some unique deformation characteristics in the static limit, those include dilatancy, anisotropy, hardening-softening, shear localization and diffuse failure, to name a few (Guo, 2000; Zhu et al., 2006). This section briefly reviews some of these features that relate to the failure of geomaterials.

2.1.1 Contractancy and dilatancy

The notation of dilatancy includes negative dilatancy, which is also called contractancy. Dilatancy is the tendency of granular materials to change their volume at shear. This property, first considered by (Reynolds, 1885), is of great importance. It is worth noting that upon stress path reversal, dilatancy turns to contractancy which is of a magnitude larger than for the previous dilatancy. Dilatancy represents the coupling between shear and volumetric deformation mechanisms.

Dilatancy models usually start from a proposition as to the way in which plastic work is dissipated, (Taylor, 1956) analysis of direct shear box test of sand assumed that the entire input work is dissipated in friction. This principle of energy dissipation has been extended for the condition of triaxial tests by (Roscoe et al., 1963), gives:

$$\begin{aligned} p'd\epsilon_v^p + qd\epsilon_d^p &= Mp'd\epsilon_d^p && \text{for loading} \\ p'd\epsilon_v^p + qd\epsilon_d^p &= -Mp'd\epsilon_d^p && \text{for unloading} \end{aligned} \tag{2.1}$$

where $p' = (\sigma'_a + 2\sigma'_r)/3$ is the mean effective stress, $q = \sigma'_a - \sigma'_r$ is the deviatoric stress, and $d\varepsilon_v^p = d\varepsilon_a^p + 2d\varepsilon_r^p$ is the volumetric strain increment. The superscript p denotes plastic components, the deviatoric strain increment $d\varepsilon_d^p = 2(d\varepsilon_a^p - d\varepsilon_r^p)/3$, and the subscripts a and r indicate axial and radial directions, respectively, in a triaxial setup. M is the slope of critical state line.

The right-hand term of [Equations 2.1](#) represents the dissipation energy in friction, which must be positive in either loading or unloading tests. Note that the value of $d\varepsilon_d^p$ is positive in loading and negative in unloading condition. [Equations 2.1](#) can be rearranged to the form of dilatancy equation:

$$\begin{aligned} \frac{d\varepsilon_v^p}{d\varepsilon_d^p} &= M_c - \frac{q}{p'} && \text{for loading} \\ \frac{d\varepsilon_v^p}{d\varepsilon_d^p} &= -M_e - \frac{q}{p'} && \text{for unloading} \end{aligned} \quad (2.2)$$

where $M_c = 6 \sin \phi_0 / (3 - \sin \phi_0)$ and $M_e = 6 \sin \phi_0 / (3 + \sin \phi_0)$ are the stress ratio corresponding to zero dilatancy for loading and unloading, respectively, which is also termed as the slope of phase transformation line (Ishihara, 1983) or characteristic line (Luong, 1980). The parameter ϕ_0 is termed as the phase transformation angle.

(Rowe, 1962, 1969) assumed that the ratio of the input energy increment to the output energy increment is a constant, denoted as K . In a loading test, the input energy increment is $\sigma'_a d\varepsilon_a^p$ and the output energy increment is $2\sigma'_r d\varepsilon_r^p$, and vice versa for an unloading test. Hence,

$$\begin{aligned} \frac{\sigma'_a}{\sigma'_r} &= K \left(1 - \frac{d\varepsilon_v^p}{d\varepsilon_a^p} \right) && \text{for loading} \\ \frac{\sigma'_r}{\sigma'_a} &= \frac{1}{K} \left(1 - \frac{d\varepsilon_v^p}{d\varepsilon_a^p} \right) && \text{for unloading} \end{aligned} \quad (2.3)$$

Because of the variation of experimental tests, a constant D is often introduced in [Equations 2.2](#), such as that proposed by (Anandarajah, 2008; Gajo and Wood, 1999; Jefferies, 1997; Li et al., 1999; Nova and Wood, 1982):

$$\begin{aligned} \frac{d\varepsilon_v^p}{d\varepsilon_d^p} &= D \left(M_c - \frac{q}{p'} \right) && \text{for loading} \\ \frac{d\varepsilon_v^p}{d\varepsilon_d^p} &= D \left(-M_e - \frac{q}{p'} \right) && \text{for unloading} \end{aligned} \quad (2.4)$$

The value of D is different for loading and unloading case. It has also been suggested that the value of M is a function of density state (e.g. (Manzari and Dafalias, 1997)).

2.1.2 Hardening and softening

In the context of plasticity theory, strain softening under a three dimensional stress state can be defined as a contraction of the yield surface in stress space with continuous shearing. The concept can be expressed mathematically by the following equations, proposed by (Prevost and Hoeg, 1975):

$$d\varepsilon_{ij} = C_{ijkl}^e d\sigma'_{kl} + h \frac{\partial G}{\partial \sigma'_{ij}} \left(\frac{\partial f}{\partial \sigma'_{kl}} d\sigma'_{kl} \right) \quad (2.5)$$

where h is a parameter defined by [Equation 2.5](#) ($h > 0$ corresponds strain hardening, $h < 0$ corresponds strain softening); C_{ijkl}^e is the elastic stiffness tensor; G is the plastic potential function; and f is the yield function. h can be determined by the consistent condition $df = 0$.

However, the use of stress-space plasticity in modeling strain softening may present certain theoretical and analytical difficulties. To overcome these problems, (Casey and Naghdi, 1981) defined strain softening based on plasticity theory formulated in strain space. Based on (Casey and Naghdi, 1981), an elastoplastic material is said to be hardening, softening, or exhibiting perfectly plastic behavior during loading according to whether

$$\begin{aligned}
\frac{\hat{f}}{\hat{g}} &> 0, & \text{for hardening} \\
\frac{\hat{f}}{\hat{g}} &< 0, & \text{for softening} \\
\frac{\hat{f}}{\hat{g}} &= 0, & \text{for perfectly plastic}
\end{aligned} \tag{2.6}$$

where f and g are the yield functions defined in stress space and strain space respectively; and \hat{f} and \hat{g} are yield functions related parameters.

Definitions of strain softening based on [Equation 2.5](#) or [Equation 2.6](#) require an elasto-plastic constitutive model of the material as a priori. (Valanis, 1985) proposed the following definition for strain softening:

If ϵ_{ij} is a parametric representation of strain path in strain space and σ'_{ij} is the corresponding stress path in stress space, a material is said to be softening at a point on the strain path if, at this point $d\sigma'_{ij}d\epsilon_{ij} \leq 0$.

This definition possesses a number of advantages in terms of total strains instead of plastic strains; therefore the difficulties inherent in decomposing the measured total strain into elastic and plastic components (Lo and Lee, 1990) is avoided. The definition is given in incremental forms, hence it is dependent on the current directions of the stress- and strain increment vectors only. The definition can be used without referring to a specific constitutive model of soil. These features in this definition make it particularly suitable for investigating, experimentally, strain-softening response along a wide spectrum of strain paths. Thus, strain softening under axisymmetric conditions can be defined as:

$$\begin{aligned}
d\epsilon_s^p &> 0 \quad \text{and} \quad d\sigma'_{ij}d\epsilon_{ij} < 0 \\
\text{or} \\
d\epsilon_s^p &> 0 \quad \text{and} \quad dp'd\epsilon_v + dq d\epsilon_s < 0
\end{aligned} \tag{2.7}$$

The first inequality in [Equations 2.7](#) ensures that the sample has undergone a plastic deformation during strain softening. The second inequality of [Equations 2.7](#) degenerates into $dq < 0$

for $d\sigma'_3 = 0$, or $dp' = 0$ or undrained tests. Under strainpath tests, the second inequality of Equations 2.7 becomes:

$$dq < du \frac{d\varepsilon_v}{d\varepsilon_1} \quad (2.8)$$

where u is the pore water pressure. For $du > 0$ and $d\varepsilon_v/d\varepsilon_1 < 0$, the given inequality at least requires $dq < 0$. These conditions are consistent with the intuitive expectation of strain softening, as $dq < 0$ has been used to refer to strain softening in the past. The dominate considerations in choosing such a definition are in avoiding making assumptions a priori and the ability to reflect the influence, if any, of path on strain softening.

2.1.3 Anisotropy

In granular materials, particles are essentially assembled together through their spatial arrangement and the resultant contact force fabric. These determine the micro-structure of the material. Depending on the internal structure and distribution of contact normals, granular materials may exhibit anisotropic response when they are subjected to external loadings (Oda, 1972b,c). Two physical origins which give rise to this anisotropy can be usually identified: the first one, called *initial anisotropy* or *inherent anisotropy*, is linked to the usual deposit under the gravity of sedimentary soils; the second one, called *induced anisotropy* is related to the loading path applied to the material considered. Initial anisotropy is related to the preferred orientation of non-spherical particles and concentration of contact normals developed during the formation of the material. Induced anisotropy is developed by the material in order to accommodate with the loading path. It is evident that material anisotropy, or primarily material fabric, influences the deformation and strength properties of the granular materials, which establishes its connection to the stress-dilatancy phenomenon described before. These two kinds of anisotropy can be analyzed using global measurements

on the scale of the representative elementary volume. The effects of anisotropy can be analyzed on elastic and as well as non-reversible characteristics (Cambou et al., 2004). For example, (Hoque, 1996) has shown from experimental results performed on triaxial tests that vertical and horizontal elastic moduli could be expressed as follows:

$$\begin{aligned} E_V &= E_{V_0} \sigma_V^{n_V} \\ E_H &= E_{H_0} \sigma_H^{n_H} \end{aligned} \quad (2.9)$$

where σ_V (resp. σ_H) is the vertical (resp. horizontal) stress, E_V (resp. E_H) is the vertical (resp. horizontal) elastic modulus, n_V (resp. n_H) is a non-linear exponent (with values not so far from 0.5) and E_{V_0} and E_{H_0} are constants. Equation 2.9 shows clearly that for non-isotropic loading paths the elastic behavior of granular materials experiences very significant anisotropy.

2.2 Micro-structure analysis in granular materials

2.2.1 Fabric

A complete description of fabric in granular materials consists of two parts: one is the scalar description; another covers the anisotropic information.

Scalar fabric description

In the scalar fabric description part, there are two quantities, that are usually measured and formulated into many theories. The one familiar to the geotechnical engineers is the void ratio which is also an important state parameter in critical state soil mechanics (CSSM) (Li and Dafalias, 2011). Another is the coordination number Z . In most cases, the coordination

number is defined as the average number of contacts per particle, i.e.:

$$Z = 2N_c/N_p \quad (2.10)$$

where N_c is the total number of contacts, N_p is the total number of particles. The coefficient 2 is introduced due to the fact that one contact is shared by two particles. (Thornton and Antony, 1998) proposed a more sophisticated definition of Z by removing rattlers from the packing. The void ratio and the coordination number are closely related, while a direct linkage between these two has not been found. For example, the void ratio can be used to define the critical state line. But there is no evidence that the coordination number is interchangeable with void ratio and defines a similar curve in $Z - p$ plane. More interesting findings on coordination number are reported by physicists (Song et al., 2008; Wang et al., 2010).

Fabric anisotropy

As two significant fabric anisotropic parts in granular materials, the material fabric refers to the contact network composed of all contact branches, while the force fabric is the network through which forces transmit. Indeed, the material fabric is the basis of the force fabric and, reversely, the force fabric can reconstruct the material fabric. The evolution and interaction of these two fabrics are fundamental microscopic ingredients of the granular assembly. (Oda, 1972a,b,c), as a succession of works, first highlighted the importance of the material fabric. By considering the tomography technique on sections of resin-glued sand sample subjected to a drained triaxial loading path, the author measured the material fabric and quantitatively presented directions of individual contacts into a density distribution $E(\theta, \beta)$, where θ and β are two coordinates in the spherical coordinate system, determining the contact direction. $E(\theta, \beta)$ enabled the material fabric to be briefly described and compared at different strain

states. $E(\theta, \beta)$ was observed to increase its anisotropy with the increasing axial strain, the direction of this anisotropy coincides with that of the axial strain. In these researches, the significant effect of the fabric anisotropy on the material's global mechanical responses was illustrated with respect to three aspects: (1) both the mechanical and the volumetric responses of the material were sensitive to the initial fabric anisotropy; (2) the stress anisotropy, i.e. the stress ratio, and stress-dilatancy was quantitatively related to the fabric anisotropy; and (3) the strain localization domain was highly associated with a localized value of the fabric anisotropy.

(Rothenburg and Bathurst, 1989) investigated the evolution of the material fabric and the force fabric in the biaxial test. The material fabric parameter α and force parameters α_n and α_t are traced during loading. A relation between deviatoric stress and these fabric parameters was theoretically derived and then experimentally proven, as given below:

$$\frac{\sigma_1 - \sigma_2}{\sigma_1 + \sigma_2} = \frac{1}{2}(\alpha + \alpha_n + \alpha_t) \quad (2.11)$$

where σ_1 and σ_2 are the axial and the lateral stress eigenvalues, respectively. (Azéma et al., 2007), in a numerical biaxial test on a pentagons assembly, also investigated the evolution of α , α_n and α_t and examined Equation 2.11. Their results supported Equation 2.11.

However, all information on fabric is unable to describe the complete behavior of granular material, because in this information, contacts are considered independently in an orientational distribution (or function), presenting neither organization nor relative displacement among each other. However, the strain in granular assemblies is derived from the relative displacement not only between contacting grains but also among rearrangement of particles. This means that the strain can be only derived on a scale competent to characterize the organization among contacts that is, in other words, a scale larger than single contact scale. On the other side, since the force fabric was evidenced, scientists gradually realized that the

force transmission in the granular material also presents an organization in a scale much larger than the single contact scale, the so-called 'force-chain', which will be mentioned in the following subsection. It is far from possible to correctly formulate the evolution of the force fabric only in an orientational function. Therefore, both material and force fabrics are required to be investigated in a scale larger than the single contact scale but, of course, smaller than the macro-scale, i.e. the so-called meso-scale. In this meso-scale, force-chains and meso-loops (will be introduced later) can be identified, as relevant ways to characterize respectively the force fabric and the material fabric. Furthermore, this meso-scale is also a significant intermediate scale in developing micromechanically-based constitutive model (introduced in [chapter 3](#)).

2.2.2 Force-chain

Force fabric shows significant heterogeneity patterns in granular materials due to the disordered granular packing (Cambou et al., 2013). This phenomenon was first observed in the experimental results of photoelastic materials (Dantu, 1968; Drescher and De Jong, 1972). Similar observations can be found in [Figure 2.1a](#), force fabric does not display homogeneously in granular materials but follows some column paths, establishing a connecting network, showing a more obviously heterogeneous and anisotropic pattern than that of the material fabric. This characteristic of granular materials was not investigated further until the middle of the 1990s. (Jaeger et al., 1996) investigated the force fabric acting on the boundary particle by measuring spots left on the carbon paper by boundary particles. A decreasing exponential density distribution of force magnitude was found.

Based on the average force in the granular materials, (Radjai and Roux, 1995; Radjai et al., 1998) classified the strong force network and weak force network and also investigated the organization of both. The weak network shows a uniform or power-law shape of density

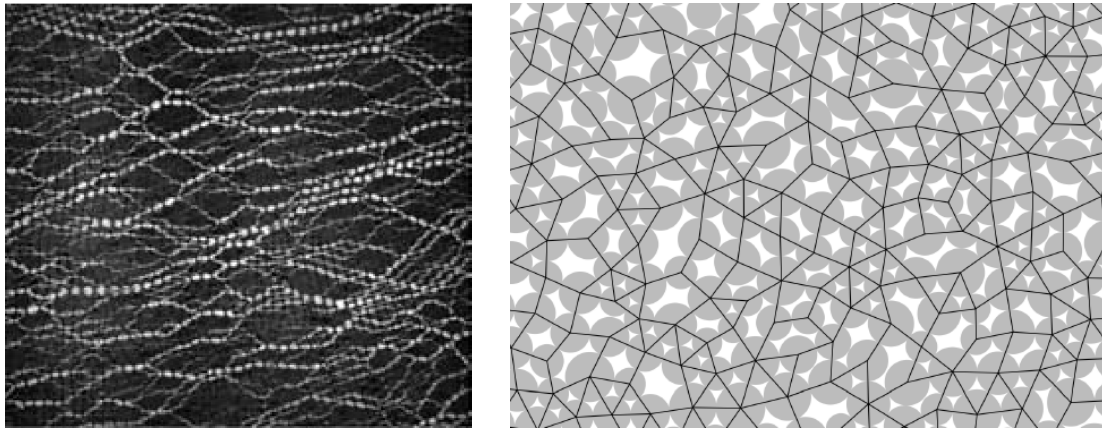
distribution, whereas the strong network, as a complement to the weak network, displays an exponential one (Mueth et al., 1998; Radjai et al., 1996). Further studies evidenced that the exponential density distribution of strong network is sensitive to the grain size distribution and to the initial state, being a leading characteristic of granular materials subjected to external loading (Antony, 2000; Azéma et al., 2007; Blair et al., 2001; Erikson et al., 2002; Mueggenburg et al., 2002; Mueth et al., 1998; Radjai et al., 1999; Silbert et al., 2002). Generally speaking, heterogeneous force distribution persistently exists in the solid phase of granular materials, whereas the fluid and gas phases are different (Jaeger et al., 1996). In recent research, the jamming transition, a concept similar to the phase transition, was observed to be highly associated to the formation of the heterogeneous force distribution (Behringer et al., 2008; Kondic et al., 2012). In this context, the strong network is distinguished from the weak network, then the concept of force-chain was proposed based on the strong network to define those quasi-linear columns, consisting of contacts with a force magnitude greater than the average.

Further investigations have shown the significant role the force-chains plays in the macroscopic behavior of granular materials. (Iwashita and Oda, 2000; Oda and Iwashita, 2000) in numerical biaxial tests with the particle rolling resistance, investigated micro-scale properties of granular assemblies with shear bands. They noticed the formation of shear bands strongly related to the massive generation of force-chains during the hardening process and their collapse in the softening process, accompanied with a volumetric dilatancy. Based on results of numerical biaxial tests, (Tordesillas, 2007) analyzed the evolution of the void ratio around force-chains and the damage pattern of force-chain. Some pieces of evidence about the link between force-chains and stress-dilatancy were found. This intriguing work shed a light to answer the question that how the volumetric variation on the material fabric influences the force fabric evolution. However, a reasonable answer requires a more precise investigation on how force-chains and their surrounding structures interact with each other. A

priori, force-chains' surrounding fabric should be characterized in a clear way with physical meanings. The meso-loop, which will be introduced in the following, provides a promising way in this aspect.

2.2.3 Meso-loops

(Satake, 1992) introduced an approach to associate discrete mechanical properties with the continuum-mechanical ones. In this approach, as shown in [Figure 2.1b](#), the contact network seamlessly tessellates the material area into loops, which are enclosed by contact branches and involves fan-shaped sections of particles and voids surrounded by particles. Therefore, voids can be correctly quantified inside loops by local kinematical properties. This approach gave a way of characterizing the material fabric by considering the microscopic volumetric nature on the loop scale, namely a meso-scale. Then the loop can be also called the meso-loop. (Bagi, 1993; Nguyen et al., 2012) expressed the stress on the meso-scale as a volume average of the tensorial product of the contact forces and the contact branches. This way of defining the meso-scale stress was satisfying only in static or quasi-static state, otherwise, an inertial term should be involved according to the expression given by (Bagi, 1993, 1996; Cambou et al., 2000; Krut, 2003; Krut and Rothenburg, 1996; Nicot et al., 2013). Several approaches were proposed to derive the average strain of the material from relative displacements on contacts and geometrical quantities of loops. Results proved that the global strain can be correctly presented from the local kinematics of the meso-loops. (Nguyen et al., 2009) gave a definition of the strain on the meso-loop. This meso-scale strain facilitates researchers to make the analysis on the meso-scale, by characterizing the meso-scale kinematics into a continuum-mechanical form which researchers are familiar with.



(a) Force fabric in the granular assembly made up of photoelastic material, in a simple shear test. The brightness of light lines presents the force magnitude (Majmudar and Behringer, 2005).

(b) Contact network composed of contact branches in the 2D granular assembly. Black continuous lines are contact branches, gray disks are grains (Zhu, 2015).

Figure 2.1 Force chain and meso-loops

2.3 Instability in granular materials

Instabilities in geomechanics manifest themselves through mainly two failure modes: localized and diffuse. For example, a natural slope may undergo large displacements as a result of strains either localizing into shear bands or developing in a diffuse mode throughout its whole mass. With respect to strain localization, there are different forms of concentrated deformations such as shear bands, compaction bands, and dilation bands (Rudnicki and Rice, 1975; Sulem and Vardoulakis, 2004; Vardoulakis et al., 1978). The significance of these typically narrow zones of intense shearing and inhomogeneous strains has been recognized for decades both at macro-scale (geotechnical problems) and micro-scale (lab experiments) (Desrues and Viggiani, 2004). Only in recent years, this form of failure with self-conducted concentrated deformations into narrow zones has been viewed as a bifurcation problem (Alshibli et al., 2003). The related bifurcation at the material point level is usually triggered around the peak response of a strain softening material or at the plastic limit failure state (Bésuelle and Rudnicki, 2004).

On the other side, it has been recently found that another type of instability can appear well before plastic localized failure is reached (Darve, 1994). This means that other forms of failure may as well occur within the Mohr-Coulomb plastic limit surface. For example, when loose sand is sheared along undrained loading paths, it may collapse as a result of a loss in stress far from the plastic limit surface. In this type of instability, known as diffuse instability, no occurrence of strain localization is visible but a rather broadly failure takes place.

In both localized and diffuse instability cases, the problem underlies a material instability phenomenon which originates in the small scale due to the micro-structure characteristics of the granular material. At such a microscale, mechanisms of energy dissipation and force chain buckling lead to local instabilities that reflect at the macroscopic scale through a dilatancy behavior, strain localization, or liquefaction, among others.

2.3.1 Experimental observations

A variety of experimental studies has been performed in the recent decades to investigate both localized and diffuse failures in geomechanics (Castro, 1969; Chu et al., 2003; Darve et al., 2007; Desrues et al., 1996; Finno et al., 1997; Vardoulakis, 1980; Wang and Lade, 2001). Methods to recognize and observe failure in granular material specimens include conventional procedures such as the installation of extensometers, or more sophisticated techniques such as Computed Tomography and False Relief Stereophotogrammetry (Alshibli et al., 2003; Desrues and Viggiani, 2004; Viggiani et al., 1994). The last two techniques have contributed to interpreting the many interfering and controlling aspects that lead to the strain localization and diffuse failure. These techniques allow the mapping of the external and internal structure of the deformed material.

To evidence localized instability in the experimental setting, one can refer to the plane strain compression drained test illustrated in [Figure 2.2](#). In this test, deformations are only

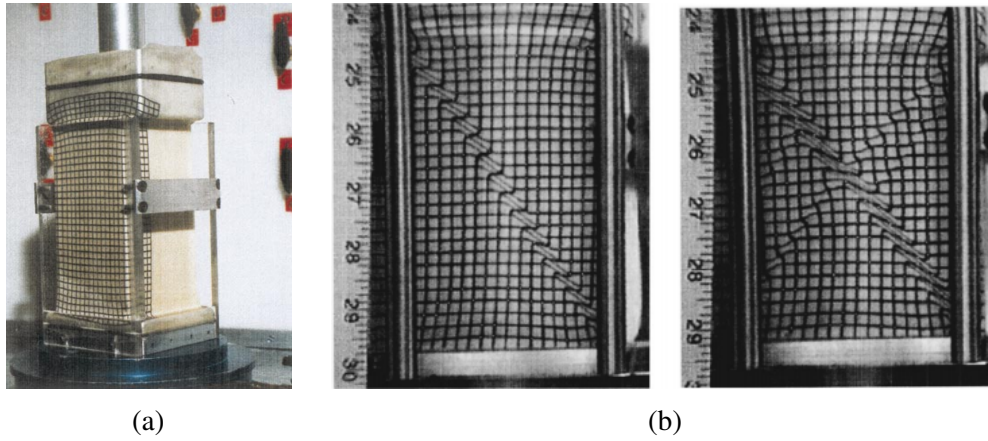


Figure 2.2 Localized strain under plane strain conditions: (a) Soil specimen before compression, (b) Deformed specimen after 9.6% and 19% axial strain (after (Alshibli et al., 2003))

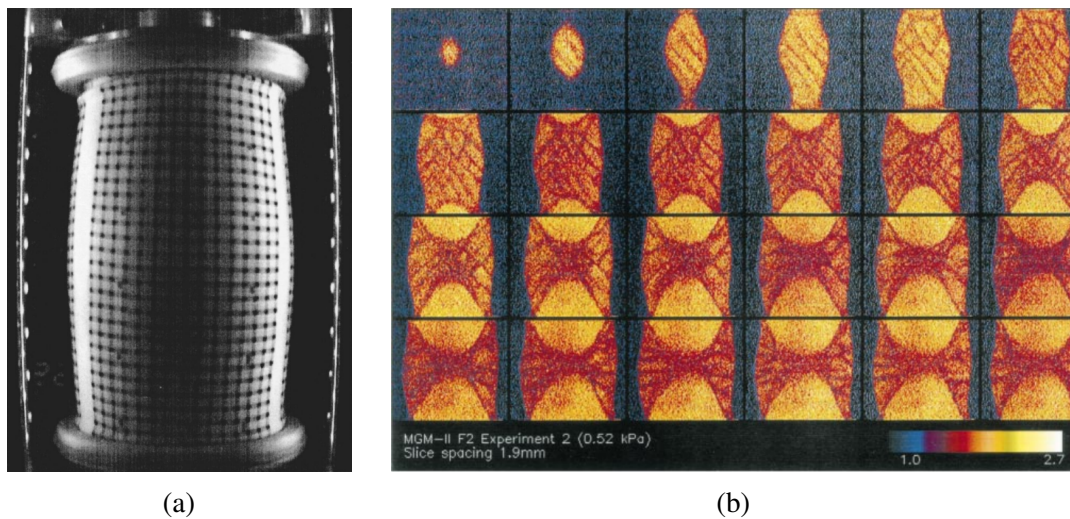


Figure 2.3 Localized strain under triaxial drained compression: (a) Soil specimen at 25% axial strain, (b) CT scans at 25% axial strain (after (Alshibli et al., 2003))

allowed to occur along two direction components, say x (horizontal) and y (vertical). The specimen is first consolidated to an initial isotropic stress state under drained conditions and then is axially loaded along the y -direction through a servo-controlled device while confining stress on x -direction is kept constant. [Figure 2.2](#) shows a sample of medium-dense Ottawa sand tested under plane strain conditions (Alshibli et al., 2003). Planar zones with concentrated deformation developed after 9.6% and 19% axial strain. The formation of such bifurcated instability led the sample to the softening behavior and consequent decrease in strength. Additionally, a conventional triaxial compression test also on F-75 Ottawa sand is shown in [Figure 2.3](#) (Alshibli et al., 2003). Computed tomography and other digital imaging techniques were used to study the development and evolution of shear bands.

Shear banding is a complex phenomenon whose formation and propagation are influenced by a series of factors such as boundary and drainage conditions, stress and density levels, strain history, anisotropy, among others. Experimental observations made by (Alshibli et al., 2003; Desrues and Viggiani, 2004) revealed that confining pressure is the main factor influencing the instability during compression. Localization of deformations developed sooner (i.e. at smaller overall axial strain) for specimens subjected to lower confining pressure compared to those tested at higher confining pressure ([Figure 2.4](#)). Similar findings were reported by (Han and Drescher, 1993), which investigated the effects of the confining pressure on the onset of shear bands by performing a series of experiments on poorly graded Ottawa sand with rounded particles. It found that the shear strain at the initiation of shear band formation increases when the confining pressure increases too.

Some other factors that influence the pattern of shear bands include size, uniformity and angularity of grains, specimen density, size and slenderness, the method of preparation and anisotropy. Many experimental works have been carried out in order to identify and quantify these factors. For example, (Alshibli et al., 2003) investigated the dependence of the overall stress-strain behavior on the specimen's density and sand grain texture on the

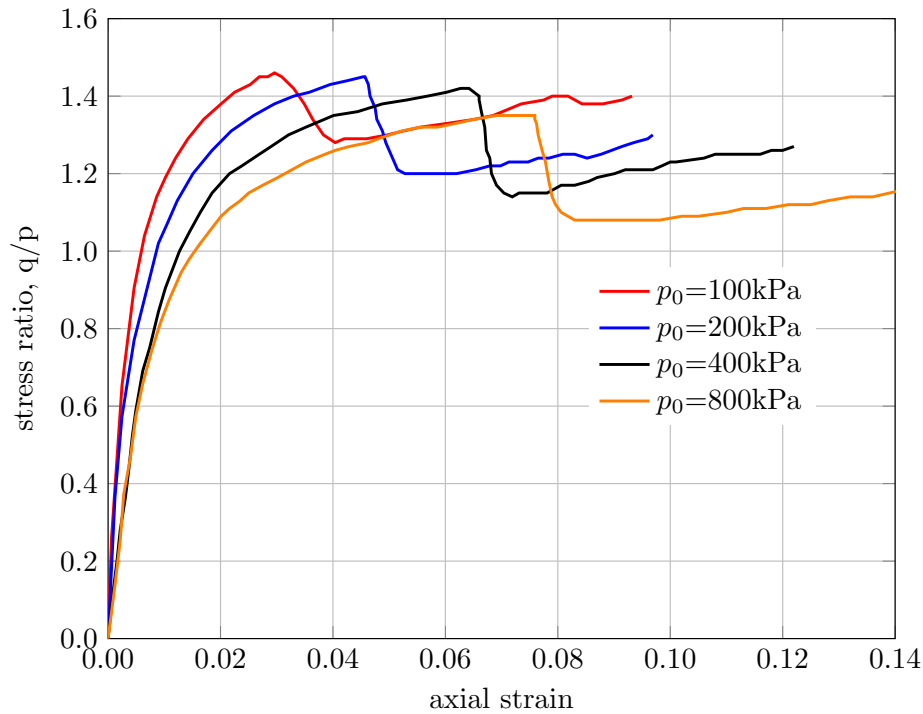


Figure 2.4 Experimental results on dense Hostun sand for biaxial drained tests at different confining pressures (after (Desrues and Viggiani, 2004)).

resulting failure mode. They performed plane strain tests on three different types of sand, namely, F-sand obtained from the Ottawa Industrial Silica Co; M-sand, obtained from Unimin Corp; and C-sand, obtained from the Connecticut Silica Co. F-sand is a rounded, uniform and fine-grained sand; M-sand is an industrial subangular, uniform medium-grained sand; whereas the third sand is an angular, uniform, crushed silica. According to their findings, it appears that higher particle interlocking, which is dependent on grain angularity, requires higher strains to fully mobilize friction along a well-defined shear band, which reduces the possibility of sudden slip mechanisms. The influence of confining pressure on strength and stability decreases as grain angularity decreases. They also reported that packing density has a relatively greater effect on the strength and stability behavior of medium-grained sand compared to fine and coarse sands. For the fine sand, the confining pressure is the main factor affecting the specimen's stability. (Desrues and Viggiani, 2004) observed that, for a given mean stress, shear bands are more precipitous in dense specimens than in loose specimens.

Lastly, the importance of anisotropy of sand deposit was pointed out by (Lade and Wang, 2001). They verified that a specimen created by deposition in the vertical direction, when tested with the major principle stress in the vertical direction, has a tendency to form shear bands more in the horizontal direction than it would have in an isotropic deposit.

Diffuse instability in the lab experimental setting has its origins in two well-known tests, namely, the consolidated undrained triaxial compression test and the constant shear (q -constant) test. In the former, the specimen is first consolidated to an initial isotropic stress state under drained conditions, and then is axially loaded through a servo-controlled device while confining stresses are kept constant (Casagrande, 1975; Castro, 1969; Chu et al., 2003; Lade, 1992; Verdugo and Ishihara, 1996). In the latter, after the initial isotropic consolidation and conventional shear drained phases up to a prescribed stress state, the soil specimen is loaded at constant deviatoric stress while mean effective stress is reduced. This stress path is followed during water infiltration in slopes where external loads remain unchanged but pore pressure increases slowly (due to the fact that the volume is more or less constant, especially in fine soils) to eventually cause failure (Anderson and Riemer, 1995; Brand, 1981; Iverson, 1997; Sasitharan et al., 1993).

The set of experimental data presented by (Chu et al., 2003; Leong, 2002) is re-examined for illustration purposes. This data set comprises a thorough lab experimental study on dredged marine sand from Singapore. The authors carried out undrained tests and q -constant tests on loose and dense soil states. [Figure 2.5](#) shows various results from undrained triaxial compression tests for different initial void ratios. These results reveal the unstable response of the specimens after reaching maximum values for the deviatoric stress. The (so-called) instability lines drawn in the figure join the origin to these peak values as defined in accord with (Lade, 1993). These lines are not unique. Here, their dependence on the initial void ratio is evident.

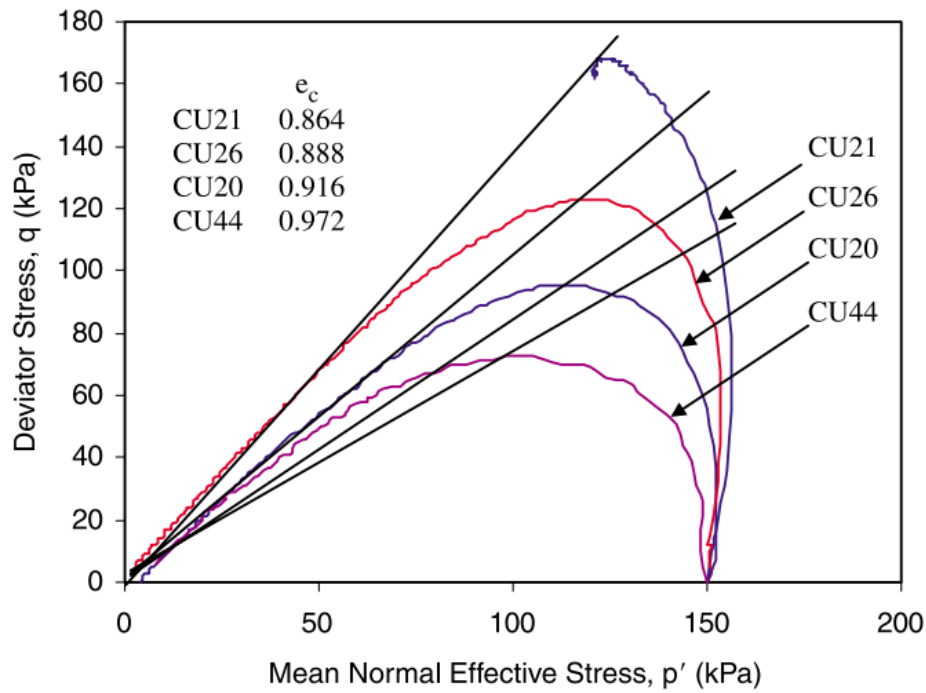


Figure 2.5 Experimental results from several undrained triaxial compression tests for different initial void ratios (after (Chu et al., 2003)).

2.3.2 Theoretical advances

From a theoretical viewpoint, by considering the energy conservation law in continuum mechanics, (Mandel, 1966) expressed with a Lagrangian formalism and a two-order time differentiation (Nicot and Darve, 2007; Nicot et al., 2007a), it is possible to obtain the kinetic energy as a function of the external and internal second-order works (Nicot et al., 2017).

The second-order work criterion was initially introduced by (Hill, 1958) as an instability criterion, with the meaning that the material will continue to deform at least in one stress–strain direction without any external input of energy (see also for example (Bigoni, 2000; Petryk, 1993) for a review of this issue). This means that a certain failure mode can be triggered. Later on, it appears (Bigoni and Hueckel, 1991; Nicot and Darve, 2011a; Valanis, 1989) that the second-order work criterion (vanishing value of the determinant of the symmetric part of the elasto-plastic matrix) contains the particular cases of the strain

localization criterion (vanishing value of the determinant of the acoustic matrix) and the plastic limit criterion (vanishing value of the determinant of the elasto-plastic matrix). It was observed (Li and Richmond, 1997; Li and Karr, 2009) that in initially homogenous materials obeying a nonassociated flow rule (the elasto-plastic matrix is non-symmetric). Thus, if flutter instabilities are not considered, the second-order work criterion is the first to be encountered (according to a monotonously increasing loading parameter) (Challamel et al., 2009, 2010) and the other criteria are simply particular cases within the bifurcation domain. The vanishing values of the determinant of the symmetric part of the elasto-plastic matrix corresponds to the internal boundary of the bifurcation domain (Darve et al., 2004; Neilsen and Schreyer, 1993; Sibille et al., 2007), while its external boundary is the plastic limit condition. Thus the second-order work criterion can be considered a necessary condition for failure (flutter instabilities excluded) according to these theoretical results. This conclusion was also verified in experiments (Darve et al., 2007) and very carefully checked by direct numerical simulations of failure with a discrete element method (Sibille et al., 2008).

It is essential to note that the second-order criterion by itself does not provide a sufficient condition for failure. But when second-order work vanishes along a loading path, the material may become unstable with a bifurcation from a quasi-static regime towards a dynamic regime. By definition, the second-order work vanishes at the plastic threshold, but it may also vanish below the plastic threshold in granular materials as a result of the asymmetry of the constitutive tensor, reflecting the fact that the direction of shear strain is independent of the yield surface (given by the internal angle of friction). As a consequence, the potential energy stored in the granular configuration by dilation may in principle transform spontaneously to shear deformation so that the material may keep deforming without further energy input. In contrast to localized structures appearing prior to failure in the form of shear zones or compaction bands at the plastic threshold, the failure appearing in the bifurcation domain below the plastic threshold is homogeneous or diffuse, in close analogy with liquefaction

where the instability fully spreads to the bulk as a consequence of load transfer from the contact network to the pore liquid (Lade, 1992).

Moreover, it is worth noting that, in grain avalanches, strong correlations have been observed repeatedly in discrete element simulations (Darve et al., 2004) between second-order work and kinetic energy. From a spatial point of view, the area where the second-order work computed on the particle scale takes negative values coincides with the area of bursts of particle kinetic energy. The second-order work computed on the particle (or the contact between particles) scale is also referred to as the discrete second-order work, to emphasize that it is computed from local variables, contrary to the macroscopic second-order work computed in the continuum. From a temporal point of view, by considering the changes over time of the total kinetic energy and the total second-order work for all the particles, the peaks of kinetic energy correlate very well with the negative minima of the second-order work.

So far, most investigations have dealt with the material point scale, or with homogeneous specimens subjected to homogeneous loading paths. Extending the second-order work formalism to more general boundary value problems remains an open, and important, issue. At the same time, this challenge is of paramount importance in view of making this approach efficient for engineering purposes. (Nicot et al., 2017) demonstrates how the second-order work approach can be conveniently extended to boundary value problems, where the internal and external second-order works are computed based on the mechanical parameters (forces, displacements) acting on the boundary of the system only, without requiring any information inside the system. This is a great advantage since these boundary parameters are generally accessible.

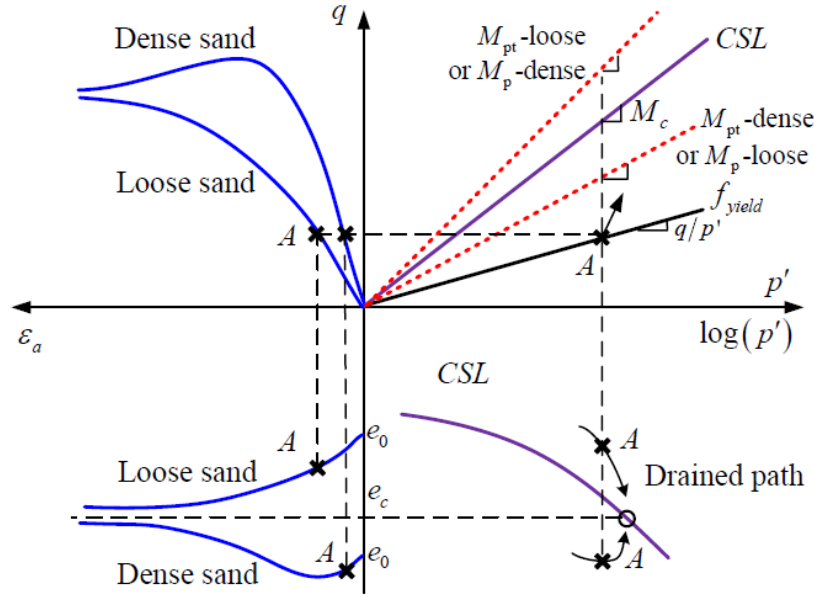


Figure 2.6 Principle of simple critical-state based model of sand (after (Wu et al., 2017)).

2.4 Constitutive modeling of granular materials

In soil mechanics, many phenomenological models were developed to describe complex phenomena. These models constantly involve enriched and complex mathematical equations introducing a great number of parameters to describe different observed phenomena. Some typical phenomenological models are reviewed here such as elastoplastic theories (Drucker and Prager, 2013; Hill, 1967; Rice, 1970, 1975; Yao et al., 2008), endochronic models (Bažant, 1978), hypoplastic theories (Kolymbas, 1991), and incrementally nonlinear models (Darve, 1990; Darve et al., 1995). For example, (Yin et al., 2013) developed a simple critical state based model (the so-called SIMSAND model) which can well capture the macroscopic behavior of different kinds of real sands. The yield surface with the principle of this model is plotted in $p' - q$ and $e - p'$ plane, shown in Figure 2.6.

With the deepening of the microscopic mechanism of granular materials, researchers started building the constitutive relation by considering micro-mechanisms. One kind of approach builds the constitutive relation still in a phenomenological framework, such as

in the framework of elasto-plasticity, but introducing the fabric-related parameters into the constitutive formulations. (Li and Dafalias, 2011) extended the critical state theory (Shigeto and Sakai, 2011) by achieving the critical state through a constant fabric instead of the constant stress or volumetric strain. Under this framework, the critical state fabric anisotropy was investigated by (Guo and Zhao, 2013b; Zhao and Guo, 2013), giving the critical state relation between the fabric anisotropy parameters and the hydrostatic pressure. Then, several constitutive relations (Gao and Zhao, 2012; Gao et al., 2014) were built based on this framework by involving fabric anisotropy parameters. This kind of approach only adjusted the phenomenological framework by considering some parameters with micro-physical meaning. However, the macroscopic relations did not stem from their microscopic essences but still from empirical relations.

On the contrary, an increasing sight can be found in microscopic modeling and multi-scale approaches on both numerical and experimental sides, with the development of microscopy technology and X-ray tomography (Fonseca et al., 2014). It is an alternative way to consider that the variety of constitutive properties stem essentially from the granular character (Cambou et al., 1995; Chang et al., 2009; Krut and Rothenburg, 2002). The multi-scale approach sophisticatedly links the macroscopic quantities with the static and kinematic aspect of the fabric by crossing the scales. (Chang and Misra, 1989; Chang et al., 1992), in their pioneering work, respectively related the incremental stress and strain to the contact force and the contact based on the contact fabric distribution $E(\theta, \beta)$ (see [subsection 2.2.1](#)). After that, various constitutive models (Chang et al., 1990; Yin et al., 2011a,b) were proposed for different kinds of soil, following similar methods as that proposed by (Chang and Misra, 1989; Chang et al., 1992). The difference only lied in the form of the initial density distribution for the contact fabric. (Emeriault and Cambou, 1996) clarified the general framework of deriving the constitutive relation for granular materials, involving three parts: the strain localization (or averaging) scheme, to determine the local kinematical variables from the global strain (or

reverse); the local constitutive relation, to link the local static quantities to the local kinematic quantities (or reverse); and the stress averaging (or localization) scheme, to solve the global stress from local quantities (or reverse). In this work, representation theorem (Spencer, 1987) was applied to formulate the relation between the local kinematics and the global strain. Combining with the stress homogenization scheme, a micro-mechanical model was derived from a non-linear elastic model, the Hertz-Mindlin model (Mindlin, 1953).

So far, the aforementioned constitutive models were usually developed based on the homogeneous condition (or a representative elementary volume), requiring to be implemented in view to solve geotechnical engineering problems. From a historical point of view, geotechnical engineering problems were empirically solved until a series of theoretical advances was proposed by pioneers in soil mechanics in the early 20th century. They are well known today as bearing capacity theory, consolidation theories, limit theorem (Drucker et al., 1952; Prager, 1952; Taylor, 1948; Terzaghi, 1943). However, these oversimplified theories are sometimes not suitable for most geotechnical issues due to the complexity of the problems including nonlinearities and coupled mechanisms. Since 1960s, computers and numerical tools were made accessible to geotechnical engineers. Several classes of numerical methods have been developed to handle geotechnical engineering problems including:

- (i) discrete approaches that explicitly describe inter-particle contact behavior among the granular assembly such as the discrete element method (DEM) (Cundall and Strack, 1979),
- (ii) continuum approaches that characterize path-dependent responses with internal variables and constitutive laws on the macroscopic scale such as the finite element method (FEM) (Courant, 1943; Hrennikoff, 1941), and
- (iii) multiscale approaches that build a constitutive relation on the specimen (material point) scale by taking microstructure information into account.

The continuum approach has been widely used to solve geotechnical engineering problems by employing phenomenological elastoplastic models which can successfully simulate the macroscopic behavior of granular assembly. Unfortunately, they do not give access to the microscopic scale in order to investigate or interpret micro-mechanisms. On the other side, the discrete approach indeed provides a simple way to do it but it is also computationally intensive to resolve the aforementioned deficiencies of continuum approaches for simulating geotechnical engineering problems.

To overcome this issue, various multiscale approaches have been proposed to couple grain-scale simulations with macroscopic continuum-scale finite element analysis. For instance, (Wellmann and Wriggers, 2012) introduced an Arlequin DEM-FEM model that divides the spatial domain into discrete and continuum sub-domains. The interaction between discrete and continuum sub-domains is assumed by overlapping with each other so that artificial reflections can be provided. (Li and Wan, 2011) proposed bridging scale method, which uses a handshake domain to couple particulate model with a higher-order continuum description. (Andrade et al., 2011; Guo and Zhao, 2014; Miehe et al., 2010; Nguyen et al., 2014; Nitka et al., 2011; Stránský and Jirásek, 2012) proposed a conceptually similar approach where the DEM solver is used at Gauss points of the finite element mesh as a representative elementary volume (REV). Nevertheless, these DEM-FEM methods have a limitation when geotechnical engineering problems are considered due to the fact that a great number of particles need to be contained in a boundary value problem (BVP) in order to reach local convergence. It makes these methods waste computational resources resulting in inefficient simulations.

From microscale to BVPs (boundary value problems), the multi-scale approach can effectively link a continuum-based method to a discontinuum-based method. Generally, the FEM (finite element method) is considered to solve the BVP on the macro-scale, while the DEM (discrete element method) (Cundall and Strack, 1979; Radjaï and Dubois, 2011) is usually considered effective to capture and describe the behavior on the micro-structural scale.

Both are leading trends of numerical simulation and sometimes can be beneficially coupled. For example, an FEM×DEM scheme is implemented to simulate the slope stability and strain localization problems (Meier et al., 2008, 2009). However, a continuum-based assumption (Taylor assumption (Voigt, 1889)) is employed on the micro-scale, which may lead some limitations for a granular medium. (Andrade and Tu, 2009; Andrade et al., 2011) proposed a discrete-continuum method based on a numerical homogenization scheme to simulate the strain localization problem in granular materials. This approach utilizes a classical plastic model on the macro-scale involving two phenomenological parameters (friction angle and dilation angle), which are transferred from the micro-scale. (Chang and Yin, 2009; Chang et al., 2010; Yin et al., 2009, 2010a, 2011a, 2014) proposed micromechanically-based models adopting static hypothesis and were successfully used to simulate various behaviors of granular soils from sand to clay. More recently, (Guo and Zhao, 2013a) proposed a multi-scale modeling framework for granular media based on a hierarchical cross-scale. This framework is also implemented to simulate a variety of engineering problems including hydro-mechanical problems (Guo and Zhao, 2014, 2016a,b).

2.5 Concluding remarks

Based on the comprehensive literature review presented above, the following concluding remarks are highlighted:

- A constitutive model for granular materials has to account for their complex mechanical behavior that originates from non-linearity together with density, stress level and strain history dependencies in relation with development of anisotropy. As the richness of the material description increases, the analysis makes it possible that non-uniqueness, bifurcation and material instability naturally emerge as subtle distinctive features of failure.

- Both the force and material fabrics only exist on the meso-scale and on larger scales, any smaller scale will blind to capture them. In order to build the proper constitutive model with the multiscale approach, the meso-scale should be a significant part, linking the microscopic variables and the macroscopic quantities.
- Conventional methods of analysis lack the ingredients that allow them to capture the fundamental mechanics of granular materials. More advanced techniques, such as the multiscale approach, need to be employed. In this perspective, it is essential to equip the Finite Element Method with a robust constitutive model that captures the proper behavior of granular materials.

Chapter 3

An extended micromechanically-based model for granular materials

A fundamental task of the mechanics is to translate knowledge and observations into the mathematical relations, those are capable of predicting or simulating the reality. Granular materials usually react with complicated mechanical responses when subjected to external loading paths. This leads to sophisticated constitutive formulations requiring large numbers of parameters. A powerful and straightforward way consists in developing micro-mechanical models embedding both micro-scale and meso-scale. This chapter proposes a three-dimensional micro-mechanical model taking into account an intermediate scale (meso-scale) which makes it possible to describe a variety of constitutive features in a natural way. The comparison between experimental tests and numerical simulations reveals the predictive capability of this model. Particularly, several simulations are carried out with different confining pressures and initial void ratios, based on the fact that the critical state is quantitatively described without requiring any critical state formulations and parameter. The model mechanism is also analyzed from a microscopic view, wherein the evolution of some key microscopic parameters is investigated.

3.1 Reviews of the micro-directional models

Complex constitutive characteristics have been observed and investigated for granular materials, such as a highly incrementally non-linear constitutive behavior (Darve, 1990; Darve et al., 1995), the existence of the non-associate flow rule, the existence of a bifurcation domain within the plastic limit (Darve et al., 2004; Nicot et al., 2009). Taking the advantage of these constitutive characteristics, large numbers of phenomenological models have been proposed in recent decades. In this kind of models, attempts are made to transform different observed phenomena into mathematical expressions, for example: elasto-plastic theories (Drucker and Prager, 2013; Hill, 1967; Rice, 1970, 1975), endochronic models (Bažant, 1978), hypo-plastic theories (Kolymbas, 1991), and non-linear incremental models (Darve, 1990; Darve et al., 1995). Phenomenological models normally involve sophisticated constitutive formulations requiring large numbers of parameters, moreover, most of these parameters lack physical backgrounds.

Building a constitutive relation in a natural way is a challenge, namely, taking into account the constitutive features at smaller scales, from which the macro-scale behavior of materials stem. In order to link the macro-scale to a smaller scale, it is inevitable to seek a suitable scale, to which macroscopic behaviors can be comprehensively associated. The subsequent revisited micro-directional models consist of the micro-directional model (Nicot et al., 2005) and the H-microdirectional model (or H-model) (Nicot and Darve, 2011b). The former builds the force-displacement relation on the grain scale (micro-scale) while the latter takes into account constitutive relations on the granular cluster scale (meso-scale). They were initially developed to describe the mechanical behavior of snow (Nicot, 2003). The micro-directional model was then generalized to any type of granular assembly, with a particular emphasis on frictional granular materials (Nicot et al., 2005).

3.1.1 The micro-directional model

Building the constitutive relations of granular materials with a multi-scale approach requires the stress and strain tensors to be related on the micro scale. Basically, a granular assembly with applied loads to boundary grains will evolve with the change of boundary conditions. The evolution of grains follows Newton's law, with repulsive forces between grains that are not nil when contact exists. The boundary grains firstly move according to the mechanical imbalance. Thus, these displacements progressively disturb the internal balance according to Newton's second law and the granular assembly rearranges. As a consequence, the mechanical response of a granular assembly results from dynamical mechanisms governing the motion of each particle constrained by the existence of adjoining particles. This is exactly the leading principle of discrete element models (Cundall and Hart, 1992). However, high degree of freedom in the resulting nonlinear differential equation system implies that it is merely impossible to obtain the analytical solution of the problem.

To simplify the differential equation system, some assumptions are introduced. In the micro-directional model, all grains of the granular assembly are considered to be spherical. The specimen is described as a distribution of contacts oriented along each direction of the physical space. All contact directions are independent of each other. Thus, the constitutive relation of the micro-directional model can be decomposed in three steps as shown in the general homogenization scheme ([Figure 3.1](#)),

(1) Kinematic localization:

$$\begin{aligned}\delta u_n &= 2r_g \delta \varepsilon_{ij} n_i n_j \\ \delta u_t &= 2r_g \delta \varepsilon_{ij} n_i t_j\end{aligned}\tag{3.1}$$

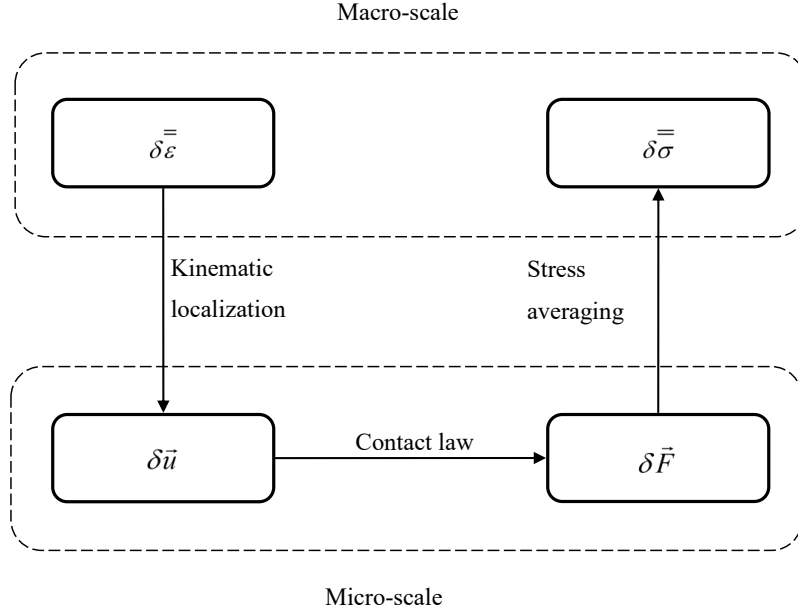


Figure 3.1 General homogenization scheme of the micro-directional model (Cambou et al., 1995).

where δu_n and δu_t respectively denote the incremental relative displacement along the normal direction \vec{n} and along the tangential direction \vec{t} to the idealized contact plane, r_g denotes the mean radius of the spherical grains, $\delta \epsilon_{ij}$ is the incremental macrostrain tensor.

(2) Contact law: The local behavior is selected according to the granular material in hand. For granular soils, an elasto-perfect plastic model can be implemented, relating the local normal force F_n to the local normal relative displacement u_n as well as the local tangential force F_t to the local tangential relative displacement u_t . Besides, this contact law includes a Mohr-Coulomb criterion and can be expressed under the following incremental formalism, which introduces a normal elastic stiffness k_n and a tangential elastic stiffness k_t , both constant, and a local friction angle φ_g .

$$\begin{cases} \delta F_n = k_n \delta u_n \\ \delta \vec{F}_t = \min \left\{ \left\| \vec{F}_t + k_t \delta \vec{u}_t \right\|, \tan \varphi_g (F_n + \delta F_n) \right\} \times \frac{\vec{F}_t + k_t \delta \vec{u}_t}{\left\| \vec{F}_t + k_t \delta \vec{u}_t \right\|} - \vec{F}_t \end{cases} \quad (3.2)$$

(3) Stress averaging: The stress tensor for a representative elementary volume (REV) packing is homogenized based on the Love's formula (Christoffersen et al., 1981; Love, 1927; Mehrabadi et al., 1982)

$$\sigma_{ij} = \frac{1}{V} \sum_{c=1}^{N_c} F_i l_j \quad (3.3)$$

where \vec{l} is the branch vector joining the centers of particles in contact on contact c , \vec{F} is the contact force, and the sum is extended to all the N_c contacts occurring in the REV of volume V .

In multi-scale approach, when the status of contacts arranging along different directions is quantified by $w(n)$, the frequency of contacts along direction \vec{n} , Equation 3.3 can be transformed into:

$$\sigma_{ij} = 2r_g \iint_D \hat{F}_i n_j \omega(\vec{n}) d\Omega \quad (3.4)$$

where $d\Omega$ is the infinitesimal solid angle, which varies in the integration surface D . \hat{F}_i is the i th coordinate of average force of all contacts along the direction represented by the unit vector n_j . Differentiation of Equation 3.4 gives,

$$\delta \sigma_{ij} = 2r_g \left(1 + \iint_D \delta \hat{F}_i n_j \omega(\vec{n}) d\Omega + \iint_D \hat{F}_i n_j \delta \omega(\vec{n}) d\Omega \right) \quad (3.5)$$

The material fabric in the assembly may evolve state by state. This evolution is described by the change of the distribution $\omega(\vec{n})$, indicating that the contact density varies along each direction. When acting as a key function in the expression of the stress, $\omega(\vec{n})$ is significant in this model because it not only presents the arrangement of the material texture, but also prominently controls the mechanical response of the material. In fact, several empirical relations can be used to predict the value of $\omega(\vec{n})$ by referring to different mechanical properties of the material (Chang, 1987; Chang et al., 1990; Yin et al., 2010b, 2011b). In

this model, the relation reported by (Calvetti et al., 1997; Oda, 1972a; Oda et al., 1980) is included inside, in order to calculate the number of contacts along a given direction at each step, from the incremental strain. This relation assumes the contact number increasing in the contractant directions and decreasing in the dilatant ones, as follows:

$$\frac{\delta \omega(\vec{n})}{\omega(\vec{n})} = \alpha (\delta \bar{\epsilon} : \vec{n}) \cdot \vec{n} \quad (3.6)$$

where α is an adjustable coefficient for different materials. The meaning of this function is that during a quasi-static loading, the fabric follows the variation of the strain, and the stress response subsequently adjusts according to the fabric. Consequently, in the implementation of this model, when an incremental strain is given, both fabric and stress evolution can be also determined.

3.1.2 From the micro-directional model to the H-model

The micro-directional model was shown to be powerful and convenient, allowing realistic simulation of most of the standard loading paths. This is due to the two fundamental assumptions ordered in terms of strain kinematic localization: (1) there is an affine relation between global strain and local deformation inside material, making the global strain to be projected into each direction of the space in order to obtain local deformation; (2) contacts in different directions evolve independently from each other. However, "Every coin has two sides", these two assumptions are foundations of the micro-directional model, bringing advantages as well as limitations.

The first assumption can be alternatively rewritten as that: the inter-particle contact fabric only depends on the global strain, however, this is mostly contradictory to the reality. As referred in (Zhu, 2015), the global strain stems not only from the deformation between contacting particles, but also from the fabric rearrangement inside the material. From a meso-

scale point of view, three parts contribute to the global volumetric strain in 2D conditions: the relative displacement on the contact, the conversion between different categories of meso-loops and the area variation of meso-loops caused by the shape changing. Moreover, the latter two parts cannot recover during the unloading, deriving the plastic volumetric strain.

However, the fabric rearrangement does not contribute to the global strain in the micro-directional model, leading to two consequences: due to the ignorance on the part of strain deriving from the fabric arrangement, there is an underestimation toward the volumetric contractancy or, inversely, an overestimation toward the dilatancy; the incremental strain is totally assigned to the local displacement, causing an overestimation of the local contact deformation and, consequently, an excessive stress. There is therefore an exceedingly higher stiffness than in reality.

3.1.3 The H-microdirectional model (H-model)

As an extension of the micro-directional model, the H-microdirectional model was developed to describe the constitutive relation of granular materials by taking into account the local geometrical interaction between grains (Nicot and Darve, 2011b). The main limitation of the micro-directional model is that the deformation on the contact level corresponds to the strain on the macroscopic (specimen) scale. (the so-called affine approximation)

To overcome this limitation, a hexagon pattern (meso-scale) takes the place of the single contact to be the directional element constituting the material fabric on the meso-scale. The hexagon, as shown in [Figure 3.2](#), consists of six particles with identical radius. A fundamental assumption of the hexagon pattern should be declared, that the hexagon is fully symmetric with respect to axis \vec{n} and \vec{t} . The quasi-static equilibrium of the hexagon can be reached under

the symmetric external forces. Thus, only the mechanical balance of two grains, denoted by grain 1 and 2, is needed to be solved.

The local geometrical configuration of the hexagon pattern is illustrated in [Figure 3.3](#), in which numbers label the particle centers. The length along \vec{n} and the width extending laterally, along \vec{t} , are respectively denoted by l_1 and l_2 . Due to an axi-symmetrical configuration, the local kinematics of one hexagon is described by only three independent variables: two branch lengths, d_1 and d_2 , which are initially equal to $2r_g$, and an opening angle α between branch \vec{l}_{21} and \vec{n} . The opening angle α embedded in the hexagon pattern is a significant parameter, highly relating the deformation and the void ratio of the hexagon, and therefore, used to calibrate the volumetric strain of the specimen. In the H-model, the void ratio of a hexagon is expressed as:

$$e(\vec{n}) = \frac{4\sin\alpha(1 + \cos\alpha)}{\pi} - 1 \quad (3.7)$$

Different with the micro-directional model, particle rearrangement can be reflected by updating the opening angle in each hexagon, which evolves during the loading path.

In terms of local static variables, as shown in [Figure 3.3](#), the symmetry and the equilibrium of this system are ensured by external forces F_1 and F_2 , exerted respectively symmetrically in the directions of \vec{n} and \vec{t} . Three independent variables in terms of the contact force, which form the entire local static information, can be identified: N_1 and T_1 , the normal and tangential force between particle 1 and 2, and N_2 , the normal force between particle 2 and 3. To maintain the axi-symmetry around the axis \vec{t} , the tangential displacement and force between particle 2 and 3 are eliminated. These internal static variables are related to three local kinematic variables in an incremental form by the elasto-frictional law:

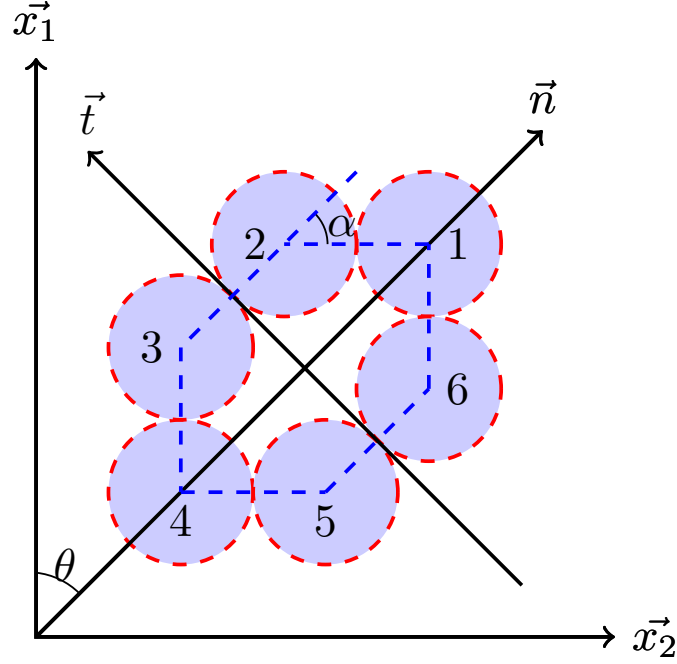


Figure 3.2 The hexagonal element of the H-directional model.

$$\begin{aligned}
 \delta N_1 &= -k_n \delta d_1 \\
 \delta N_2 &= -k_n \delta d_2 \\
 \delta T_1 &= \min \{ |T_1 + k_t d_1 \delta \alpha|, \tan \phi_g (N_1 - k_n \delta d_1) \} \xi - T_1
 \end{aligned} \tag{3.8}$$

where ξ is the sign of $T_1 + k_t d_1 \delta \alpha$, k_n and k_t are normal and tangential contact stiffness, respectively.

A series of hexagons, instead of single contacts in the microdirectional model, distribute along different orientations, also following a directional distribution $\omega(\theta)$ in a polar system, where θ is the rotation angle of \vec{n} , i.e. $\vec{n} = \cos \theta \vec{x}_1 + \sin \theta \vec{x}_2$. An affinity on the deformation is also assumed. The incremental of hexagonal lengths, expressed by δl_1 and δl_2 , is related to the global incremental strain $\delta \epsilon_{ij}$:

$$\begin{aligned}
 \delta l_1 &= -l_1 \delta \epsilon_{ij} n_i n_j = -l_1 (\delta \epsilon_1 n_1^2 + \delta \epsilon_2 n_2^2) \\
 \delta l_2 &= -l_2 \delta \epsilon_{ij} t_i t_j = -l_2 (\delta \epsilon_1 t_1^2 + \delta \epsilon_2 t_2^2)
 \end{aligned} \tag{3.9}$$

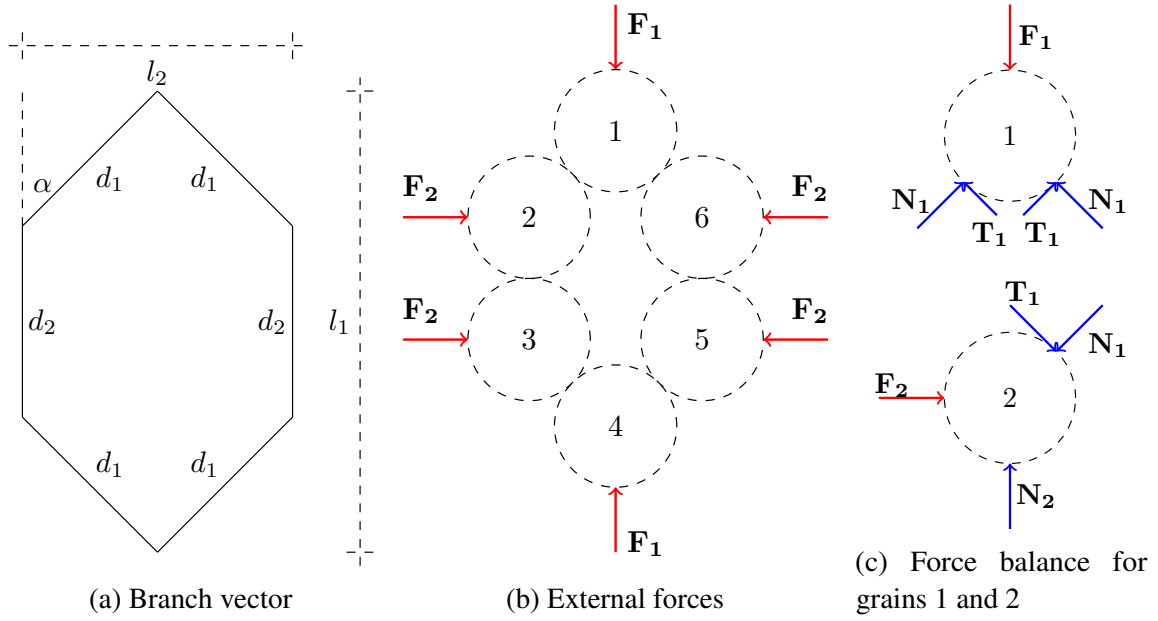


Figure 3.3 Mechanical description of hexagon pattern.

where, restrained by the symmetrical configuration, the material is assumed not to rotate,

namely $\bar{\bar{\delta}}\varepsilon = \begin{bmatrix} \delta\varepsilon_1 & 0 \\ 0 & \delta\varepsilon_2 \end{bmatrix}$

The local constitutive relation formulates the behavior of an individual hexagon, determining incremental internal forces, when the incremental lengths, δl_1 and δl_2 , are given. The local geometrical compatibility reads:

$$\begin{aligned} l_1 &= d_2 + 2d_1 \cos \alpha \\ l_2 &= 2d_1 \sin \alpha \end{aligned} \quad (3.10)$$

Equations 3.10 transformed in incremental form give:

$$\begin{aligned} \delta l_1 &= \delta d_2 + 2\delta d_1 \cos \alpha - 2d_1 \sin \alpha \delta \alpha \\ \delta l_2 &= 2\delta d_1 \sin \alpha + 2d_1 \cos \alpha \delta \alpha \end{aligned} \quad (3.11)$$

The balance condition on particle 2 along direction \vec{n} yields:

$$N_2 = N_1 \cos \alpha + T_1 \sin \alpha \quad (3.12)$$

and under an incremental form,

$$\delta N_2 = \delta N_1 \cos \alpha - N_1 \sin \alpha \delta \alpha + \delta T_1 \sin \alpha + T_1 \cos \alpha \delta \alpha \quad (3.13)$$

Substituting [Equations 3.8](#) into [Equation 3.13](#) gives the balance equation expressed by kinematic variables in an incremental form. Combining with incremental compatibility [Equations 3.11](#) yields a linear system relating δd_1 and δd_2 to incremental internal kinematic variables, d_1 , d_2 and α ,

$$\begin{bmatrix} 2 \cos \alpha & 1 & -2d_1 \sin \alpha \\ 2 \sin \alpha & 0 & 2d_1 \cos \alpha \\ \cos \alpha + A & -1 & \frac{(N_1 - B) \sin \alpha - T_1 \cos \alpha}{k_n} \end{bmatrix} \begin{bmatrix} \delta d_1 \\ \delta d_2 \\ \delta \alpha_1 \end{bmatrix} = \begin{bmatrix} \delta l_1 \\ \delta l_2 \\ C \end{bmatrix} \quad (3.14)$$

In the elastic regime, $A = 0$, $B = k_t d_1$, and $C = 0$, whereas in the plastic regime, $A = \xi \tan \phi_g \sin \alpha$, $B = 0$ and $C = \sin \alpha \left(\frac{\xi \tan \phi_g N_1 - T_1}{k_n} \right)$.

As the local kinematic and static variables are solved, the stress averaging process will be used to obtain the global stress. According to the Love formula ([Equation 3.3](#)), a loop stress $\bar{\bar{\sigma}}(\theta)$ referring to local coordinate system (\vec{n}, \vec{t}) can be given for each hexagon of volume $v(\theta)$, as follows:

$$\bar{\bar{\sigma}}(\theta) = \begin{bmatrix} v(\theta) \bar{\sigma}_n(\theta) & 0 \\ 0 & v(\theta) \bar{\sigma}_t(\theta) \end{bmatrix} \quad (3.15)$$

$$v(\theta) \bar{\sigma}_n(\theta) = 4N_1 d_1 \cos^2 \alpha + 4T_1 \sin \alpha \cos \alpha + 2N_2 d_2$$

$$v(\theta) \bar{\sigma}_t(\theta) = 4N_1 d_1 \sin^2 \alpha - 4T_1 \sin \alpha \cos \alpha$$

An integration of the loop stress along all the orientations renders the global stress,

$$\bar{\bar{\sigma}} = \frac{1}{V} \int \omega(\theta) \bar{P}^{-1} \bar{\bar{\sigma}}(\theta) \bar{P} d\theta \quad (3.16)$$

where \bar{P} is the transport matrix, being equal to $\begin{bmatrix} \cos \theta & \sin \theta \\ \sin \theta & \cos \theta \end{bmatrix}$, V is the volume of the specimen.

Under this framework, one assumption propounded in micro-directional model and their inducing consequences is invalidated; contacts in the fabric will displace never independently, but compatibly with other contacts in individual hexagons. This, however, does not indicate a comprehensive compatibility among all contacts in the specimen, as it is only satisfied on the scale of an individual hexagon.

3.2 A 3D extension of the H-model

The H-directional model is still limited within a 2D context. In order to extend the application range of the H-directional model, especially to implement it in 3D FEM (Finite Element Method) codes, several questions are encountered, such as, how to extend this striking 2D-H model to 3D conditions. More generally, how to extend a 2D multi-scale constitutive model to 3D conditions in a feasible and straightforward way? In this section, an innovative approach which is able to extend the 2D-H model to 3D conditions is presented.

3.2.1 Kinematic localization

In 3D conditions, a global coordinate system $(\vec{x}_1, \vec{x}_2, \vec{x}_3)$ is required, where $\vec{x}_1, \vec{x}_2, \vec{x}_3$ axes stand for the principal stress directions on the macro-scale. The 3D-H model similarly follows the three steps shown in [Figure 3.1](#), going from the incremental macroscopic strain

tensor $\delta \bar{\bar{\epsilon}}$ to the incremental macroscopic stress tensor $\delta \bar{\bar{\sigma}}$ by transforming the micro-scale and meso-scale information. No rotation of the principal axis of both stress and strain tensors is supposed to take place, so that $\delta \bar{\bar{\epsilon}}$ and $\delta \bar{\bar{\sigma}}$ express as:

$$\delta \bar{\bar{\epsilon}} = \begin{bmatrix} \delta \epsilon_{11} & 0 & 0 \\ 0 & \delta \epsilon_{22} & 0 \\ 0 & 0 & \delta \epsilon_{33} \end{bmatrix} \quad \delta \bar{\bar{\sigma}} = \begin{bmatrix} \delta \sigma_{11} & 0 & 0 \\ 0 & \delta \sigma_{22} & 0 \\ 0 & 0 & \delta \sigma_{33} \end{bmatrix} \quad (3.17)$$

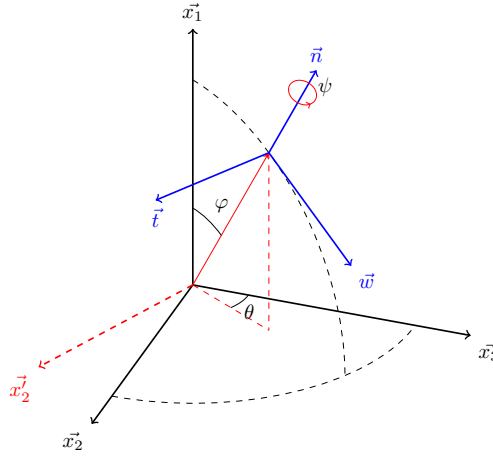


Figure 3.4 Global and local coordinate systems.

The granular assembly is described as a distribution of meso-structures oriented along each direction of the physical space. As shown in Figure 3.4, each meso-structure with respect to a given local frame $(\vec{n}, \vec{t}, \vec{w})$, can be described by Euler angles θ , ϕ and ψ . Thus, a distribution function $\omega(\theta, \phi, \psi)$ which indicates the density of meso-structures associated with the frame $(\vec{n}, \vec{t}, \vec{w})$ is introduced. This function expresses the directional distribution of the meso-structures to describe texture arrangement of the granular assembly. In this thesis, only the isotropic distribution is discussed.

The coordinate transformation from global frame to local frame can be implemented by employing the rotation matrix $\bar{\bar{P}}$, which is computed as the composition product of elementary rotation matrices along axis \vec{x}_1 , \vec{x}_2 and \vec{n} , respectively:

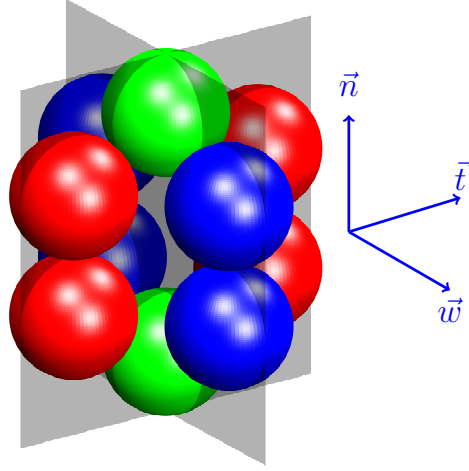


Figure 3.5 The meso-structure of 3D-H model.

$$\bar{\bar{P}} = \begin{bmatrix} 1 & 0 & 0 \\ 0 & \cos \psi & -\sin \psi \\ 0 & \sin \psi & \cos \psi \end{bmatrix} \begin{bmatrix} \cos \varphi & 0 & -\sin \varphi \\ 0 & 1 & 0 \\ \sin \varphi & 0 & \cos \varphi \end{bmatrix} \begin{bmatrix} 1 & 0 & 0 \\ 0 & \cos \theta & -\sin \theta \\ 0 & \sin \theta & \cos \theta \end{bmatrix} \quad (3.18)$$

which gives:

$$\bar{\bar{P}} = \begin{bmatrix} \cos \varphi & -\sin \theta \sin \varphi & -\cos \theta \sin \varphi \\ -\sin \varphi \sin \psi & \cos \theta \cos \psi - \sin \theta \cos \varphi \sin \psi & -\sin \theta \cos \psi - \cos \theta \cos \varphi \sin \psi \\ \sin \varphi \cos \psi & \cos \theta \sin \psi + \sin \theta \cos \varphi \cos \psi & -\sin \theta \sin \psi + \cos \theta \cos \psi \cos \varphi \end{bmatrix} \quad (3.19)$$

Besides, the meso-structure introduced in the following subsection (see [Figure 3.5](#)) is a significant connection between macro-scale and meso-scale. The branch vector relies the centers of particles in contact: $\vec{L} = [l_1, l_2, l_3]^T$, wherein l_1, l_2, l_3 represent the lengths along directions $\vec{n}, \vec{t}, \vec{w}$, respectively. Thus, the kinematic localization gives:

$$\delta \vec{L} = \bar{\bar{P}} \delta \bar{\bar{\epsilon}} \bar{\bar{P}}^{-1} \vec{L} \quad (3.20)$$

$$\text{where: } \delta \vec{L} = \begin{bmatrix} \delta l_1 \\ \delta l_2 \\ \delta l_3 \end{bmatrix}$$

3.2.2 Meso-structure behavior

The meso-structure is composed of ten spherical grains with the identical radius r_g (Figure 3.5). This meso-structure is selected because it includes a grain cluster, large enough to contain four force chains (see Figure 3.6 and Figure 3.7), and enabling grain rearrangement. It can be described analytically, and solved by hand, which is a great advantage. The grain centers respectively belong to two mutually perpendicular planes. Meanwhile, the centers of grains make up two mutually perpendicular hexagon patterns. Thus, the meso-structure can be decomposed into two independent hexagon patterns: Hexagon A and Hexagon B (shown in Figure 3.6 and Figure 3.7). To inherit the features from the H-directional model, this meso-structure is able to lead complicated kinematic mechanisms, including local dilatant and contractant behaviors. To simplify the derivation, it is assumed that each meso-structure is subjected to an external symmetric load. Consequently, only two contacts between grains 1 to 2 and grains 2 to 3, respectively denoted by contact 1 and contact 2, are considered in Hexagon A while two contacts between grains 1 to 7 and grains 7 to 8, denoted by contact 3 and contact 4 are considered in Hexagon B. T_1 is tangential component and N_1 is normal component of the contact force of contact 1. The contact force applied by grain 3 to grain 2 only involves a normal component N_2 , the tangential component is nil due to the symmetry. The relative incremental displacement between grains 1 and 2 is composed of a normal component δu_n^1 and a tangential component δu_t^1 . Likewise, the relative incremental displacement of contact 2 is composed of a single normal component. With respect to Figure 3.3, the

tangential forces G_2 and G_3 are included, so that the moment balance of each grain can be reached. Employing the notations given in Figure 3.6a, it follows that

$$\begin{aligned}\delta u_n^1 &= \delta d_1 \\ \delta u_t^1 &= d_1 \delta \alpha_1 \\ \delta u_n^2 &= \delta d_2\end{aligned}\tag{3.21}$$

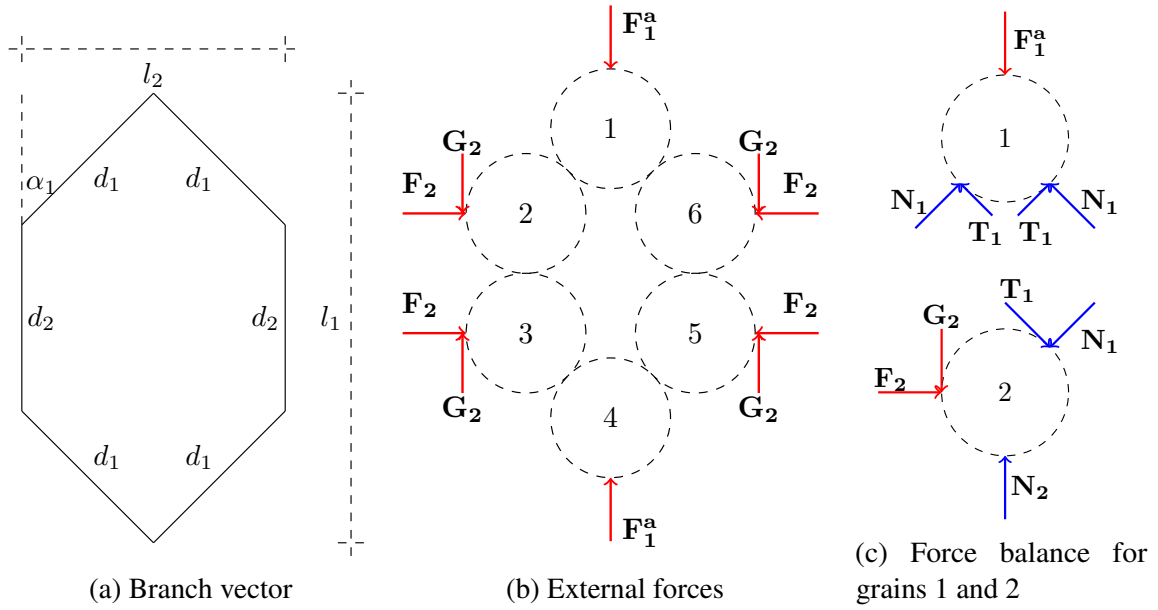


Figure 3.6 Mechanical description of hexagon pattern A.

The geometrical compatibility yields:

$$\begin{aligned}l_1 &= d_2 + 2d_1 \cos \alpha_1 \\ l_2 &= 2d_1 \sin \alpha_1\end{aligned}\tag{3.22}$$

Force balance of grain 1 along direction \vec{n} and of grain 2 along direction \vec{w} and \vec{n} and moment balance of grain 2 read:

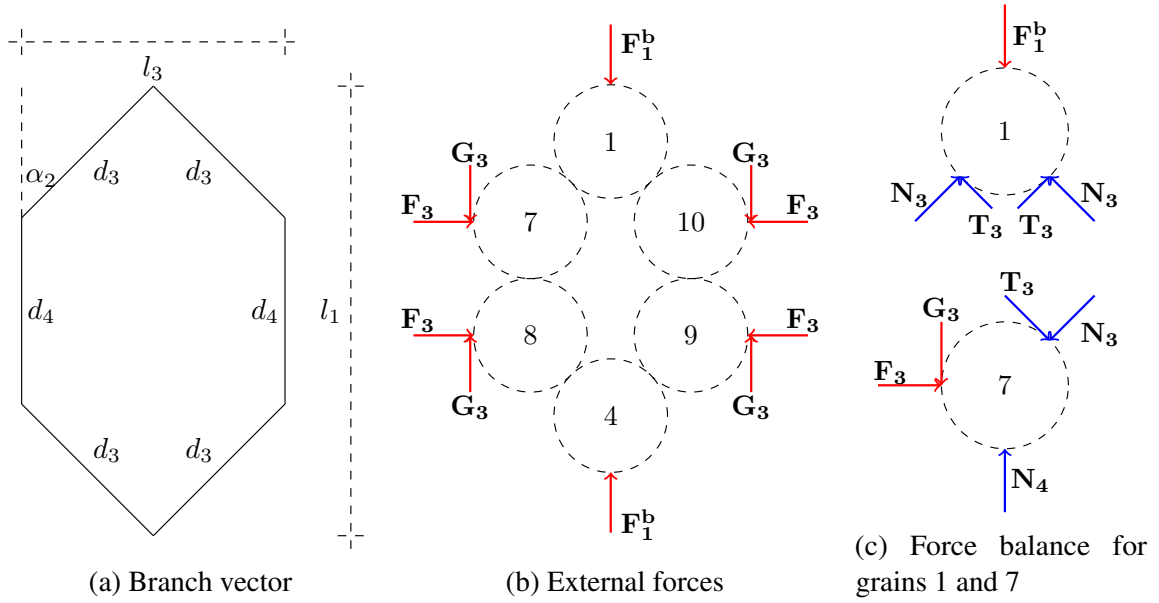


Figure 3.7 Mechanical description of hexagon pattern B.

$$F_1^a = 2(N_1 \cos \alpha_1 + T_1 \sin \alpha_1) \quad (3.23a)$$

$$F_2 = N_1 \sin \alpha_1 - T_1 \cos \alpha_1 \quad (3.23b)$$

$$N_2 = N_1 \cos \alpha_1 + T_1 \sin \alpha_1 + G_2 \quad (3.23c)$$

$$G_2 = T_2 \quad (3.23d)$$

It should be noted that no rolling is assumed to affect particles (Equation 3.23d). This assumption is undoubtedly questionable for spherical shaped grains, where particle rolling acts as an important ingredient of the deformational processes (Kuhn and Bagi, 2004). However, it seems to be reasonable for real granular soil materials where actual grains are angular with multiple facets (Oda et al., 1982, 1997).

The inter-particle contact law expressed in Equations 3.2 is employed. After simplifying (see detail in Appendix A.1), Equations 3.2 can be rewritten as follows:

$$\begin{aligned}\delta N_i &= -k_n \delta d_i \\ \delta T_i &= B_i \delta \alpha_j - A_i \delta d_i + C_i\end{aligned}\quad i = 1, 2, 3, 4 \quad (3.24)$$

For the purpose of simplification, term C_i is negligible. It differs from zero only during a transition from elastic regime to plastic regime. Except this situation, it is zero. For very small strain increments, as considered throughout this paper, term C_i can therefore be neglected.

To obtain the incremental evolution of the external forces, δd_1 , δd_2 and $\delta \alpha_1$ have to be expressed as a function of the meso strain. Three equations are therefore required. Compatibilities (Equations 3.22) provide two relations. The third one is the balance equation of grain 2 along direction \vec{n} (Equation 3.23c). Taking the inter-particle contact law (Equations 3.24) into account leads to the following algebraic system expressing the incremental changes in δd_1 , δd_2 and $\delta \alpha_1$ with respect to the incremental changes in δl_1 and δl_2 :

$$\begin{bmatrix} 2 \cos \alpha_1 & 1 & -2d_1 \sin \alpha_1 \\ 2 \sin \alpha_1 & 0 & 2d_1 \cos \alpha_1 \\ \cos \alpha_1 + \frac{A_1}{k_n} (\sin \alpha_1 + 1) & -1 & \frac{F_2 - B_1 (\sin \alpha_1 + 1)}{k_n} \end{bmatrix} \begin{bmatrix} \delta d_1 \\ \delta d_2 \\ \delta \alpha_1 \end{bmatrix} = \begin{bmatrix} \delta l_1 \\ \delta l_2 \\ 0 \end{bmatrix} \quad (3.25)$$

where A_1, B_1 are given in Appendix A.1.

Differentiating Equation 3.23a, Equation 3.23b and combining with Equations 3.24 gives:

$$\begin{aligned}\delta F_1^a &= -k_n \cos \alpha_1 \delta u_n^1 + k_t \sin \alpha_1 \delta u_t^1 - F_2 \delta \alpha_1 \\ \delta F_2 &= -k_t \cos \alpha_1 \delta u_t^1 - k_n \sin \alpha_1 \delta u_n^1 + F_1^a \delta \alpha_1\end{aligned} \quad (3.26)$$

Thus, combining Equations 3.21, Equations 3.25 and Equation 3.26, the incremental constitutive relation for Hexagon A can be expressed as follows:

$$\begin{bmatrix} K_{11}^a & K_{12}^a \\ K_{21}^a & K_{22}^a \end{bmatrix} \begin{bmatrix} \delta l_1 \\ \delta l_2 \end{bmatrix} = \begin{bmatrix} \delta F_1^a \\ \delta F_2 \end{bmatrix} \quad (3.27)$$

Similarly, the incremental constitutive relation for Hexagon B reads:

$$\begin{bmatrix} K_{11}^b & K_{12}^b \\ K_{21}^b & K_{22}^b \end{bmatrix} \begin{bmatrix} \delta l_1 \\ \delta l_3 \end{bmatrix} = \begin{bmatrix} \delta F_1^b \\ \delta F_3 \end{bmatrix} \quad (3.28)$$

Finally, superimposing Hexagon A and Hexagon B, the total incremental force along direction \vec{n} is $\delta F_1 = \delta F_1^a + \delta F_1^b$. The incremental constitutive relation of the 3D meso-structure can be obtained as follows: (see detail in [Appendix A.2](#))

$$\bar{\bar{K}} \delta \vec{l} = \delta \vec{F} \quad (3.29)$$

$$\text{with } \bar{\bar{K}} = \begin{bmatrix} K_{11}^a + K_{11}^b & K_{12}^a & K_{12}^b \\ K_{21}^a & K_{22}^a & 0 \\ K_{21}^b & 0 & K_{22}^b \end{bmatrix}$$

3.2.3 Stress averaging

Averaging the mesostress taking place within all the meso-structures in the specimen of volume V can be performed as follows:

$$\bar{\bar{\sigma}} = \frac{1}{V} \iiint \omega(\theta, \varphi, \psi) \bar{P}^{-1} \bar{\bar{\sigma}}(\vec{n}, \vec{l}, \vec{w}) \bar{P} \sin \varphi d\varphi d\theta d\psi \quad (3.30)$$

where $\bar{\bar{\sigma}}$ is the macro-stress tensor operating on the specimen scale. For an isotropic specimen, the distribution function $\omega(\theta, \varphi, \psi)$ is constant and $\theta \in [0, 2\pi)$, $\varphi \in [0, \pi]$, $\psi \in [0, 2\pi)$ (θ, φ, ψ are the Euler angles depicted in [Figure 3.4](#)). The mesostress $\bar{\bar{\sigma}}(\vec{n}, \vec{l}, \vec{w})$ with

respect to the local frame can be computed using the Love-Weber's formula (Christoffersen et al., 1981; De Saxcé et al., 2004; Love, 1927; Mehrabadi et al., 1982):

$$\begin{aligned}
 \tilde{\sigma}_{11}(\vec{n}, \vec{t}, \vec{w}) &= 4N_1 d_1 \cos^2 \alpha_1 + 4T_1 d_1 \cos \alpha_1 \sin \alpha_1 + 2N_2 d_2 \\
 &\quad + 4N_3 d_3 \cos^2 \alpha_2 + 4T_3 d_3 \cos \alpha_2 \sin \alpha_2 + 2N_4 d_4 \\
 \tilde{\sigma}_{22}(\vec{n}, \vec{t}, \vec{w}) &= 4N_1 d_1 \sin^2 \alpha_1 - 4T_1 d_1 \cos \alpha_1 \sin \alpha_1 \\
 \tilde{\sigma}_{33}(\vec{n}, \vec{t}, \vec{w}) &= 4N_3 d_3 \sin^2 \alpha_2 - 4T_3 d_3 \cos \alpha_2 \sin \alpha_2 \\
 \tilde{\sigma}_{ij}(\vec{n}, \vec{t}, \vec{w}) &= 0 \quad \text{when } i \neq j
 \end{aligned} \tag{3.31}$$

It should be mentioned that a classical approximation is introduced when averaging the stress: the applied point of each external force is shifted from the grain boundary to the grain center, making it possible to introduce the branch vectors, and to retrieve the usual Love-Weber formula; see for details (Nicot et al., 2013).

The principal components of meso-stress tensor are calculated by the internal forces and the geometric terms of the meso-structure. Besides, off-diagonal components can be simply considered as nil, because the meso-structure with respect to $(\vec{n}, \vec{t}, \vec{w})$ always offsets the one with respect to $(-\vec{n}, -\vec{t}, -\vec{w})$ in off-diagonal components when integrated. This point was carefully checked from a numerical point of view.

3.2.4 Opening angle and void ratio

For a virgin specimen, the initial opening angle is denoted α_0 . Then, $\alpha_1 = \alpha_2 = \alpha_0$. The initial void ratio $e_0(\vec{n}, \vec{t}, \vec{w})$ of each meso-structure belonging to local frame $(\vec{n}, \vec{t}, \vec{w})$ can be estimated by using the initial opening angle α_0 . The volume of the dodecahedron which is made up of the branch vectors of meso-structure can be expressed as follows:

$$V_d = 32r_g^3 \sin^2 \alpha_0 \left(\frac{1}{3} \cos \alpha_0 + \frac{1}{2} \right) \tag{3.32}$$

where: r_g is grain radius; α_0 is the initial opening angle of the meso-structure considered.

The volume of the solid V_s in the dodecahedron includes ten parts. It is easy to calculate the entire volume of the solid, because the volume of the five parts on top side equal the volume of a whole grain. Thus, the entire volume of the solid parts can be calculated as follows:

$$V_s = \frac{8}{3}\pi r_g^3 \quad (3.33)$$

Combining Equation 3.32 and Equation 3.33, the initial void ratio expression is given by:

$$e_0 = \frac{V_d - V_s}{V_s} = -\frac{4}{\pi}\cos^3\alpha_0 - \frac{6}{\pi}\cos^2\alpha_0 + \frac{4}{\pi}\cos\alpha_0 + \frac{6}{\pi} - 1 \quad (3.34)$$

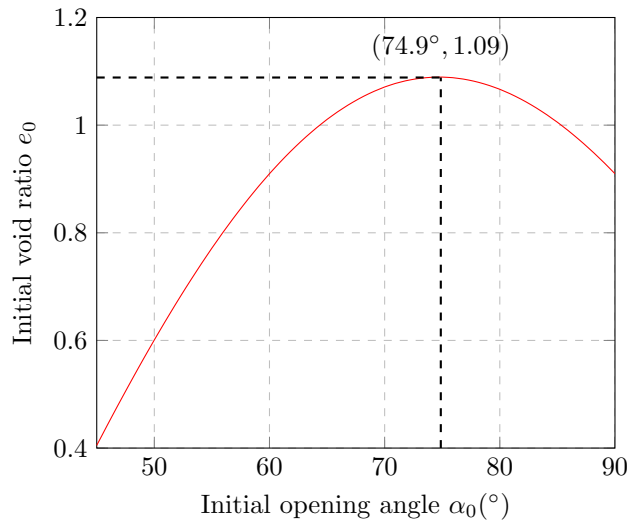


Figure 3.8 Evolution of initial void ratio as a function of initial opening angle.

The evolution of e_0 with respect to angle α_0 (Equation 3.34) is plotted in Figure 3.8, the initial opening angle α_0 is limited due to initial configuration of the meso-structure without overlapping between grains. The minimum value $\alpha_0 = 45^\circ$ corresponds to the condition that the grain 2 is just in contact with grains 7 and 10. The maximum value can reach 90°

when the grains 1 and 4 are touching. In order to estimate the initial opening angle from the initial void ratio, Equation 3.34 is required to become a bijective function. Thus, the domain of α_0 is limited from 45° to 74.9° corresponding to the initial void ratio e_0 from 0.4 to 1.09. Consequently, α_0 can be estimated from e_0 , which is obtained from laboratory test. With the help of this key micro parameter α_0 , the geometric fabric of the meso-structure is determined. However, it should be noted that the maximum and minimum values of e_0 are not the maximum and minimum void ratios of the specimen considered.

3.3 Performances of the 3D-H model

In this section, the performance of the 3D-H model is examined. First, parameters are calibrated by comparing the numerical response of the model with experimental data. Second, one of the most appropriate set of parameters is adopted to carry out prediction tests at different confining pressures. Then, some numerical simulations are conducted along different loading paths to validate the model. As discussed in previous section, the proposed model introduces four parameters: k_n , k_t , ϕ_g (material parameters), and e_0 , wherein the initial void ratio e_0 corresponding to opening angle α_0 can be estimated from Equation 3.34.

3.3.1 Parameter calibration and model prediction

The calibration of the present model can be performed from the comparison between numerical and experimental results. The experiment was carried out along the conventional drained triaxial loading path with mono-disperse sand ($d_{50} = 0.6mm$) called Ticino sand, well characterized from a geotechnical point of view and adopted in many studies (Valentino et al., 2008).

Conventional triaxial compression test (CTC) at 200 kPa of confining pressure is adopted to calibrate the model parameters by considering two responses: (1) the stress-strain response; (2) the volumetric response. Figure 3.9 shows the numerical result in comparison with the experimental result, where the experimental curves are well reproduced using the set of parameters reported in Table 3.1.

Table 3.1 Parameters selected in calibration and prediction phases

$k_n/r_g(N/m^2)$	k_n/k_t	e_0	$\phi_g(^{\circ})$	Initial isotropic stress $p_0(\text{kPa})$
1.90×10^9	0.6	0.53	25	100, 200, 300 and 400

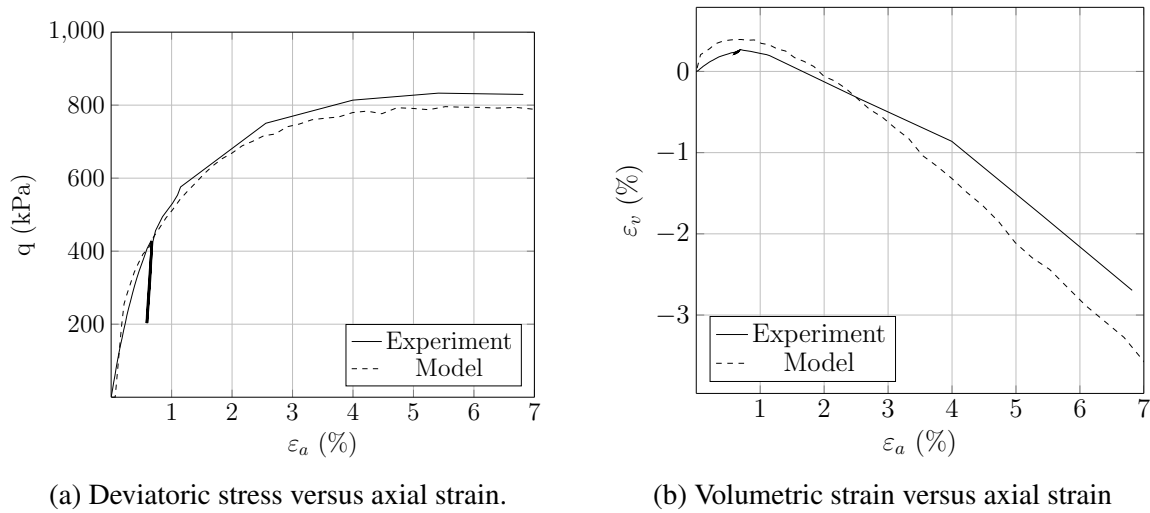


Figure 3.9 Calibration phase of the model at 200 kPa of confining pressure.

Figure 3.10 shows the model predictions of deviatoric stress and volumetric strain plotted against axial strain at different confining pressures. The calibrated parameters reported in Table 3.1 are employed. Evidently, the model predictions agree fairly well with the experimental curves in terms of both the stress-strain relation and volumetric responses. As shown in Figure 3.10a, the numerical curve rises lower than the experimental curve at 300 kPa of confining pressure while higher at 100 kPa. Figure 3.10b plots the volumetric strain ε_v versus axial strain ε_a . The experimental curves are reproduced well, illustrating the capability of this model.

In general, the calibration and prediction evidence satisfying results. The present model captures well the experimental curves with only four parameters. The microscopic geometrical parameter α (see Figure 3.6a and Figure 3.7a) evolves independently during loading paths, which will be further discussed subsequently.

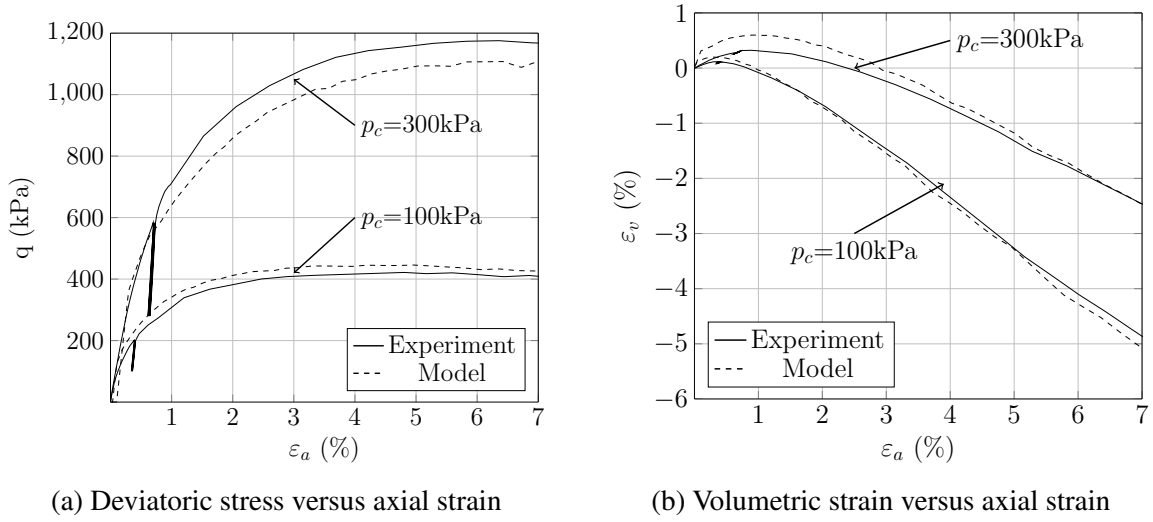


Figure 3.10 Prediction capability of the model at 100 kPa and 300 kPa of confining pressures.

3.3.2 Triaxial loading paths

CTC tests at different confining pressures are selected to show how the proposed model simulates the behavior observed for sands. For demonstration purpose, the simulations at 100 kPa, 200 kPa and 400 kPa confining pressures are compared in Figure 3.11 from $\varepsilon_a = 0\%$ to $\varepsilon_a = 25\%$. The parameters reported in Table 3.1 are adopted.

Figure 3.11a shows that the deviatoric stress q reaches a peak at a small strain about $\varepsilon_a = 5\%$ and undergoes a subsequent softening regime until critical state regime develop. As shown in Figure 3.11b, the deviatoric stress q triple increases as the mean stress p during the triaxial loading path. The volumetric strain responses at different confining pressures are displayed in Figure 3.11c, where a dilatancy can be observed before the critical state, except a sensible contractancy captured at the beginning. Figure 3.11d plots the void ratio e

versus the mean stress p in logarithms form. The curves are increasing until the critical state line. The evolution of the void ratio can be observed in Figure 3.11e where the volumetric strain ε_v firstly decreases and then increases until a plateau is reached. Figure 3.11f gives the deviatoric ratios q/p plotted against the axial strain ε_a . The peak of deviatoric stress ratio increases as the initial confining pressure decreases. All the curves converge toward more or less the same value, close to 1.25. In 3D conditions, the deviatoric ratio is related to the mobilized macroscopic friction angle, as:

$$\frac{q}{p} = \frac{6 \sin \varphi_c}{3 - \sin \varphi_c} \quad (3.35)$$

which gives $\varphi_c \sim 31.15^\circ$ when $q/p = 1.25$

Besides, additional three CTC tests are carried out at a same initial confining pressure, namely 200 kPa, with different initial void ratios $e_0 = 0.43$, $e_0 = 0.53$, $e_0 = 0.63$. As shown in Figure 3.12a, the deviatoric stress q reaches different peaks due to the effect of different initial void ratios. The peak of the curve corresponding to $e_0 = 0.53$ (the densest specimen) rises higher than the curve corresponding to $e_0 = 0.63$ (the loosest specimen). In Figure 3.12b, the void ratio slightly decreases at the beginning and then increases until the critical void ratio at the end, where a convergence tendency can be observed. Conversely, the loosest specimen reaches a higher critical void ratio than the densest one. As shown in Figure 3.12c, the volumetric strain curve decreases before $\varepsilon_a = 2\%$ and increases until critical state. The densest specimen response is more dilatant than that of the loosest one. Figure 3.11d plots the axial strains versus the deviatoric ratios, which shows that the largest initial void ratio brings out the lowest peak in deviatoric ratio q/p , corresponding to the highest macroscopic friction angle φ_c . It is very challenging for a stress-strain model to reproduce the critical state, when no specific assumptions are introduced. However, by the proposed model it is

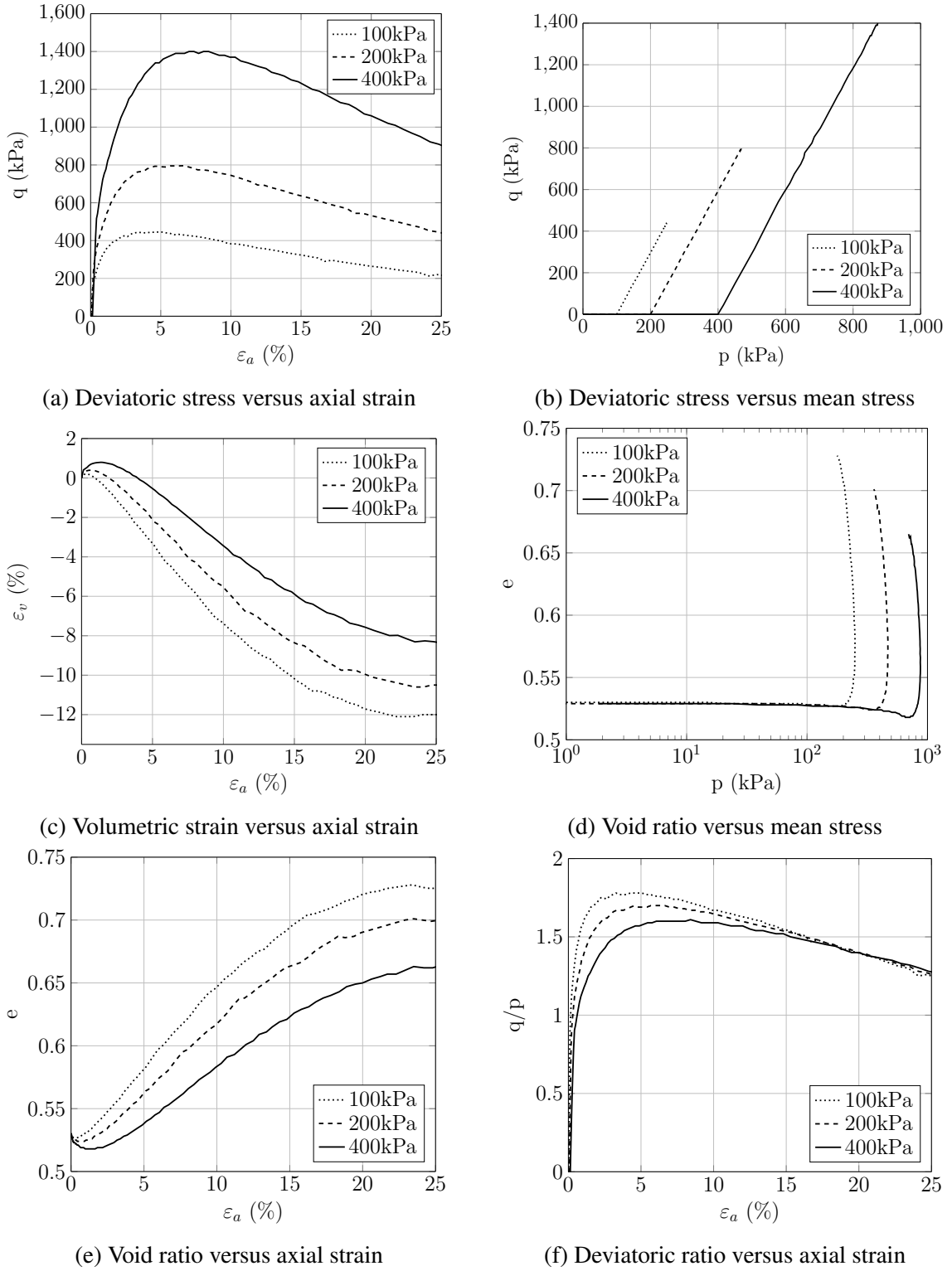


Figure 3.11 Effect of different initial confining pressures on model responses along an axisymmetric drained triaxial loading path.

observed that the critical state is not perfectly obtained, but is reached approximately, giving rise to a critical state regime tendency.

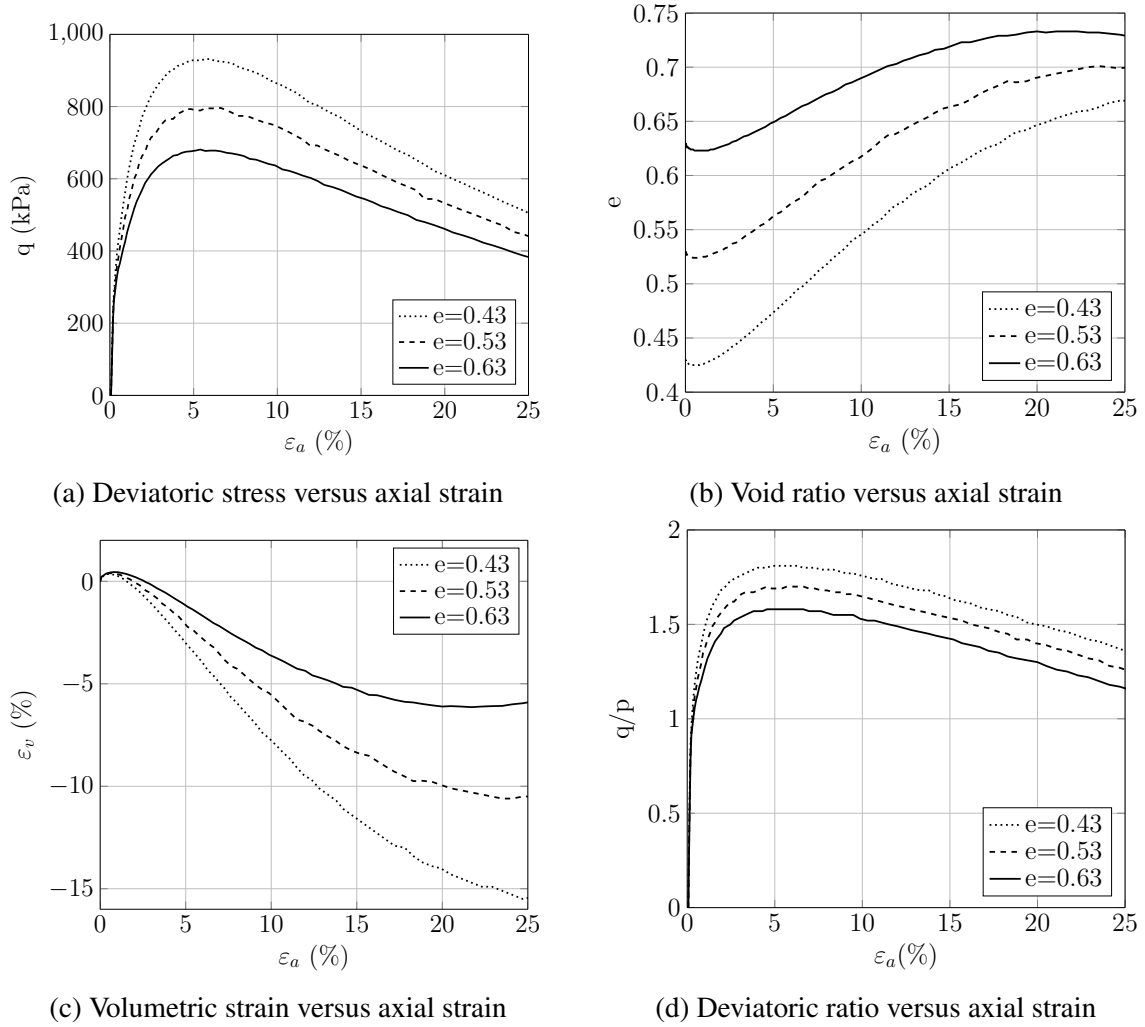
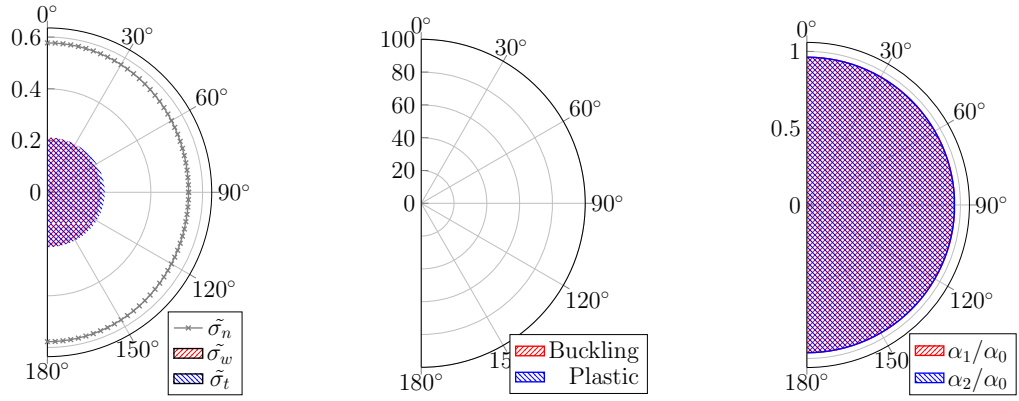
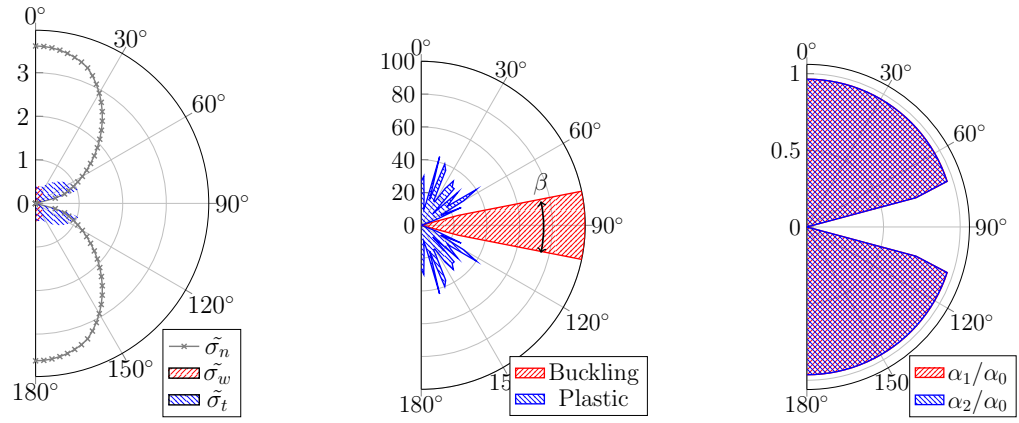
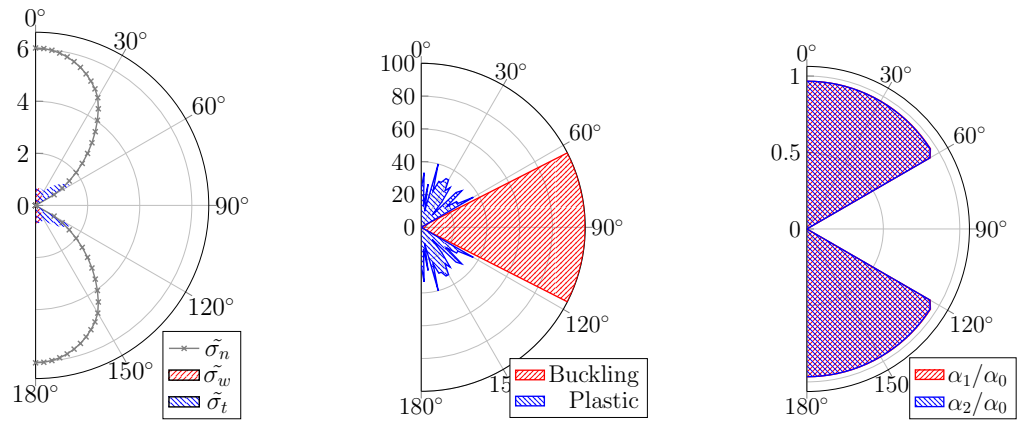


Figure 3.12 Effect of different initial void ratios on the model response along an axisymmetric drained triaxial loading path.

It is noticed that the hardening and softening behavior, including the qualitatively described critical state, can be illustrated from a micro-mechanical point of view. The 3D distributions over angle θ of micro variables including micro stresses ($\tilde{\sigma}$), contact information and opening angles ($\alpha_{1(2)}$) involve three Euler angles (θ , φ and ψ see Figure 3.4). For the purpose of simplification, these 3D micro variables can be integrated either over φ , ψ or over θ , ψ . Considering the drained triaxial loading path, the former is selected. The

angular distributions of micro variables at different strain states, with 200 kPa confining stress, are illustrated in [Figure 3.13](#). In each sub-figure, three polar figures are shown: the integrated micro stress $\iint \omega \tilde{\sigma}_n d\theta d\psi$, $\iint \omega \tilde{\sigma}_t d\theta d\psi$ and $\iint \omega \tilde{\sigma}_w d\theta d\psi$ (left column); the percentage of plastic or buckling meso-structures (center column); the mean normalized opening angle $(\alpha_1/\alpha_0, \alpha_2/\alpha_0)$ (right column). It should be mentioned that the buckling area in the center column denotes the percentage of meso-structures at a certain value of θ . As a meso-structure is buckling, $\tilde{\sigma}$ and $\alpha_{1(2)}$ are set to zero. The contact buckling is a significant feature of the present model, which makes it possible to simulate the persisting loss of contacts corresponding to the so-called force-chains buckling.

Initially, all of the meso-structures are created following an isotropic distribution with same initial opening angle $\alpha_0 = 41.56^\circ$. [Figure 3.13\(a\)](#) corresponds to the end of the isotropic compression phase, where the micro stress and opening angle are isotropically distributed. Each meso-structure evolves independently, giving rise to different local relative displacements in terms of the kinematic localization ([Equation 3.20](#)). During the isotropic compression phase, neither buckling nor plastic meso-structure can be observed, which indicates that the specimen still behaves in an elastic regime. As shown in [Figure 3.13\(b\)](#), $\iint \omega \tilde{\sigma}_n d\theta d\psi$ plays a major role along the axial compression direction ($\varphi = 0$ or 180°), which shows an anisotropic micro stress state. The meso-structures oriented within a central cone (angle β , the circumferential angle of the buckling cone) become buckling, because the meso-structures in this cone dilate too much in order to keep the constant confining stress. Meanwhile, more than 20% of meso-structures reach a plastic regime in the rest of area. Afterwards, [Figure 3.13 \(c,d,e and f\)](#) shows the evolution of micro variables during the triaxial loading path. In the left column, micro-stress increases in the non-buckling area as β also increases in the center column. Thus, the macro stress-strain response can be better illustrated from these micro state variables. If the micro-stress increases significantly, the macro-stress raises. Otherwise, if the buckling regime becomes dominant, the macro-stress

(a) $\varepsilon_a = \varepsilon_0$ (isotropic)(b) $\varepsilon_a = 0.25\%$ (c) $\varepsilon_a = 0.5\%$

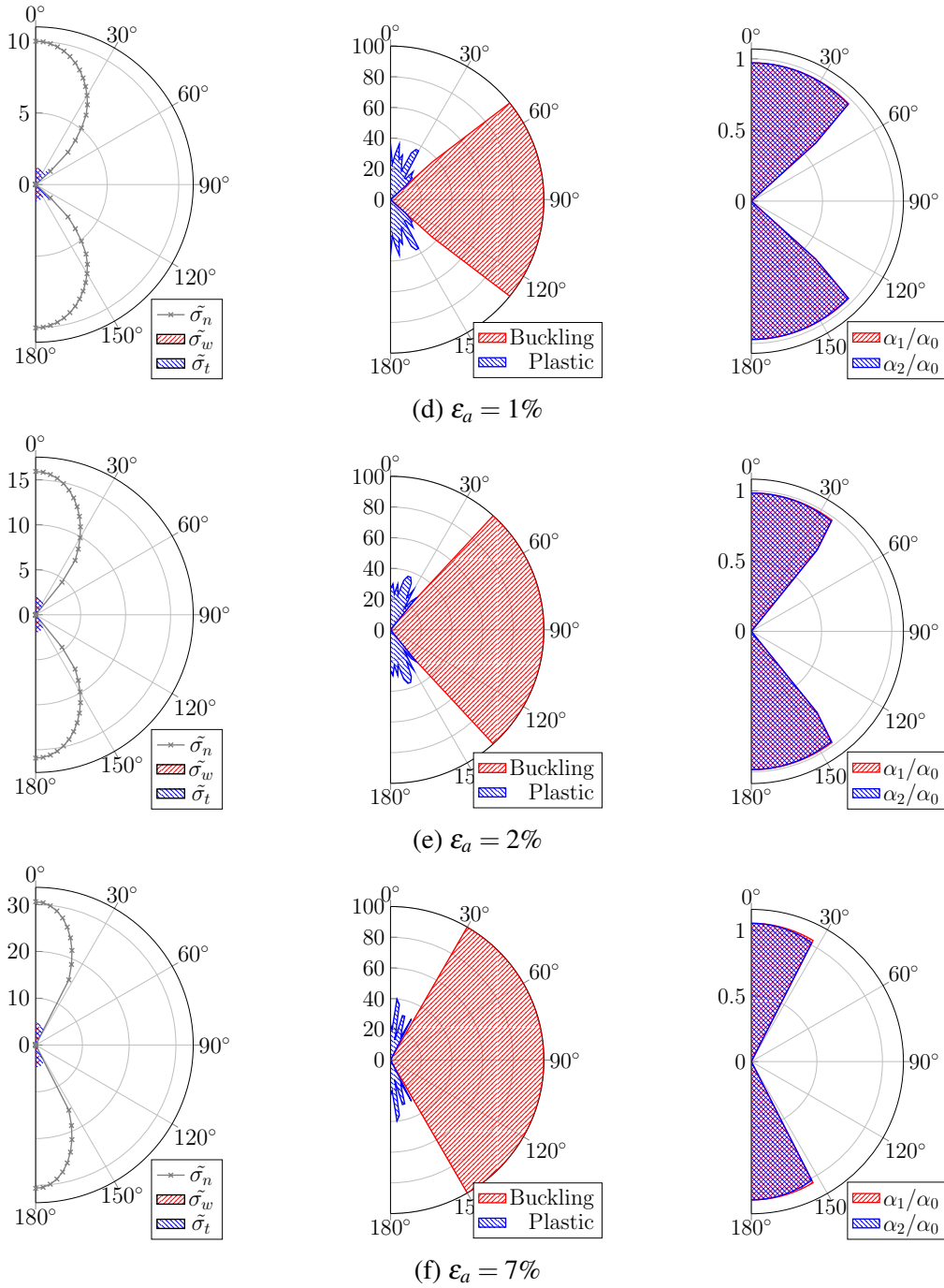


Figure 3.13 Angular distributions of micro variables along θ at different strain states, with 200 kPa of the confining stress: the integrated micro stress $\iint \omega \tilde{\sigma}_n d\theta d\psi$, $\iint \omega \tilde{\sigma}_t d\theta d\psi$ and $\iint \omega \tilde{\sigma}_w d\theta d\psi$ (N) (left column); the percentage of plastic or buckling meso-structures (center column); the mean normalized of the opening angles (α_1/α_0 , α_2/α_0) (right column).

decreases. Moreover, the increasing and decreasing tendencies of the macro-stress can reach a balance corresponding to the macro-stress plateau. Both buckling and plastic regimes of the present model cannot be reversed, which directs the softening behavior observed on the macro scale. Additionally, slightly growing of opening angles α_2 and α_3 can be observed in the right column. It is a key geometrical parameter, which has a tremendous influence on the micro forces within the meso-structure. This geometrical parameter also reveals the rearrangement of the specimen. The relative position between particles is directed not only from the single contact relation, but is also governed by the geometrical configuration described by this key parameter.

3.4 Closing remarks

There are two aspects to be considered in the constitutive modeling of the granular materials using a multi-scale approach. First, the macroscopic constitutive relation should be properly related to the microscopic features, that is to say, the local behaviors on the contact scale, from which the macroscopic behavior stems. The more properly this point is achieved, the more realistic the constitutive model's performance will be. Another concern is to decrease the computational complexity as much as possible with reasonable assumptions, in order to avoid handling an exceeding number of local balance equations, for all the particles. To most cases, involving more mechanical details in the micro-scale and decreasing the computational complexity are paradoxical. In past decades, many researchers explored different routes between these two aspects, trying to find an optimized solution in favor of both. However, an optimized solution can be obtained only if the microscopic behavior of the granular material can be deeper understood. This chapter gives an example of the attempt to find this optimized solution.

In this chapter, the micro-directional model and the H-model are first reviewed. The former states that the microscopic fabric of the material consists of individual contacts independent from each other and oriented along different directions. As the incremental strain is affinely projected onto all individual contacts, incremental forces are simultaneously generated according to the local constitutive relation, namely, the contact law. Then the global stress can be obtained by integrating all contacts forces in the way given by the Love formula. This model succeeds to relate the macro-scale properties to micro-scale ones by employing an assumed fabric. However, strong shortcomings have been noted. To overcome such limitations, the H-model is introduced, which replaces individual contacts by individual hexagonal patterns. The local behavior from the contact law is replaced with the local constitutive relation of the hexagon, in which contacts are never independent but internally compatible with each other.

based on the homogenization scheme used in the micro-directional model and the H-model, the latter is extended to 3D conditions by replacing the 2D hexagonal pattern with a 3D meso-structure. For this purpose, a decomposition and superimposition approach is introduced to analyze the local behavior of the meso-structure. The 3D-H model only introduces four parameters, wherein k_n , k_t and ϕ_g relate to the elastic-perfect plastic inter-particle contact law. The last one (the opening angle α_0) is a key microscopic geometrical parameter which can be estimated from the initial void ratio. It is noteworthy that the granular assembly rearrangement can be reflected by the evolution of the opening angle α_0 .

By comparing with experimental results on Ticino sands, the calibration of the model is carried out and the predictive capabilities are examined along drained triaxial compression loading paths. The results obtained are both qualitatively and quantitatively satisfying. The hardening and softening regimes are reproduced well in the stress-strain response. Meanwhile, the dilatant and contractant regimes are also well captured by the volumetric strain curve. By adopting the calibrated parameters, two sets of numerical tests are run, including different

confining stresses and initial void ratios. One of the most significant findings emerging from this study is that the critical state can be approximately described from void ratio evolution without involving any CSL formulations and associated parameters. The model mechanism is also analyzed from a microscopic point of view. The angular distributions of micro variables are plotted at different strain states under the drained triaxial loading path, giving important information about the microstructure evolution.

Chapter 4

Finite element implementation of the 3D-H model

A 3D multi-scale approach is presented to investigate the mechanical behavior of a macroscopic specimen consisting of a granular assembly, as a boundary value problem. The core of this approach is a multiscale coupling, wherein the finite element method is used to solve a boundary value problem and a micromechanically-based model is employed as constitutive relationship used at a representative volume element scale. This approach provides a convenient way to link the macroscopic observations with intrinsic microscopic mechanisms. The plane-strain triaxial loading condition is selected to simulate the occurrence of strain localization. A series of tests are performed, wherein distinct failure patterns are observed and analyzed. A system of shear band naturally appears in a homogeneous setting specimen. By defining the shear band area, microstructural mechanisms are separately investigated inside and outside the shear band. Moreover, a second-order work directional analysis is performed by applying strain probes at different stress-strain states along drained triaxial loading paths. The normalized second order work introduced as an indicator of instability occurrence is analyzed not only on the macroscale but also on the microscale.

4.1 The Finite Element Method

The finite element method (FEM) is perchance the most effective and famous numerical method ever devised for approximately solving boundary value problems (BVP), i.e. sets of differential equations applied to a domain with prescribed boundary conditions. Examples of BVPs abound in real life. In the field of geotechnical engineering, BVPs not only exist at the laboratory scale but also exist in geotechnical engineering problems, for instance, the footing case as a foundation supporting loads from a structure, water/fluid flowing through an embankment dam, a tunnel being excavated and a footing located near a slope.

In a broad sense, the FEM basically consists of:

- transforming the set of governing equations to a weak form;
- dividing/discretizing the domain of the problem into smaller geometrically simpler subdomains, i.e. finite elements; and
- using proper approximating solutions.

The constitutive relation plays a significant role in the FE stress-strain analysis because it establishes the connection between stresses (forces) and strains (displacements) for the material (structure). Using a constitutive model making it possible to describe the material behavior can produce misleading FE results that, as a result, if applied to engineering design, may lead to grievous consequences. The analysis of structures contacting with geomaterials requires caution, for the reason that the mechanical behavior of these materials is very complex. It is essential to use proper and effective constitutive models such as the micromechanically-based models.

Aside from picking up a reliable constitutive model, it is also relevant that the FEM code is robust and able to deal properly with issues that arise within numerical methods

themselves, for instance, hourglassing, patch test. As already alluded in the introduction of this research work, computations are here carried out using the commercial software Abaqus v6.11 (<http://www.simulia.com>). Abaqus is a commercial package of FEM-based programs designed to simulate a wide variety of engineering problems ranging from relatively simple linear analyses to more complex nonlinear ones. This software allows users to define their own constitutive model through a facility subroutine called VUMAT. Moreover, extensively detailed manuals with theory and example accompany the package. Also, a great number of users and forums can be found on the internet. A few more details about Abaqus and the user material subroutine VUMAT can be encountered in Appendix B of this dissertation.

The FEM code (ABAQUS/Explicit) (Hibbitt and Sorensen, 2001) is used to solve BVPs in the context of this multi-scale approach. An arbitrary geometric domain Ω of a given BVP is firstly discretized into apposite FEM meshes with geometric position \vec{x} . The discretized equilibrium equation for the whole mesh reads:

$$\vec{F}^e - \vec{F}^i = \bar{\bar{M}}\ddot{\vec{u}} \quad (4.1)$$

where \vec{F}^e is the external force vector; \vec{F}^i is the internal force vector; $\bar{\bar{M}}$ is the mass matrix and $\ddot{\vec{u}}$ is the displacement of each material point \vec{x} .

The internal force vector is given by:

$$\vec{F}^i = \bar{\bar{K}}\vec{u} \quad (4.2)$$

where $\bar{\bar{K}}$ is the stiffness matrix, calculated from the 3D-H model (constitutive relation) and the interpolation assumption (geometric relation) in the element.

Thus, for a dynamic equilibrium state at the current time (t):

$$\bar{\bar{M}}\ddot{\vec{u}}|_t = (\vec{F}^e - \vec{F}^i)|_t \quad (4.3)$$

The central difference integration scheme is used to update velocities and displacements:

$$\begin{cases} \vec{u}|_{(t+\frac{\Delta t}{2})} &= \vec{u}|_{(t-\frac{\Delta t}{2})} + \left(\frac{\Delta t|_{(t+\Delta t)} + \Delta t|_t}{2} \right) \ddot{u}|_t \\ \vec{u}|_{(t+\frac{\Delta t}{2})} &= \vec{u}|_t + \Delta t|_{(t+\Delta t)} \ddot{u}|_{(t+\frac{\Delta t}{2})} \end{cases} \quad (4.4)$$

The geometry is updated by adding the displacement increments to the initial geometrical configuration \vec{x}_0 :

$$\vec{x}_{t+\Delta t} = \vec{x}_0 + \vec{u}_{t+\Delta t} \quad (4.5)$$

As the mass matrix \bar{M} in [Equation 4.3](#) is diagonalized (or lumped), its inversion is trivial, and the system of differential equations decouples. Its overall solution can then be performed independently and very fast for each degree of freedom. Further reductions of the computation time per time increment stem from a utilization of reduced integration schemes that are often applied even to the deviatoric parts of the stiffness matrix, and finally numerical actions related to mass scaling and load factoring also contribute to the reductions of the computation.

Additional computational advantages result from the fact that dynamic explicit schemes, unlike quasi-static implicit schemes, do not check equilibrium requirements at the end of each increment of time. The analogy between the dynamic equilibrium [Equation 4.1](#) and the ideal mass-spring vibrating system allows concluding that explicit central difference time integration schemes (frequently referred to as explicit integration schemes) are conditionally stable according to the magnitude of the time increment Δt :

$$\Delta t \leq \frac{L_e}{E/\rho} = \frac{L_e}{c_e} \quad (4.6)$$

where L_e is the typical size of the finite elements discretizing the domain, E is the elasticity modulus and c_e is the propagation velocity of a longitudinal wave in the material. In case of metal forming applications, the stability condition [Equation 4.6](#) requires the utilization of very small increments of time Δt , say microseconds, and millions of increments to finish a simulation because industrial metal forming processes usually take several seconds to be accomplished. This is the reason why computer programs often make use of the following numerical actions in order to increase the increment of time Δt and, consequently, reducing the overall computation time:

- Diagonalization of the mass matrix;
- Mass scaling—by increasing the density of the material and thus artificially reducing the speed c_e of the longitudinal wave;
- Load factoring—by changing the rate of loading through an artificial increase in the velocity of the tooling as compared to the real forming velocity;
- Reduced integration of the deviatoric part of the stiffness matrix, which is usually fully integrated.

4.2 Multi-scale approach implementation

The FEM implementation of the 3D-H model constitutes a complete multi-scale procedure. In FEM, the cell is usually called 'microscale' due to the fact that it is one of the fundamental elements of a BVP. However, this cell can also be called 'macroscale', because it is the REV in DEM. To clarify, different scales involved in this multi-scale approach are depicted in [Figure 4.2](#). Gauss integration points in the FEM mesh correspond to the REV scale at which the 3D-H model operates. Two intermediate scales (hexagon scale and REV scale)

are introduced to bridge macro and micro scales. The element type named C3D8R (three-dimensional eight-node brick element with reduced integration) is selected. The schematic diagram of the framework is depicted in [Figure 4.1](#) and can be illustrated by the following steps:

- (1) From macro-scale to the REV scale, the BVP is solved by using ABAQUS dynamic-explicit solver. The macro-strain of each element is computed, and then transferred to the REV scale.
- (2) From the REV scale to the meso-scale, the 3D-H model is employed. The macro-strain is distributed to local meso-structures by using kinematic localization ([Equation 3.20](#)). Thus, the strain of the meso-structure is obtained.
- (3) From the meso-scale to the REV scale, the constitutive relation of the meso-structure is firstly obtained, then the internal forces within the meso-structure are calculated. By using Love's formula, the stress within the REV is calculated.
- (4) From the REV scale to the macro-scale, the macro-stress is computed after all the stresses acting at integration points are calculated.

4.3 Finite Element Model and benchmark

4.3.1 Finite Element Model

In order to examine the performance of the multiscale approach elaborated in previous chapter, the numerical analysis presented in this chapter mainly focuses on plane-strain triaxial compression loading conditions. As shown in [Figure 4.3](#), the specimen with size: $0.2(\vec{x}_1) \times 0.1(\vec{x}_2) \times 0.005(\vec{x}_3) m^3$ is assembled between two rigid bars. The degree of freedom along \vec{x}_3 of the whole model is blocked while the confining stress is applied along \vec{x}_2 .

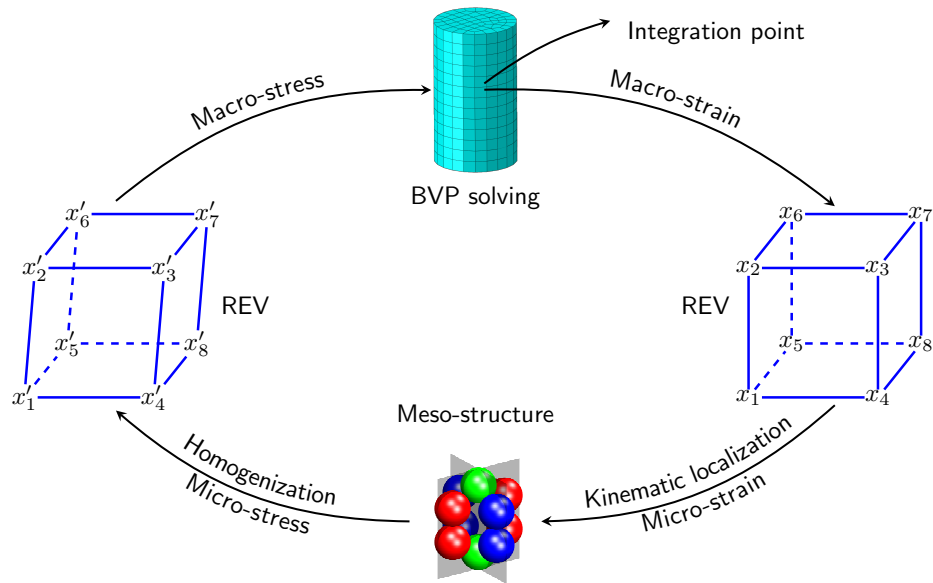


Figure 4.1 The schematic diagram of multi-scale approach based on the 3D H-model.

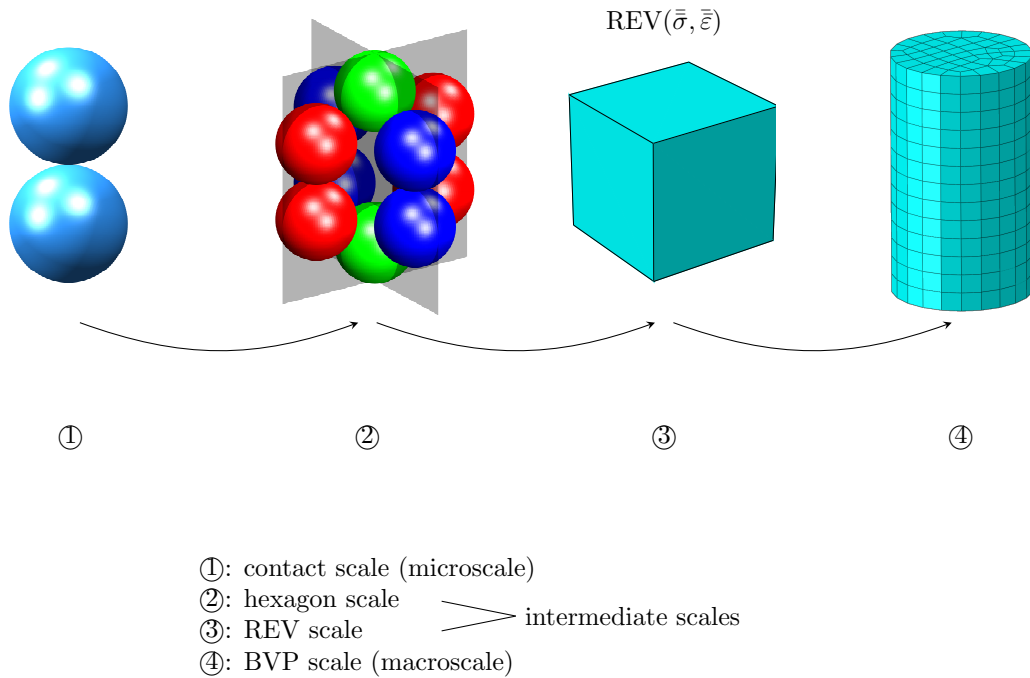


Figure 4.2 Different scales involved in the multi-scale approach.

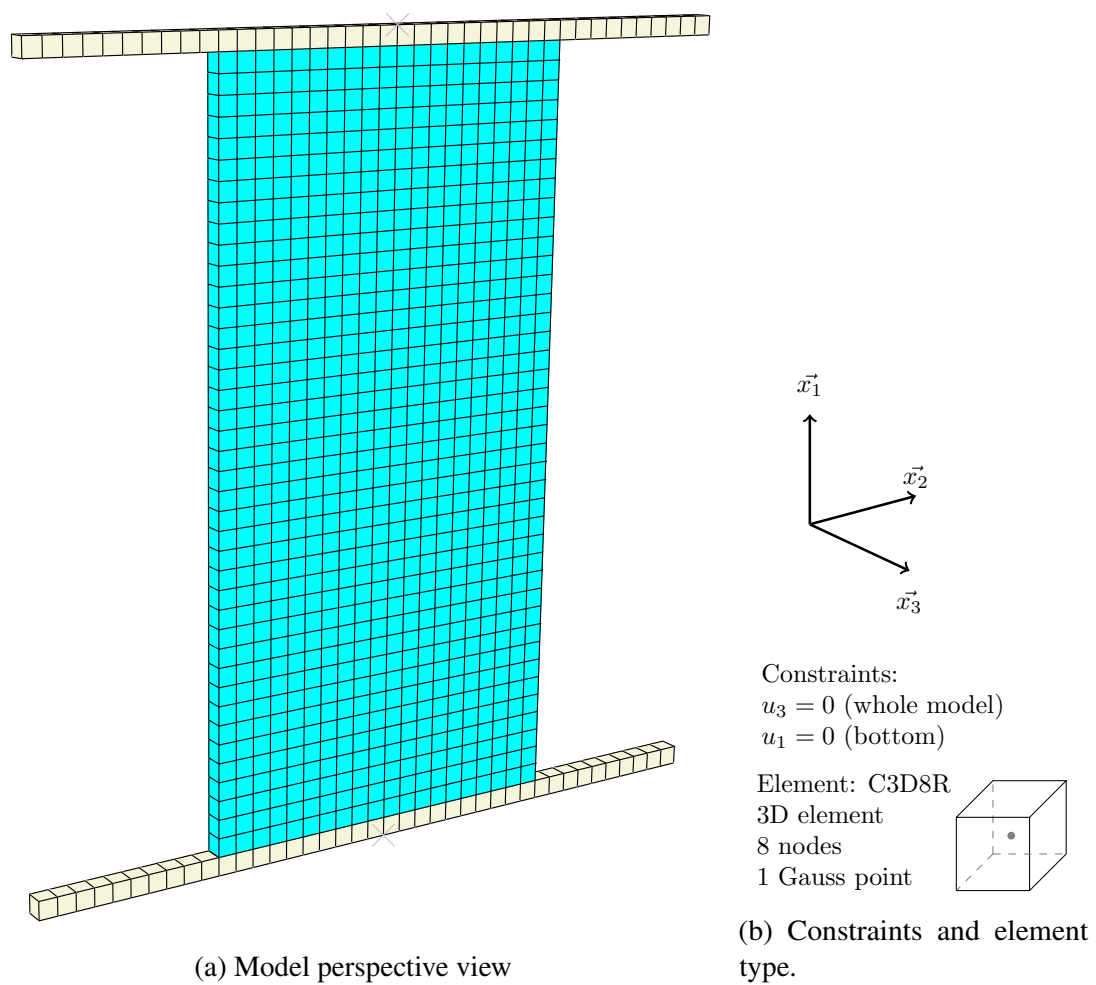


Figure 4.3 Model constraints and element type.

4.3.2 Calibration and verification

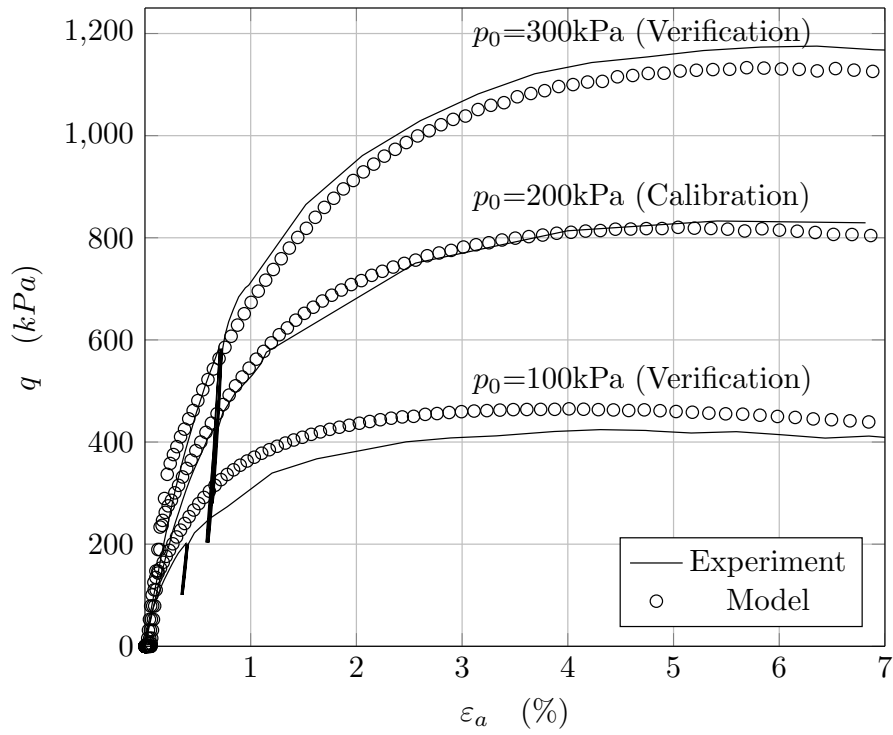
In relation with the elastic-perfect plastic inter-particle contact law, it is worth noting that this multiscale approach involves only three material parameters and one micro geometrical parameter. The formers including the normal stiffness (k_n), tangential stiffness (k_t), inter-particle friction angle (φ_g) stem from the contact law, while the latter is the opening angle (α_0) calculated from the initial void ratio. Thus, four parameters need to be calibrated. It is worth noting that, the 3D-H model was calibrated in [chapter 3](#) with a homogeneous specimen under homogeneous conditions. In contrast with [chapter 3](#), the calibration procedure in this chapter is based on solving the boundary value problem with a meshed volume by using FEM model. The parameters are determined by trial and error in order to provide the best fit to a single isotropically compressed drained triaxial test confined at 200 kPa on Ticino sand with $D_R = 74\%$ of relative density. The best fit of $D_R = 74\%$ is shown in [Figure 4.4](#) while the employed parameters are reported in [Table 4.1](#). Afterwards, these parameters are used to examine the model predictive capability by comparing the experimental data from the drained triaxial test confined at 100 kPa and 300 kPa. The results are observed in [Figure 4.4](#), where the predicted curves are in agreement with the experimental curves.

Table 4.1 Parameters selected in calibration and prediction phases

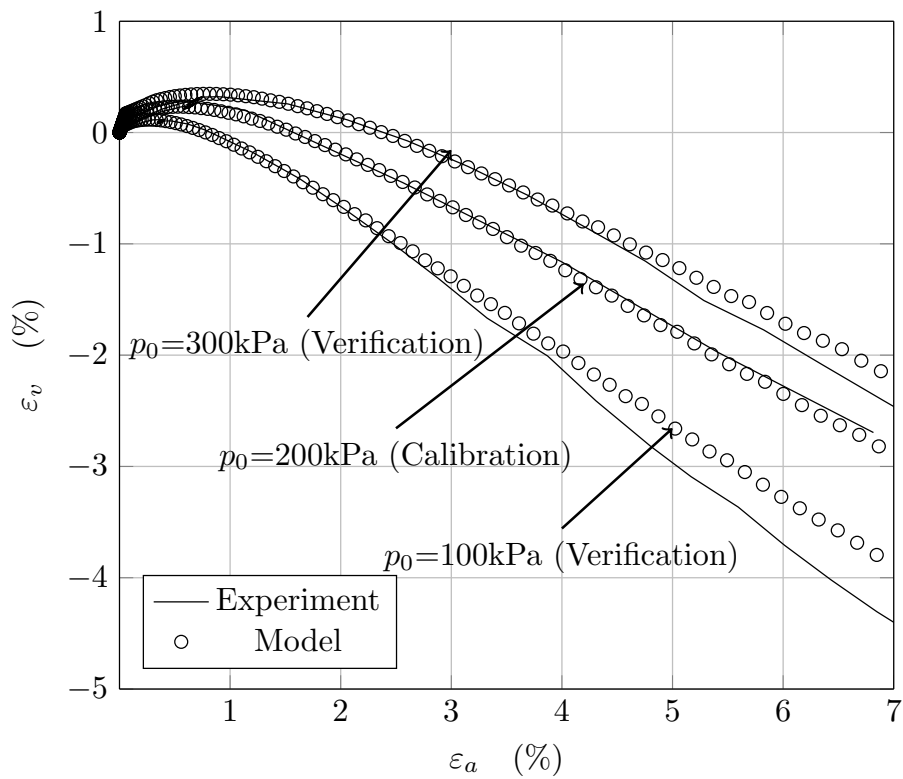
$k_n(\text{N/m})$	$k_t(\text{N/m})$	e_0	$\varphi_g(^{\circ})$
1.90×10^6	1.14×10^6	0.53	25

4.3.3 Mesh dependency

In order to assess the sensitivity of finite element mesh for the localization analysis, five cubic mesh patterns with different elements are considered. [Figure 4.5](#) shows the mechanical responses for all the mesh patterns along drained triaxial loading paths at 200 kPa of confining stress. It is remarkable that whatever the mesh is, the hardening phase is the same ($\epsilon_a < 3.6\%$).



(a) Mechanical response.



(b) Volumetric response.

Figure 4.4 Parameters calibration and model verification using the triaxial compression test on Ticino sand ($D_R = 74\%$).

Afterwards, the curves reach the stress peak, and a softening behavior can be observed, where the more elements are used, the deeper the deviatoric stress drops. The softening phase reveals a mesh dependency stemming from the strain localization. As shown in Figure 4.6, no visible strain localization can be observed with 50 elements and 200 elements, whereas it evidently exists with 406 elements, 595 elements, 800 elements and 1653 elements. Due to the strain localization, a given increment of top loading displacement is no longer accommodated by all the elements in the whole specimen, but localized through a much marked shear deformation in the band. However, the different curves tend toward a unique one when the number of elements is increased. Besides, taking into account the computational efficiency, the mesh with 800 elements is used hereafter.

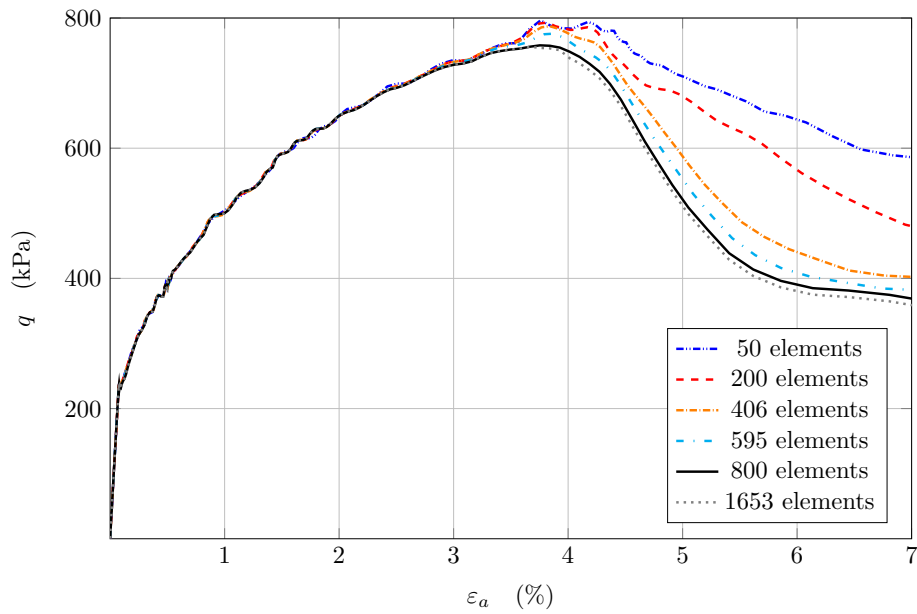


Figure 4.5 Mechanical response with different mesh patterns under the drained triaxial loading path at 200 kPa of confining stress.

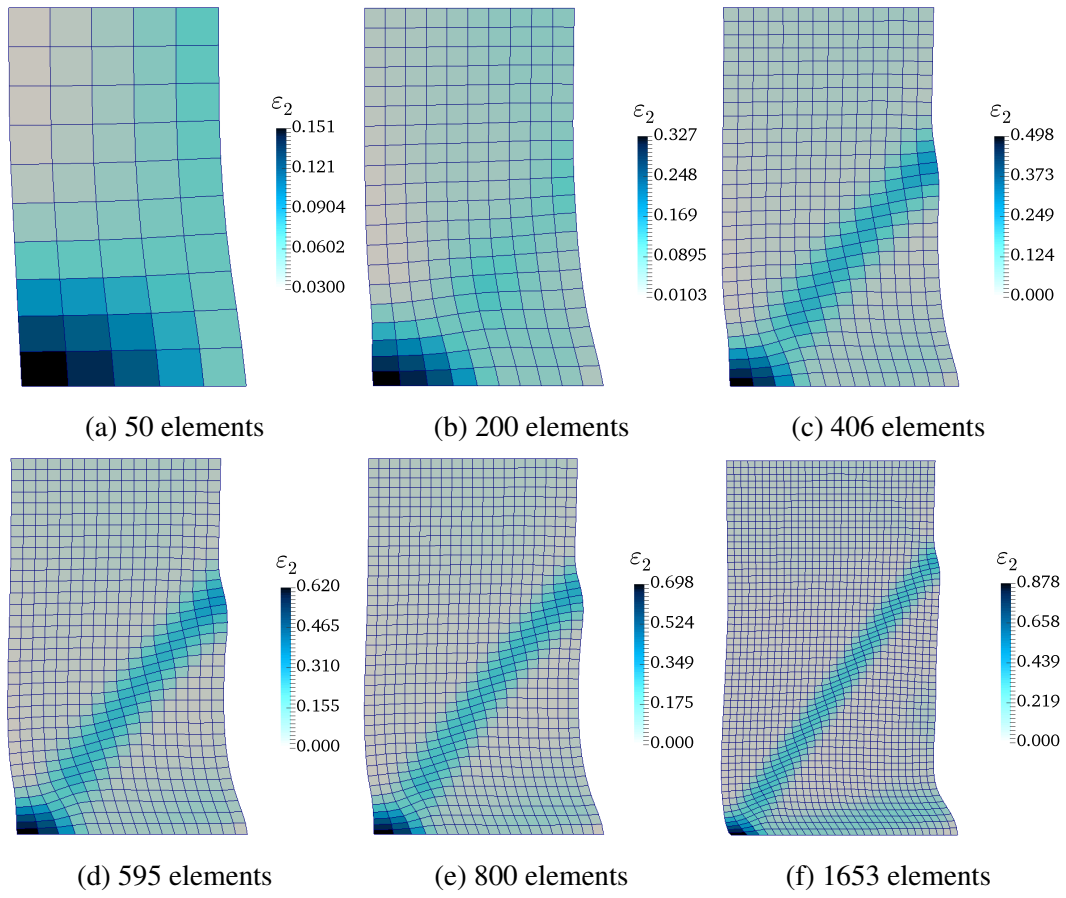


Figure 4.6 Contours plotting of element strain ε_2 for the deformed configuration at the axial strain $\varepsilon_a = 6\%$.

4.4 Drained triaxial tests

The plane-strain model with 800 elements is used to investigate the strain localization problem. As discussed in the previous section, the calibrated parameters listed in Table 4.1 are adopted. A series of tests described in Table 4.2 and Table 4.3 are performed to analyze the model performance under drained triaxial loading paths. The effects of boundary conditions (T1-T4) and imperfection positions (T5-T8) are firstly investigated. Then, test T1 is considered as a representative test to discuss the influence of initial void ratio and confining stress.

Test	Imperfection position	Boundary condition
T1	None	①
T2	None	②
T3	None	③
T4	None	④
T5	①	②
T6	②	②
T7	③	②
T8	④	②

Table 4.2 Imperfection positions and boundary conditions of different tests.

4.4.1 Model performance

Figure 4.7 compares the numerical results in terms of deformed configuration and strain field ε_2 for different boundary conditions (T1-T4). By the same token, strain localization with inclined shear band(s) appear(s) in all tests (T1-T4) even though symmetrical boundary conditions (T2 and T3) are adopted. For non-symmetric boundary conditions, the strain localization normally initiates from the non-symmetric boundary point, gradually penetrates the whole specimen to form shear band(s). However, if the boundary conditions do not

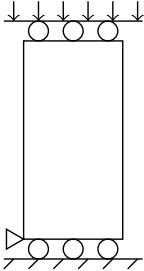
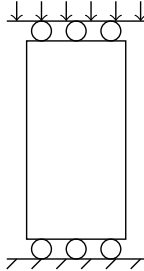
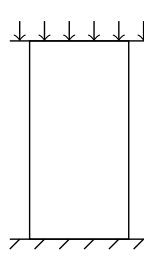
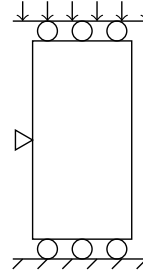
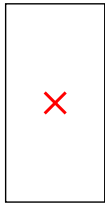
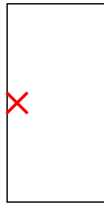
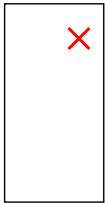
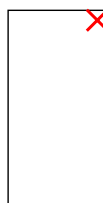
	①	②	③	④
Boundary condition				
Imperfection position				

Table 4.3 Schematic diagram of imperfection positions and boundary conditions given in Table 4.2.

break the symmetry, the elements on the corner firstly reach stress peak and then shear bands develop.

An initial imperfection is introduced in the specimen via some material perturbation in terms of increasing initial void ratio from $e = 0.53$ to $e = 0.54$. The imperfection positions are depicted in Table 4.3. Figure 4.8 compares the failure patterns on deformed configurations in terms ε_2 for distinct imperfection positions. Particularly, even though the material and boundary conditions are homogeneous, the strain localization can be still observed. The deformed configurations referring to distinct imperfection positions are totally different. Generally speaking, shear bands are usually centered on the material point with imperfection. The shape of strain localization depends on the imperfection position: X-shape shear band (T5), half X-shape shear band (T6) or quarter X-shape shear band (T7, T8).

Initiation and development of strain localization are governed by different mechanisms: they do not depend only on boundary conditions and material imperfections, but are also affected by the initial void ratio and confining stress (Desrues and Viggiani, 2004). In this

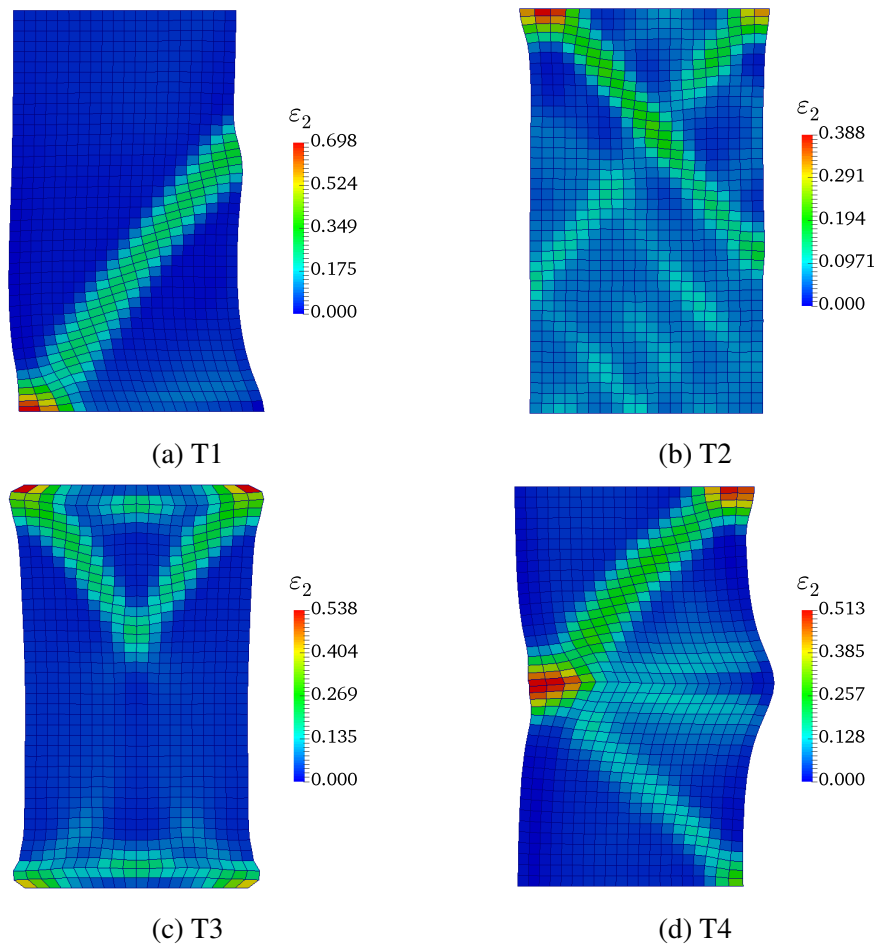


Figure 4.7 Failure patterns on deformed configuration in terms of ε_2 for distinct boundary conditions (T1-T4).

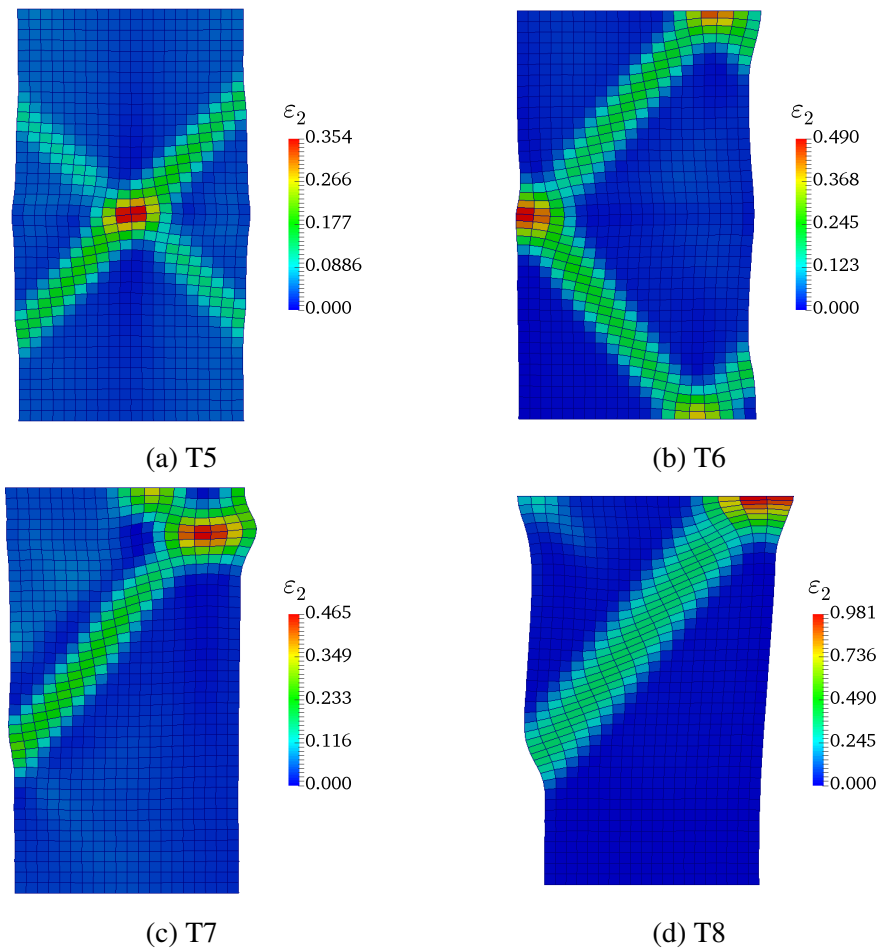


Figure 4.8 Failure patterns on deformed configuration in terms of ε_2 for distinct imperfection positions (T5-T8).

section, the effects of initial void ratio and confining stress are numerically analyzed under plane strain conditions. [Figure 4.9](#) and [Figure 4.10](#) show the mechanical response of the specimen, together with failure patterns at different confining stress for test T1. It is worth noting that the initiation of strain localization corresponds to the stress peak of the mechanical response. The plots clearly demonstrate the influence of confining stress on the mechanical response. The stress peak is reached faster, which means that the strain localization initiates earlier, when the specimen is subjected to lower confining stress compared to those confined at higher stress. It is consistent with the experimental results observed by (Alshibli et al., 2003; Han and Drescher, 1993).

The dense homogeneous specimens for test T1 with initial void ratio spanning from 0.53 to 0.63 are subjected to the triaxial loading path, confined at 200 kPa. [Figure 4.11](#) shows the evolution of deviatoric stress versus overall axial strain. It is observed that the looser the specimen is, the earlier the strain localization initiates, because the stress peak of the looser specimen is reached at a lower axial strain and then the looser specimen becomes heterogeneous.

It is worth noting that the shear band inclination, θ , is in good agreement with the values given by Roscoe's approximation: $\theta = \pi/4 + (\varphi_m + \psi_m)/4$, where φ_m is mobilized friction angle and ψ_m is dilatancy angle. For the 3D-H model, the micro friction angle $\varphi_m = \varphi_g = 25.00^\circ$ and the dilatancy angle $\psi_m = 1.00^\circ$ is measured in [Figure 4.11b](#). Thus, $\theta = 45.00^\circ + (25.00^\circ + 1.00^\circ)/4 = 51.50^\circ$ which is exactly measured in [Figure 4.12a](#).

4.4.2 Phases transition: from homogeneity to inhomogeneity

The nature of the mechanical response of a perfectly homogeneous specimen is investigated in this section. The parameters and initial conditions are identical for all elements in the mesh. [Figure 4.13a](#) and [Figure 4.13b](#) show the mechanical responses and volumetric responses for

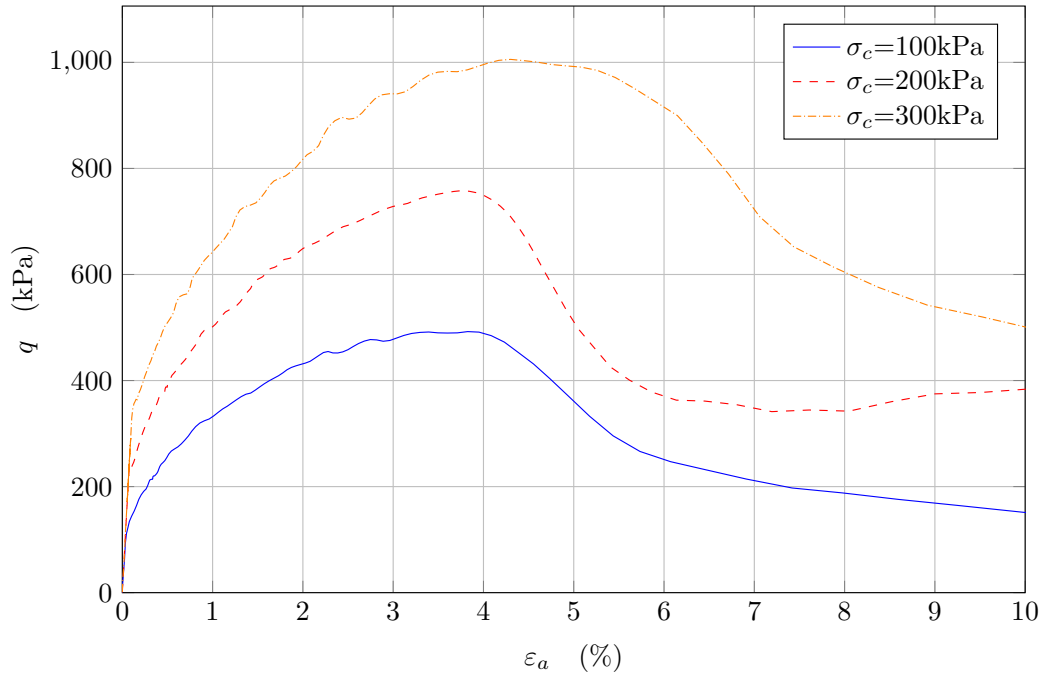


Figure 4.9 Mechanical response with different confining stresses for test T1.

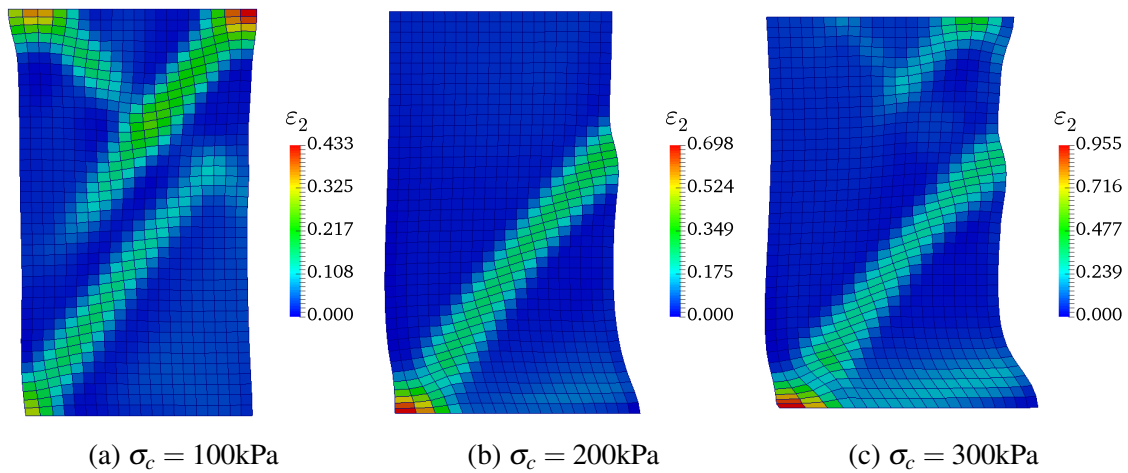
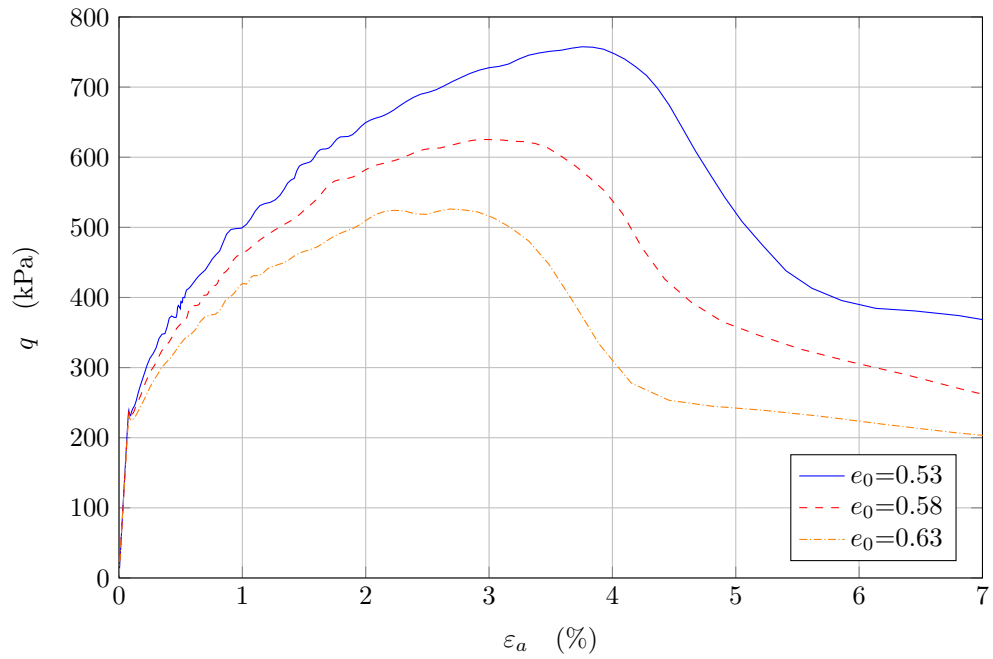
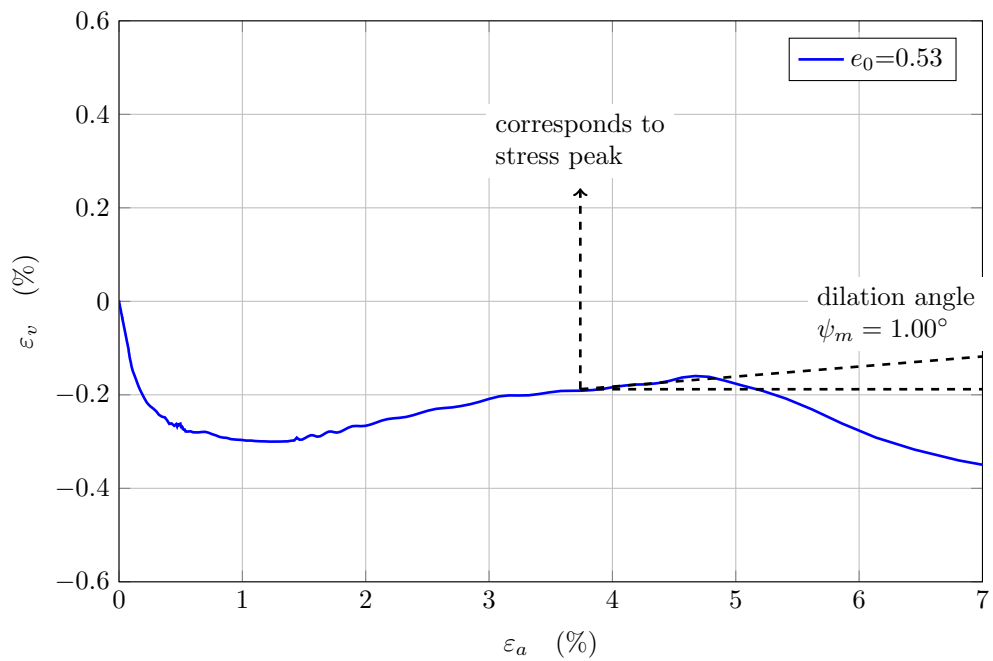


Figure 4.10 Failure patterns on deformed configuration in terms of ε_2 for different confining stresses in test T1.



(a) Mechanical response.



(b) Volumetric responses.

Figure 4.11 Mechanical and volumetric responses with different initial void ratios for test T1.

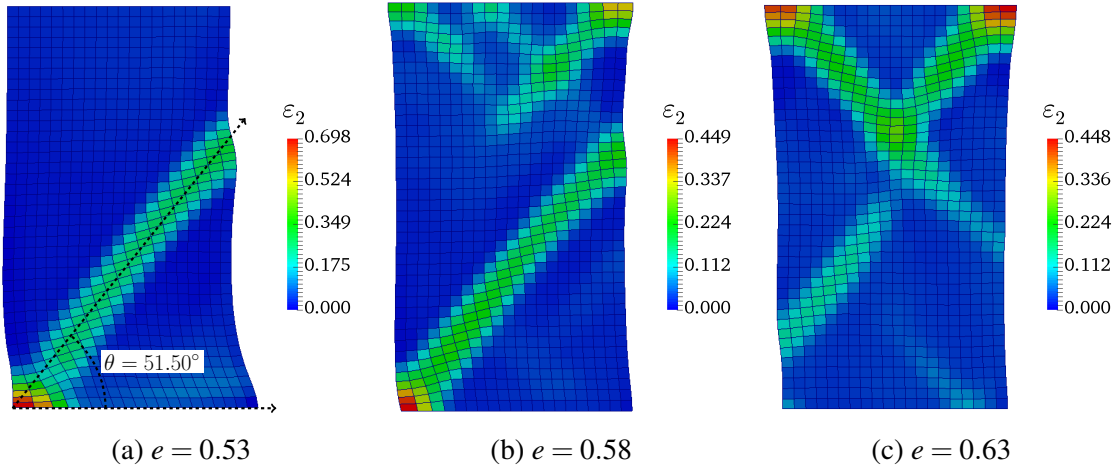
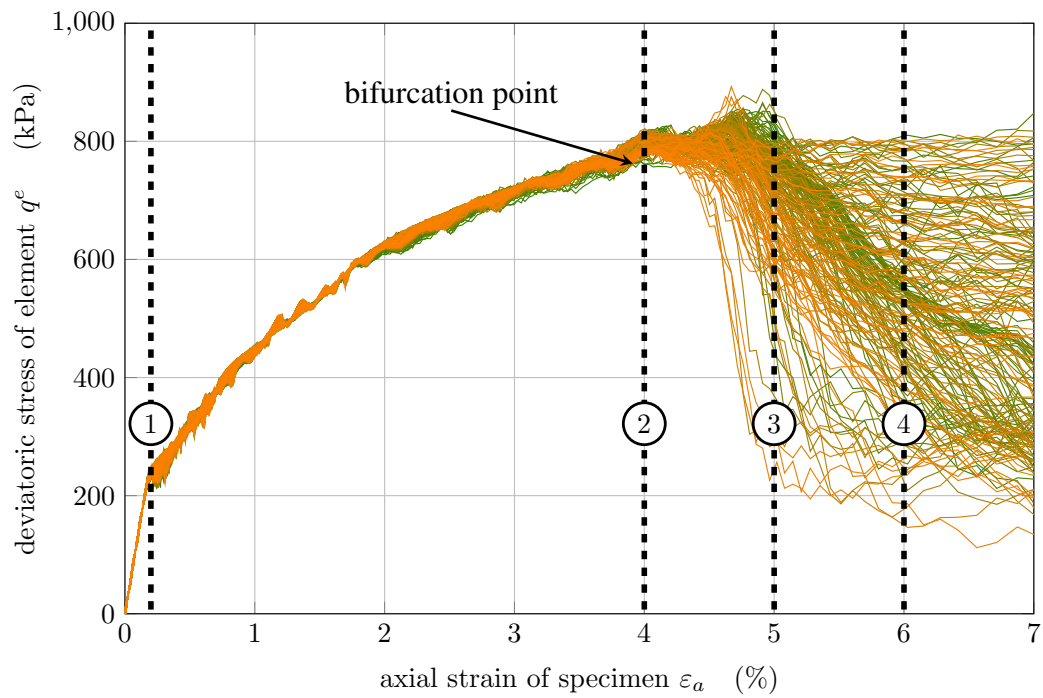


Figure 4.12 Failure patterns on deformed configuration in terms of ε_2 for different initial void ratios in test T1.

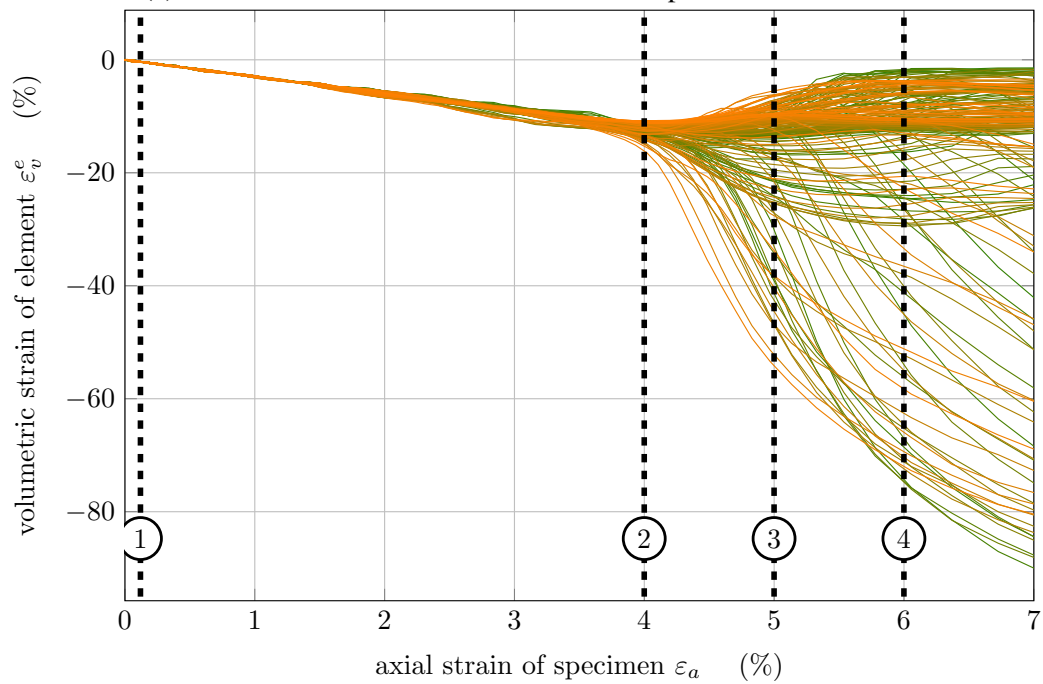
all the elements in the finite element mesh, respectively. The first remark is that from the beginning to the line ①, whatever the mechanical response (stress or volumetric response), the specimen behaves perfectly homogeneously corresponding to the purely elastic regime of the model. The curves approximately coincide from lines ① to ② with slight differences due to possible dynamical effects. All curves bifurcate at a bifurcation point (line ②), which occurs at around 4% of axial strain indicating the loss of uniqueness of solutions of BVPs as a homogeneous problem. This loss of uniqueness corresponds to the violation of Rice's criterion (Darve et al., 2004; Prunier et al., 2009a; Rudnicki and Rice, 1975; Wan et al., 2013).

Figure 4.14 shows the maps of normalized second-order work W_{2n} for the deformed configuration at three different states corresponding to lines ②, ③ and ④ in Figure 4.13. The second-order work for each element can be normalized as follows:

$$W_{2n} = \frac{\delta \vec{\sigma} : \delta \vec{\varepsilon}}{||\delta \vec{\sigma}|| ||\delta \vec{\varepsilon}||} \quad (4.7)$$



(a) Deviatoric stress of each element versus specimen axial strain.



(b) Volumetric strain of each element versus specimen axial strain.

Figure 4.13 Mechanical and volumetric responses for all elements in the mesh.

As shown at state ② in Figure 4.14, the negative values of W_{2n} distribute in the whole specimen, indicating the unstable state of most of the elements, which corresponds to the bifurcation point reported in Figure 4.13. After that, at states ③ and ④, the negative values of W_{2n} concentrate in a narrow zone: a shear band naturally and gradually appears. The material points located inside the shear band remain unstable as negative second-order work values subsist, whereas other points outside the shear band undergo unloading with positive values of second-order work. It is noted that the bottom area of the specimen also reveals negative values at state ② due to the fact that the non-symmetry of the boundary conditions leads to horizontal displacements. However, it gradually disappears when the shear band becomes evident at state ③.

Figure 4.15 correspondingly shows the maps of kinetic energy E_k (J) for the deformed configuration at states ②, ③ and ④. At the bifurcation point ②, elements on the left and bottom boundary firstly experience an increase in kinetic energy due to the deformation of the elements at the bottom left corner. After the shear band appears, the specimen is divided into two parts. The top part evolves in a dynamic regime directed by the external displacement loading applied at the top of the specimen, whereas the bottom part only experiences a material dilatancy. It is consistent with previous work of (Desrues and Viggiani, 2004; Rechenmacher, 2006)

4.4.3 Inside and outside shear band

As illustrated in the previous section, the specimen loses homogeneity when the shear band appears. Thus, the specimen can be considered as constituted with two parts: inside shear band area and outside shear band area. The material behavior should be analyzed separately in these two regions. A shear band or, more generally, a strain localization refers to a special zone where the strain largely concentrates, usually of plastic nature, and develops during

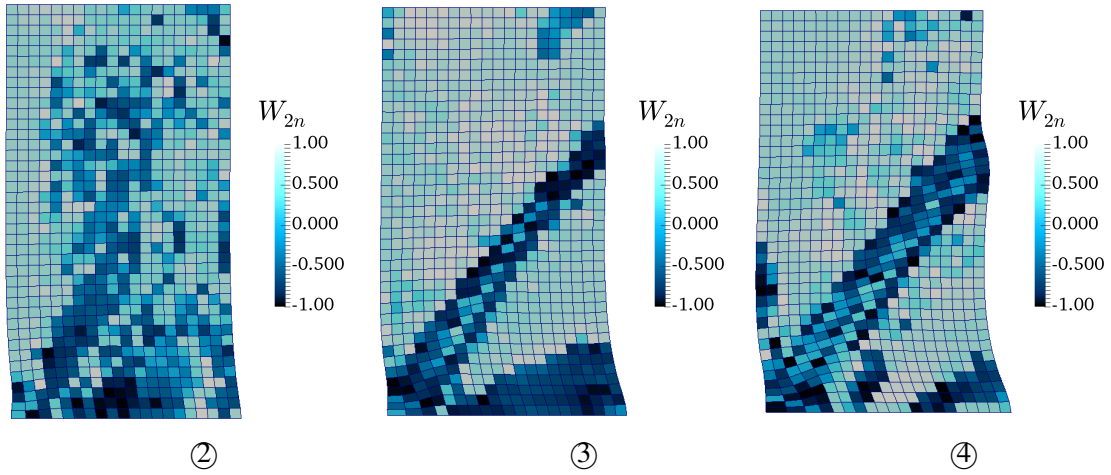


Figure 4.14 The maps of normalized second-order work W_{2n} for the deformed configuration at different states (see [Figure 4.13](#)).

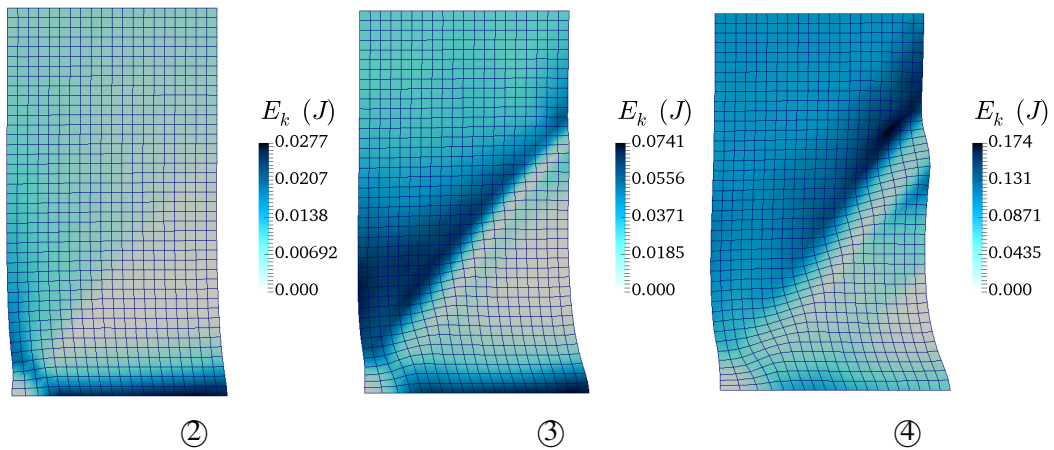


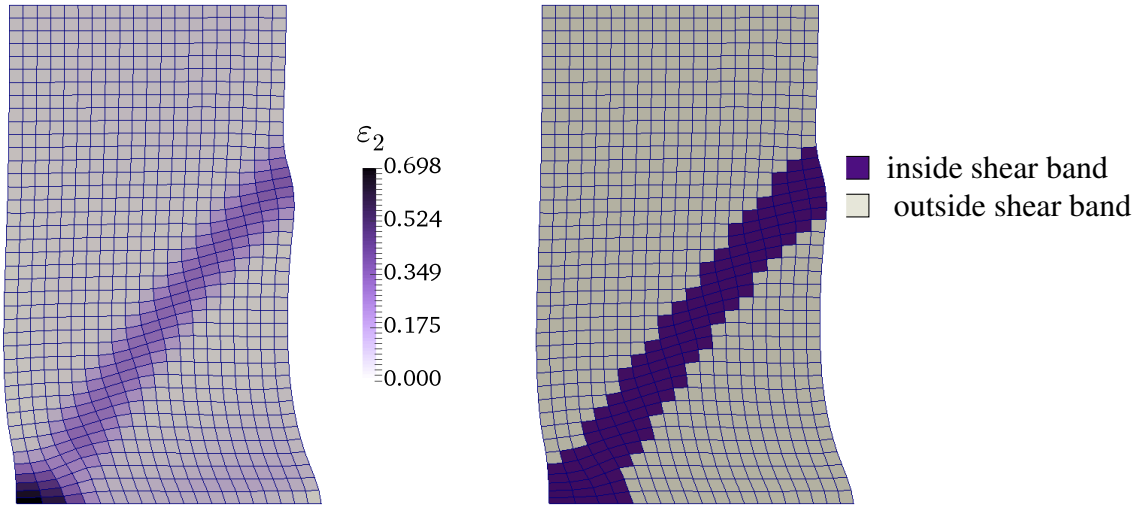
Figure 4.15 The maps of kinetic energy E_k (J) for the deformed configuration at different states corresponding to [Figure 4.13](#).

large deformation of the material. However, there is no quantitative definition of shear band area in the literature. In this section, the element strain (ϵ_2) along direction \vec{x}_2 is used to define the shear band area. In T1 test, for example, the axial strain $\epsilon_a = 6\%$ is selected, located along the descending branch of deviatoric stress curve (Figure 4.13a). The map of ϵ_2 for the deformed configuration of the specimen is shown in Figure 4.16a. As observed in this figure, ϵ_2 experience a localized pattern along a diagonal area crossing the whole specimen to form a shear band, which is a typical localization pattern appearing after stress peak. Thus, the shear band area is defined as in Figure 4.16c, which shows the ascending order evolution of ϵ_2 versus element number. As shown in the figure, most of material points locate below with small ϵ_2 , whereas the remaining material points have large ϵ_2 . In this case, a critical value ϵ_2^c is introduced to determine whether an element is located inside or outside the shear band. Thus, the definition is considered as follows:

$$\begin{cases} \epsilon_2 < \epsilon_2^c & \Rightarrow \text{outside} \\ \epsilon_2 \geq \epsilon_2^c & \Rightarrow \text{inside} \end{cases} \quad (4.8)$$

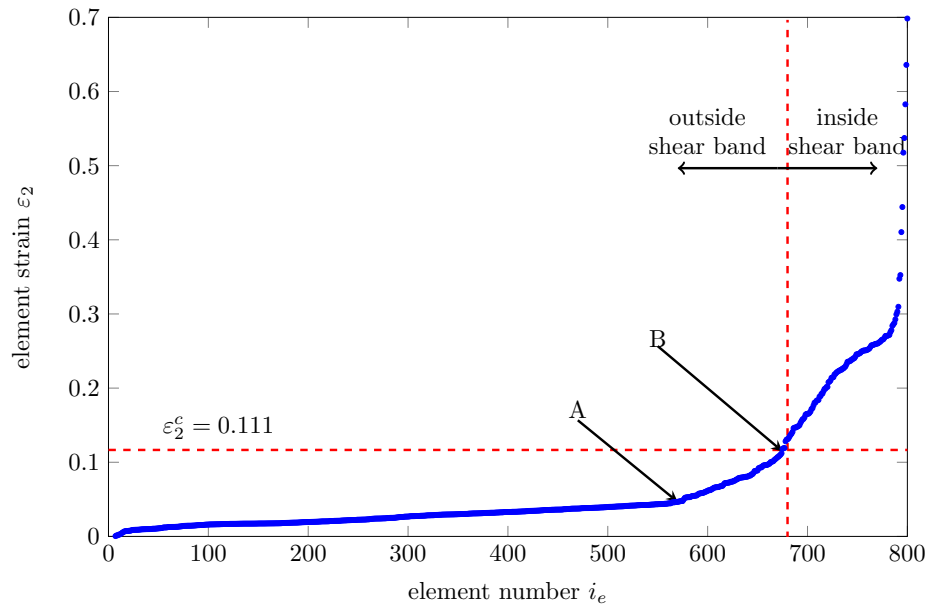
As shown in Figure 4.16c, point A is a transition from linear to nonlinear pattern whereas a linear regime seems to be obtained immediately after point B. Point B is selected, because point B leads a more obvious shear band than Point A. Thus, by adopting $\epsilon_2^c = 0.111$ to test T1, the shear band appears clearly in Figure 4.16b.

Figure 4.17a shows the evolution of volumetric strain with respect to the overall axial strain for specimen T1: inside shear band area, outside shear band area and total area. The three curves are coinciding before $\epsilon_a = 4\%$ due to the fact that the specimen is homogeneous. However, the inside shear band curve and outside shear band curve diverge toward two different states after $\epsilon_a = 4\%$. The outside shear band curve becomes more contractant whereas the inside shear band curve shows dilatancy. Moreover, the global curve does not allow to figure out the strong dilatancy taking place within the shear band. Figure 4.17b



(a) The map of ε_2 for the deformed configuration of T1 at the strain $\varepsilon_a = 6\%$.

(b) Shear band definition by adopting $\varepsilon_2^c = 0.111$.



(c) Ascending order evolution of element strain ε_2 versus element numbers i_e , at the state $\varepsilon_a = 6\%$.

Figure 4.16 Shear band definition.

correspondingly shows the evolution of second-order work against the overall axial strain for specimen T1. The inside shear band second-order work (W_2^{in}) and the outside shear band second-order work (W_2^{out}) are computed as follows:

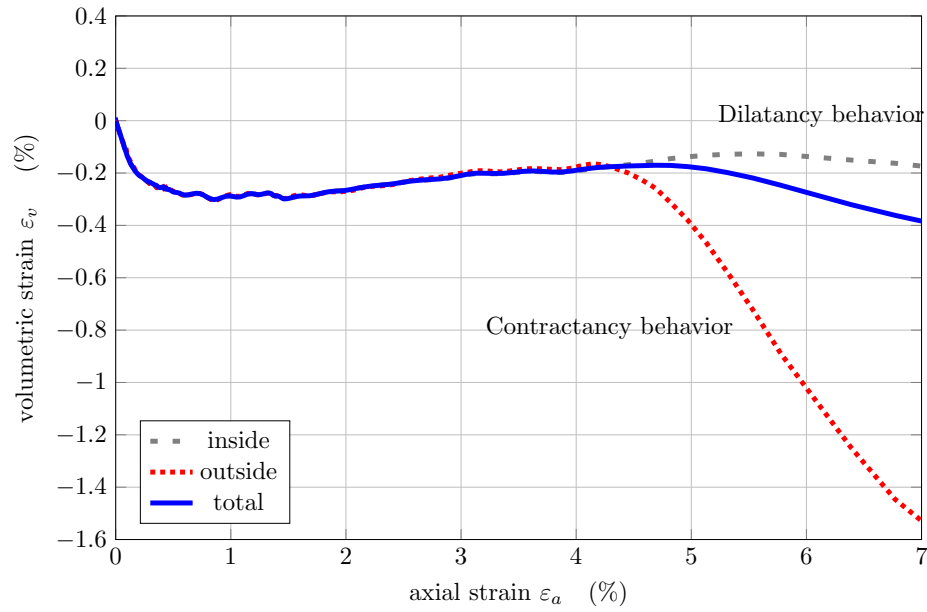
$$\begin{aligned} W_2^{in} &= \sum_{i \in \text{inside}} (\delta \sigma_1^i \delta \epsilon_1^i + \delta \sigma_2^i \delta \epsilon_2^i) \\ W_2^{out} &= \sum_{i \in \text{outside}} (\delta \sigma_1^i \delta \epsilon_1^i + \delta \sigma_2^i \delta \epsilon_2^i) \end{aligned} \quad (4.9)$$

Similar to the volumetric strain curve, the inside shear band second-order work (W_2^{in}) and the outside shear band second-order work (W_2^{out}) diverge when the shear band appears. W_2^{in} shows a significant decreasing dropping to negative values whereas the W_2^{out} stays positive. It should be noted that the number of elements inside the shear band is much less than the number of elements outside the shear band. Finally, this result recovers the fact that the material response and the underpinning mechanisms are totally different inside shear band area and outside shear band area (Desrues et al., 1996; Vardoulakis et al., 1978; Zhu et al., 2016).

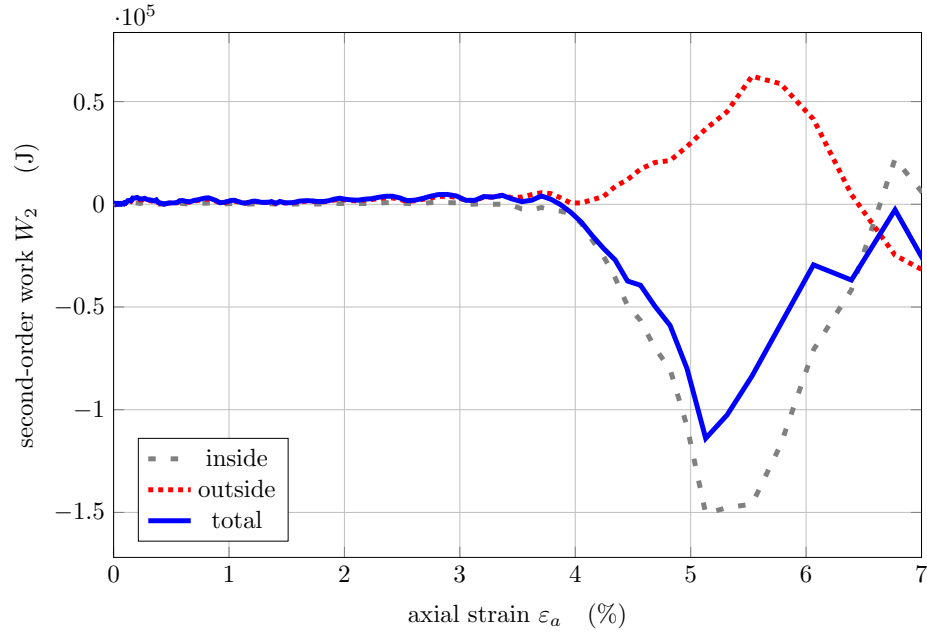
4.5 Directional analysis of second-order work

The aim of this section is to analyze the sign of the second-order work calculated from the finite element model. Considering a conventional drained triaxial test such as T1, some selected stress-strain states are firstly saved along the drained triaxial loading path. Then, strain probes are carried out at these stress-strain states to analyze the model response. Thus, the second-order work can be computed along these directions.

Basically, this method requires the incremental loading is sufficiently small, which is necessary due to the non-linearity of the material response. Thus, incremental strain probes are applied with a uniform magnitude ($\|\delta \vec{\epsilon}\| = 1 \times 10^{-6}$). The angle α_ϵ between $\delta \epsilon_1$ axis and



(a) Evolution of the volumetric strain ε_v (%) against the overall axial strain ε_a (%): inside shear band, outside shear band and total area.



(b) Evolution of the second-order work W_2 (J) against the overall axial strain ε_a (%): inside shear band, outside shear band and total area.

Figure 4.17 Evolution of the volumetric strain ε_v (%) and the second-order work W_2 (J) with respect to the overall axial strain ε_a (%) for test T1.

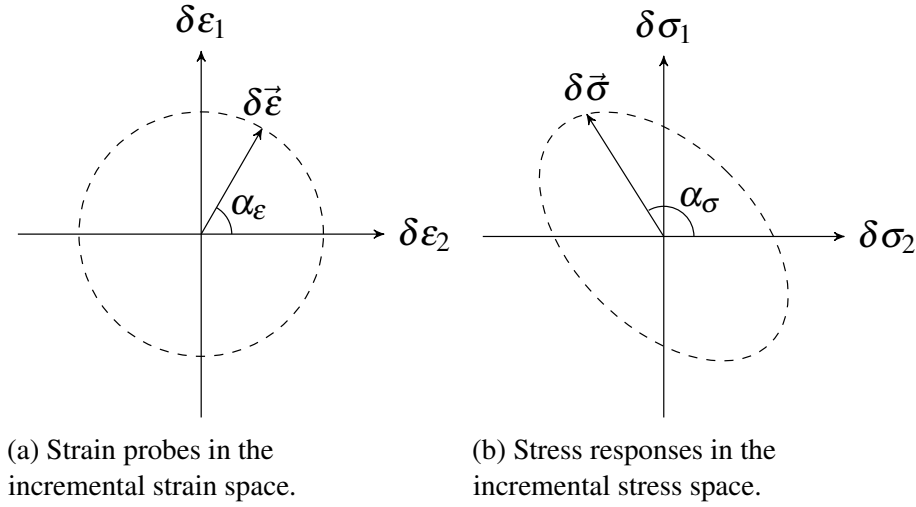


Figure 4.18 Strain probes and stress responses.

$\delta\vec{\epsilon}$ direction is depicted in Figure 4.18a. By varying α_ϵ from 0° to 360° , each strain direction can be considered and the corresponding stress response can be calculated. Similarly, the angle α_σ (see Figure 4.18b) is defined as the angle between $\delta\sigma_1$ axis and $\delta\vec{\sigma}$ direction in the incremental stress space.

Figure 4.19 gives the mechanical and volumetric responses of T1 under triaxial loading conditions with 200 kPa of confining stress. Three states (①, ② and ③) are selected to perform a second-order work directional analysis. State ① corresponds to the end of the isotropically compression stage and state ③ corresponds to the stress peak. During the hardening phase, state ② is selected.

The result of second-order work directional analysis is illustrated in Figure 5.12, which shows the polar diagram of normalized second-order work in the incremental stress space and in the incremental strain space, respectively. The shaded circle represents the vanishing of the normalized second order work. It takes negative values inside the circle. At the beginning (state ①), W_{2n} distributes outside the shaded circle, which means that the sign of W_{2n} along all directions is positive. However, as the axial strain increases, negative values of W_{2n} appear in the second quarter of the incremental strain space, and in the third quarter of the

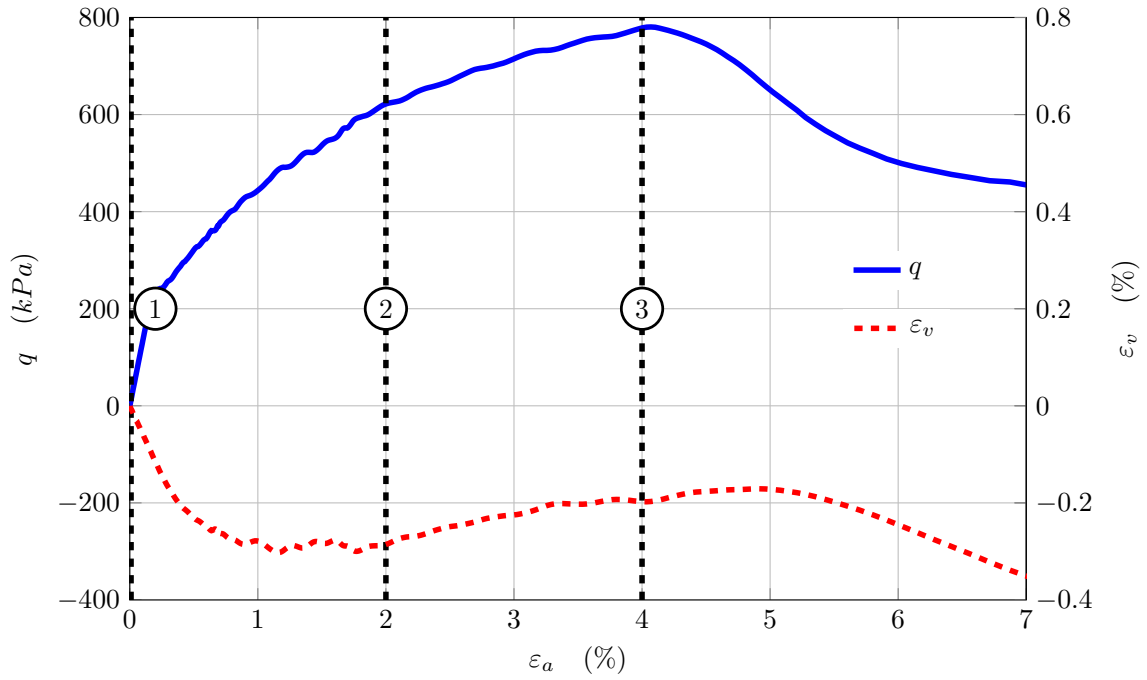
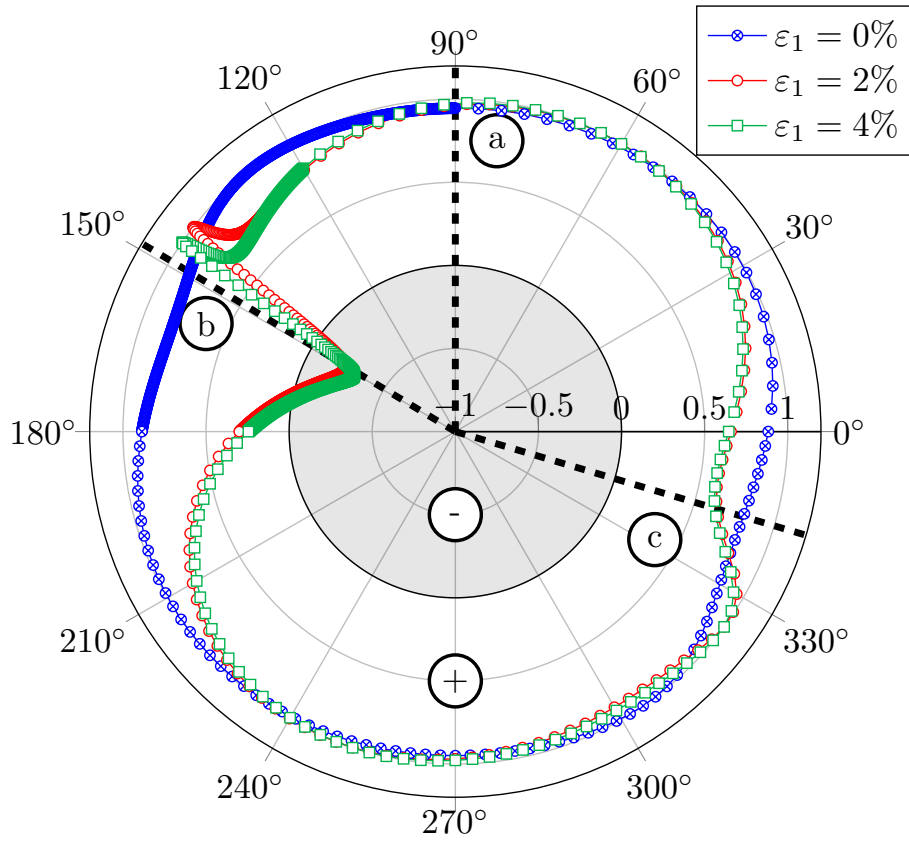


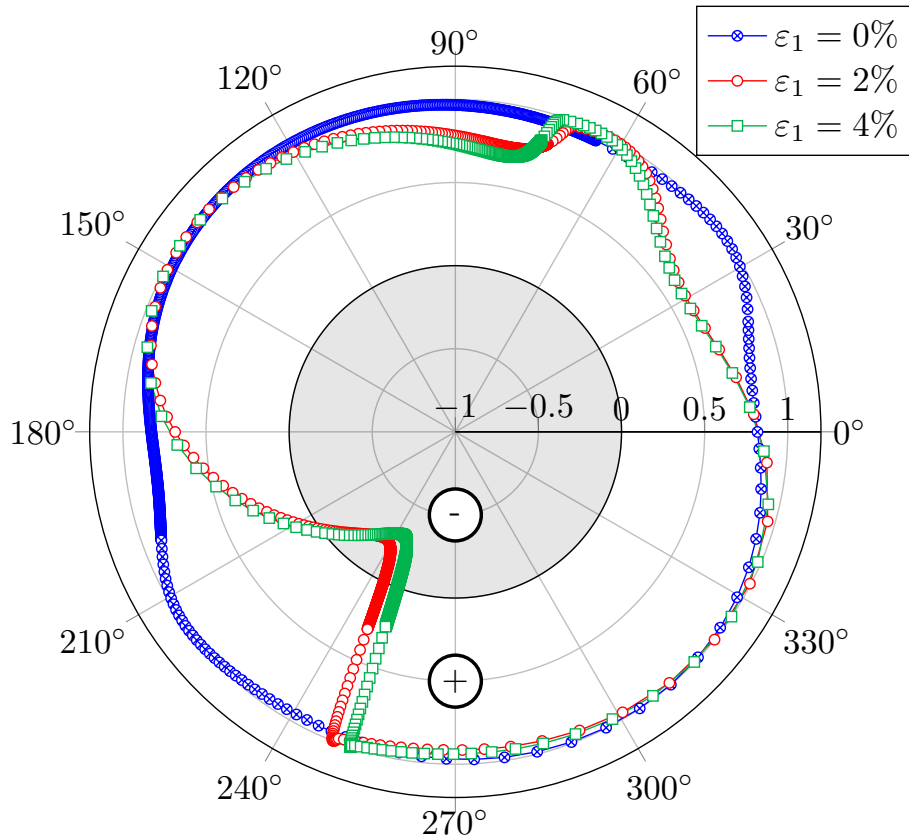
Figure 4.19 Mechanical and volumetric responses of T1 under triaxial loading at 200 kPa of confining stress.

incremental stress space. The cone covering the area of negative value of W_{2n} is the so-called instability cone, indicating that the system is unstable when the loading direction is located inside (Hadda et al., 2013; Nicot et al., 2007b; Prunier et al., 2009b). It is worth noting that the instability cone appears at a stress-strain state, much before the deviatoric stress limit is reached (state ③). It is consistent with the results obtained from other constitutive models and DEM investigations (Nicot et al., 2007b; Sibille et al., 2007).

Taking advantage of the micromechanically-based model, the second-order work can be analyzed not only on the element scale but also on the hexagonal pattern scale (meso-scale). For this purpose, three typical directions (see in Figure 4.20a directions ①, ② and ③) are selected to analyze the angular distribution of second-order work. Direction ② corresponds to strain probes inside the instability cone and directions ① and ③ are located outside the instability cone. For the sake of clarity, the distribution of W_{2n}^{meso} is plotted in 2D rather than



(a) Polar diagram of normalized W_{2n} in incremental strain space.



(b) Polar diagram of normalized W_{2n} in incremental stress space.

Figure 4.20 Polar diagram of normalized W_{2n} in incremental stress space and strain space using strain probes at different loading states with 200 kPa of confining stress.

in 3D. Thus, W_{2n}^{meso} is computed as a function of angle φ by integrating over the two Euler angles (θ and ψ) as follows:

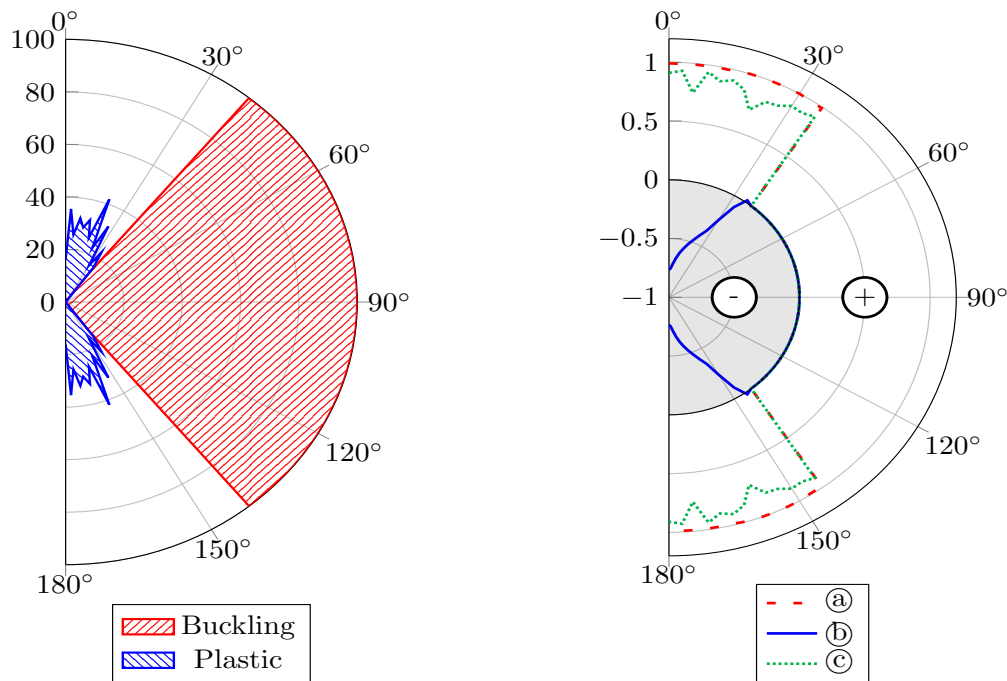
$$W_{2n}^{meso}(\varphi) = \frac{\iint \frac{\delta F \bullet \delta l}{\|\delta F\| \|\delta l\|} d\theta d\psi}{\iint d\theta d\psi} \quad (4.10)$$

Figure 4.21 shows angular distributions of micro variables in terms of φ along the three strain probe directions ① ② and ③ at 2% of axial strain. It should be noted that each direction in Figure 4.21 represents a surface in 3D conditions. Figure 4.21a illustrates the percentage of plastic and buckling meso-structures in this surface. Meso-structure buckling means that at least one contact inside the meso-structure opens, leading to a mechanical softening. Besides, the plastic meso-structure denotes that at least one contact reaches the plastic regime. Figure 4.21b presents the angular distributions of W_{2n}^{meso} over φ under strain probes ①, ② and ③.

As shown in Figure 4.21b, W_{2n}^{meso} inside the buckling zone is merely equal to zero. Obviously, the strain probe ① directs identical and positive value of W_{2n}^{meso} within the plastic zone. The curve ③ shows a slight decreasing compared to ①, but with positive values of W_{2n}^{meso} . When loading direction ② is considered, a large set of material directions are associated with a negative value of W_{2n}^{meso} . This evidences that the meso-structure located in the non-buckling area can be potentially unstable.

4.6 Closing remarks

A 3D multi-scale approach has been developed and further analysis has been carried out to investigate the occurrence of strain localization along drained triaxial loading paths. To avoid too much sophisticated equations requiring a large number of parameters as introduced in most of conventional phenomenological models, a micromechanically-based model, named



(a) Angular distributions of the percentage of plastic and buckling meso-structures along ϕ .

(b) Angular distributions of W_{2n}^{meso} along ϕ by applying the strain probes inside (b) and outside (a, c) the instability cone.

Figure 4.21 Angular distributions of micro variables when the strain probes are applied at 2% of axial strain.

3D-H model, was implemented within a FEM code. The proposed multiscale approach offers a straightforward way to establish the macro-micro relationship wherein the FEM is used to solve BVPs and the 3D-H model is employed as the constitutive relation taking place at Gauss points.

Taking advantage of a micromechanically-based approach, only four parameters are involved. The model parameters were firstly calibrated from comparisons with the experimental data on Ticino sand. Then, drained triaxial tests in plane strain conditions were carried out. A series of aspects were considered, including boundary conditions, material imperfections, initial void ratio and confining stress. A system of shear bands has naturally emerged from a homogeneous specimen, corresponding to a proper bifurcation in the mechanical response of the specimen. A shear band area definition was proposed, and the material response inside and outside the shear band was separately analyzed.

The directional analysis of second-order work was performed. The sign of second-order work is considered as an indicator of material instability. Incremental strain probes were used to detect the vanishing of the second-order work at distinct stress-strain states along a triaxial loading path. An instability cone has been clearly observed in the polar diagram of normalized second-order, indicating the potentiality unstable of the materials. Additionally, loading directions located inside the instability cone were also analyzed on the mesoscopic scale, to highlight the major influence of the anisotropic behavior on this scale.

Chapter 5

Engineering applications based on the second-order work criterion

The multiscale approach is a powerful numerical tool in solving boundary value problems pertaining to strain localization and rich complex material responses of granular media, as fully demonstrated in the previous chapter. Many applications in material sciences and engineering designs and operations can benefit from this advanced approach. In this chapter, more complicated geotechnical engineering problems are investigated using this novel numerical tool. Specifically, a standard problem routinely encountered in geotechnical engineering and/or mining and energy extraction industries - the footing problem- is chosen for such a purpose. In contrast to the previous two chapters, this chapter is devoted to giving a demonstration of the capabilities of the multiscale method in solving the engineering problems, instead of detailed analysis of the problems themselves.

5.1 Second-order work criterion

As reviewed in [section 2.3](#), many examples of granular systems pertaining to instabilities have been reported. Herein, this chapter restricts to divergence instabilities, which means that the system is suddenly no longer able to sustain external forces and experiences large deformation, with strains increasing rapidly over time. This phenomenon is called diffuse failure (Darve et al., 2004), in contrast with localized failure, when the kinematic field presents a chaotic aspect with no visible localization pattern. In fact, this is a proper bifurcation mode, since there is an abrupt transition from a quasi-static regime towards a dynamical regime. Through a proper formalism, this section investigates how the kinetic energy of a system initially in equilibrium can arise when a certain external incremental loading is applied.

For this purpose, consider a material body of volume V_0 and density ρ_0 enclosed by boundary (Γ_0) in a initial configuration C_0 at time t_0 . Following a certain loading history, the body is in a strained configuration C and occupies a volume V of boundary (Γ) , in equilibrium under a prescribed external loading. This loading is defined by specific static or kinematic parameters, referred to as the loading parameters (Klisinski et al., 1992; Nova, 1994; Runesson and Mroz, 1989). The current boundary (Γ) of the material can be resolved into a part (Γ_σ) controlled by static parameters, and a complementary part (Γ_ϵ) controlled by kinematic parameters. \vec{f} denotes the surface density of force applied to Γ_σ and \vec{u} represents the displacement field imposed to each point of Γ_ϵ . It is assumed hereafter that the physico-chemical properties of the constituents of the system being studied are not altered, and that no matter is added to or removed from the system. In addition, only isothermal transformations will be considered, so that the system can only exchange mechanical energy with the exterior.

Adopting a semi-Lagrangian formulation (each material point \vec{x} of the current configuration C corresponds (through bijective mapping) to a material point \vec{X} of the initial configuration C_0), and in absence of body forces, the evolution of each material point of the

system is given by the equation

$$\rho_0 \vec{u}_i - \frac{\partial \Pi_{ij}}{\partial X_j} = 0 \quad (5.1)$$

where $\bar{\bar{\Pi}}$ is the first Piola–Kirchhoff stress tensor. The kinetic energy of the whole system reads:

$$E_c = \frac{1}{2} \int_{V_0} \rho_0 \dot{\vec{u}}^2 dV_0 \quad (5.2)$$

where $\dot{\vec{u}}(\vec{X})$ is the Lagrangian velocity field. It is convenient to express the integrals in [Equation 5.2](#) with respect to the initial configuration. Thus, a double time differentiation of [Equation 5.2](#) yields

$$\ddot{E}_c = \int_{V_0} \rho_0 \ddot{\vec{u}}^2 dV_0 + \int_{V_0} \rho_0 \dot{\vec{u}} \ddot{\vec{u}} dV_0 \quad (5.3)$$

Combining [Equation 5.3](#) with [Equation 5.1](#) gives:

$$\ddot{E}_c = \int_{V_0} \rho_0 \ddot{\vec{u}}^2 dV_0 + \int_{V_0} \dot{u}_i \frac{\partial \dot{\Pi}_{ij}}{\partial X_j} dV_0 \quad (5.4)$$

By virtue of the Green formula, [Equation 5.4](#) can be rewritten as:

$$\ddot{E}_c = \int_{V_0} \rho_0 \ddot{\vec{u}}^2 dV_0 + \int_{\partial V_0} \dot{u}_i \dot{\Pi}_{ij} N_j dS_0 - \int_{\partial V_0} \dot{u}_i \frac{\partial \dot{\Pi}_{ij}}{\partial X_j} dV_0 \quad (5.5)$$

The result is that the second-order time derivative of the kinetic energy is the sum of three terms:

- The first term $I_2 = \int_{V_0} \rho_0 \ddot{\vec{u}}^2 dV_0$ is an inertial term. This is the quadratic average of the acceleration; this term is therefore always positive.
- The second term $\int_{\partial V_0} \dot{u}_i \dot{\Pi}_{ij} N_j dS_0 = \int_{\partial V_0} \dot{u}_i \dot{s}_i dS_0$ is a boundary term involving the loading parameters (the displacements \vec{u} and the current external forces \vec{f} with $d\vec{f} = \vec{s} dS_0$) acting on the boundary of the initial (reference) configuration of the system. It is hereafter called the external second-order work W_2^{ext} .

- The third term explicitly introduces the second-order work, which is expressed following a semi-Lagrangian formalism (Hill, 1958) as $\int_{V_0} \dot{\Pi}_{ij} \frac{\partial \dot{u}_i}{\partial X_j} dV_0 = \int_{V_0} \dot{\Pi}_{ij} \dot{F}_{ij} dV_0$, where $\bar{\bar{F}}$ is the tangent linear transformation. This term is related to the constitutive behavior of the material and is therefore referred to as the internal second-order work W_2^{int} . It should be noted that at any material point of the system, both the stress rate tensor $\dot{\Pi}$ and velocity gradient tensor $\bar{\bar{F}}$ are related by the constitutive relation $\dot{\Pi}_{ij} = L_{ijkl} \dot{F}_{kl}$, where the fourth-order tensor L is the tangent constitutive tensor for rate-independent materials.

It follows that Equation 5.5 can be expressed as:

$$\ddot{E}_c = I_2 + W_2^{ext} - W_2^{int} \quad (5.6)$$

When the system is quasi-static, the inertial term I_2 and the kinetic energy \ddot{E}_c are nil. Thus, Equation 5.6 yields:

$$W_2^{ext} = W_2^{int} \quad (5.7)$$

Equation 5.7 means that the internal second-order work is equal to the external second-order work, when the system is in a quasi-static regime.

5.2 Numerical applications

5.2.1 Laboratory test

Based on the multiscale approach presented in the previous section, a full three-dimensional cylindrical specimen subjected to a drained triaxial loading path is considered as a homoge-

neous BVP. The mesh, element type and boundary conditions are described in [Figure 5.1](#). The cylinder with diameter $D = 2R$ and height $H = 4R$ is discretized into 18580 elements. The bottom surface of the specimen is permanently fixed while the confining stress σ_c is applied to the side surface. The loading program prescribed to the specimen includes three stages: isotropically confining stage under the stress σ_c , strain control stage and stress control stage. The specimen is isotropically compressed at 200kPa during the first stage. Then, a triaxial loading path is imposed by prescribing to the top surface a constant loading speed. Finally, the loading process is switched to a stress control when the axial stress reaches a maximum value. The displacement of the top surface along direction \vec{v}_1 is denoted by d_1 while the external force is denoted by f_1 . During the stress control, f_1 is imposed constant, corresponding to the maximum value of top loading at the end of the strain control stage.

[Figure 5.2](#) shows the mechanical and volumetric responses for the 3D cylinder specimen and the strain fields at the successive states $\epsilon_a = 2.7\%$, 7% , 8% and 9% along a drained triaxial loading path. As shown in [Figure 5.2](#), the deviatoric stress increases up to the peak (the dashed line \otimes when $\epsilon_a = 2.7\%$) and then decreases, with both hardening and softening regimes well reproduced. Meanwhile, the volumetric response shows a contractant behavior before $\epsilon_a = 1\%$ and a dilatant behavior after as expected for dense sand under a drained triaxial loading path. It should be noted that the external stress loading applied to the top surface of the specimen is constant during the stress control stage. The shadow area between the deviatoric stress curve and external stress loading curve is the excess external work, which will be converted into kinetic energy for the system.

As discussed in [section 5.1](#), the external second-order work, based on the prescribed loading condition, reads:

$$W_2^{ext} = \dot{f}_1 \dot{d}_1 \quad (5.8)$$

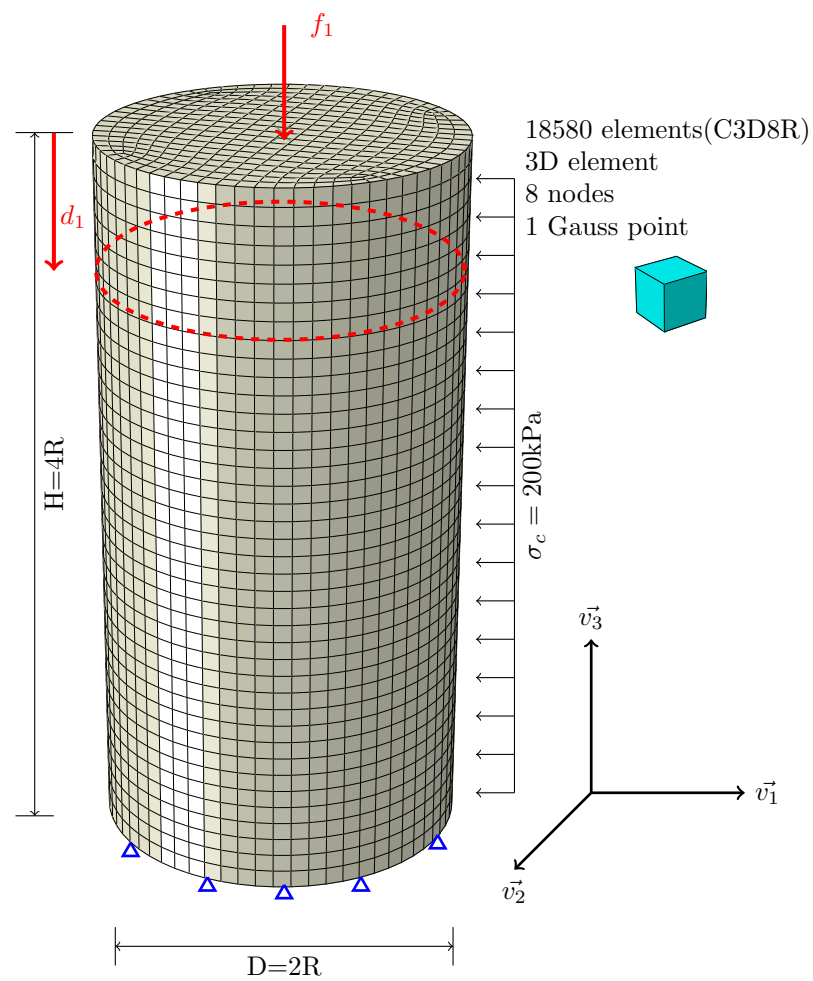


Figure 5.1 Mesh, element type and boundary conditions for the 3D cylinder specimen.

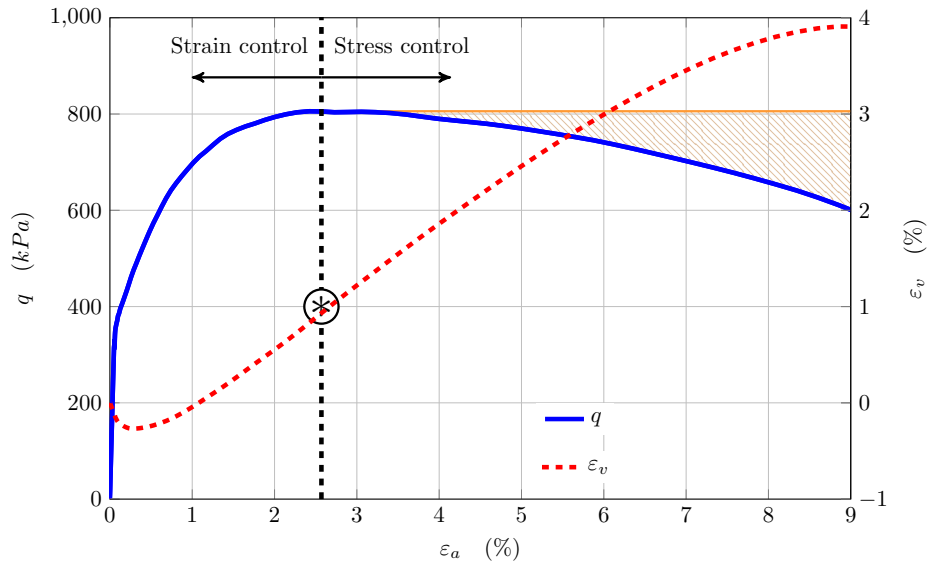


Figure 5.2 Mechanical and volumetric responses for a 3D cylinder specimen and strain fields (ϵ_3) at the selected states $\epsilon_a = 2.7\%$, 7% , 8% and 9% along a drained triaxial loading path under a confining pressure of 200kPa.

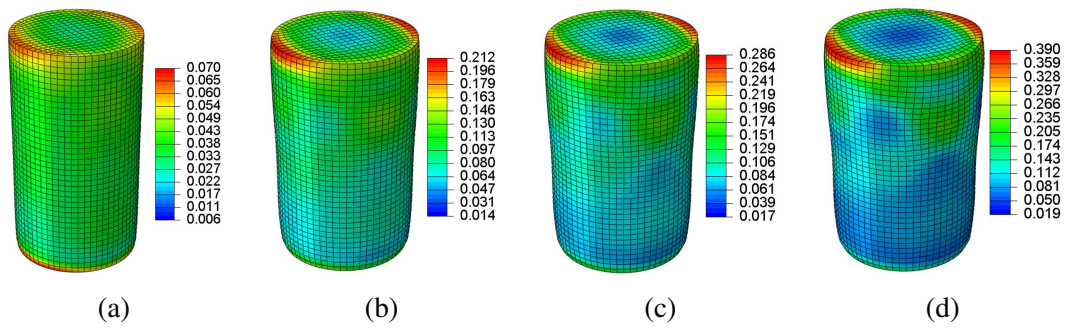


Figure 5.3 1

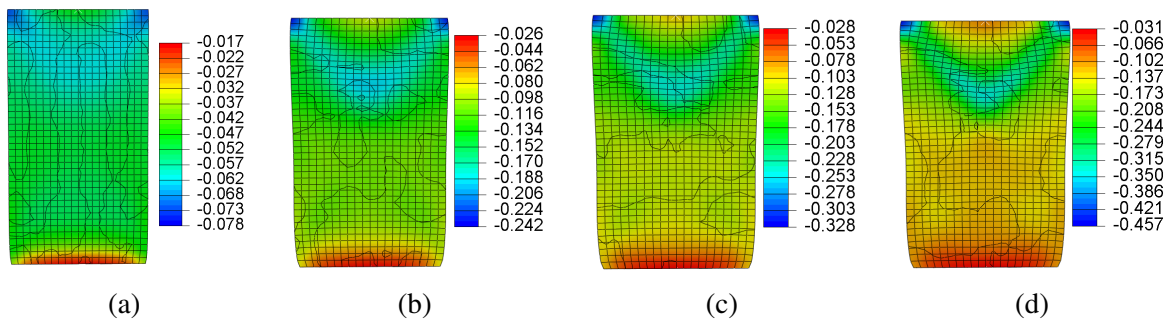


Figure 5.4 1

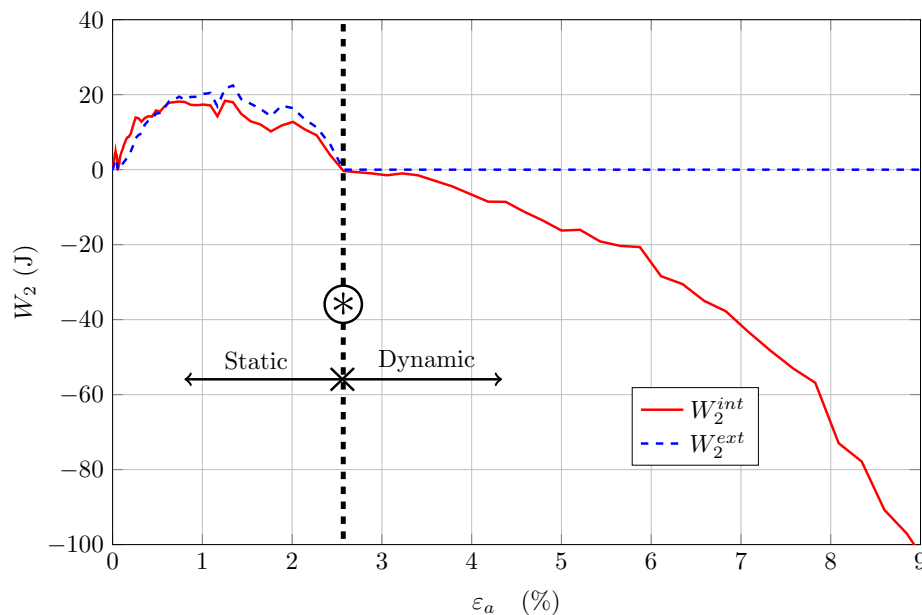


Figure 5.5 Evolution of external and internal second-order works versus axial strain ε_a (%) for a 3D cylinder specimen.

In 3D conditions, the internal second-order work of the specimen is expressed as:

$$W_2^{int} = \sum_{i=1}^n (\sigma_1^i \dot{\varepsilon}_1^i + \sigma_2^i \dot{\varepsilon}_2^i + \sigma_3^i \dot{\varepsilon}_3^i) V_i \quad (5.9)$$

where i is the element indicator, n is the total number of elements, V_i is the volume of the element i .

By using Equation 5.8 and Equation 5.9, the evolution of external and internal second-order works plotted against the axial strain along the drained triaxial loading path is shown in Figure 5.5. It should be noted that the dashed line (*) corresponds to the transition from the strain control mode to the stress control mode. As shown in Equation 5.6, the internal second-order work is equal to the external second-order work during the strain-controlled regime because \dot{E}_c and I_2 is nil. This is verified in Figure 5.5 where the two curves are quite close before the dashed line (*). The very little difference between the two curves is due to the fact that the loading program is not perfectly static and small inertial mechanisms can

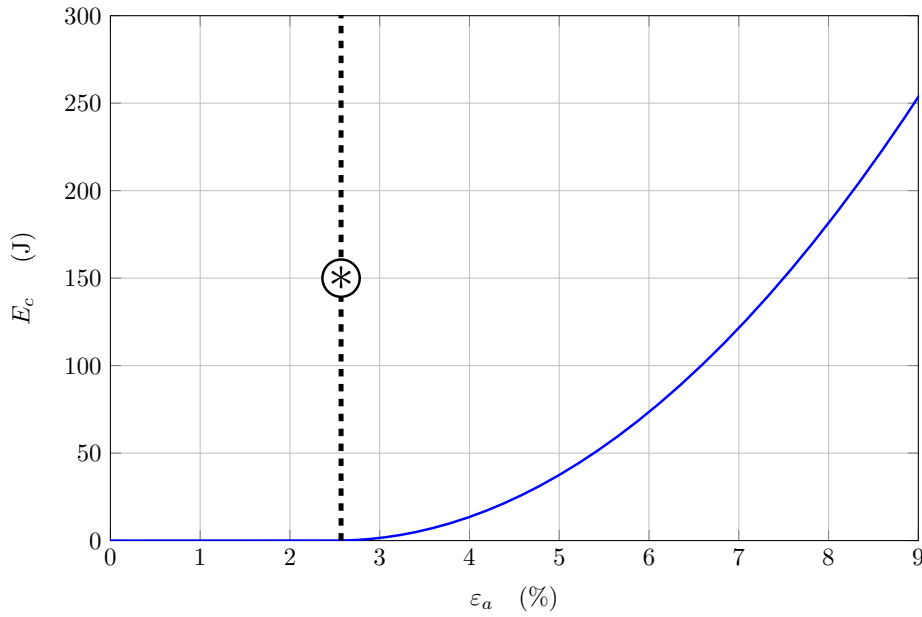


Figure 5.6 Evolution of kinetic energy E_c (J) versus axial strain ε_a (%) for 3D cylinder specimen.

develop. As the deviatoric stress reaches the peak, the internal and external second-order works both vanish. Then, the loading method is switched to a stress control. As can be observed in Figure 5.5, the external second-order work after the dashed line \circledast is zero as $\dot{f}_1 = 0$. However, the internal second-order work is strictly negative after the dashed line \circledast . The difference between internal and external second-order works implies that \ddot{E}_c is positive, which means that the system bifurcates which from a quasi-static regime to a dynamical one. This is verified in Figure 5.6 where the evolution of kinetic energy of the whole system versus the axial strain is shown. The kinetic energy is close to zero during the quasi-static regime, but it abruptly increases once the loading is stress controlled.

5.2.2 Geotechnical engineering problem

The strip footing problem is an example of a non-homogeneous boundary value problem. The multiscale approach presented in chapter 4 is used. The mesh, element type and boundary

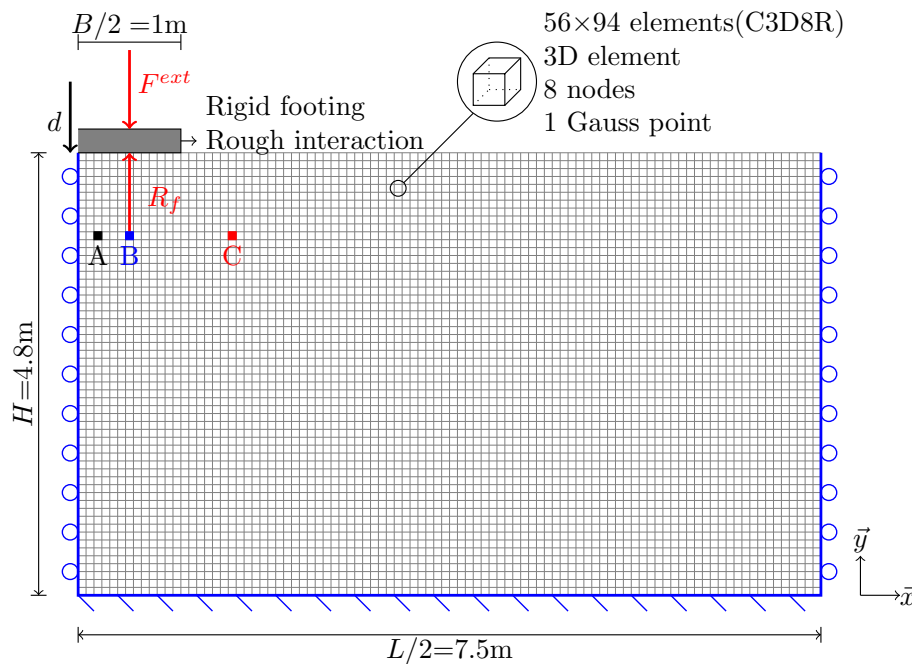


Figure 5.7 Mesh, element type and boundary conditions for the footing problem.

conditions are depicted in Figure 5.7. For the purpose of simplification, only half of the domain is modelled due to the symmetry of the problem. The half domain is discretized into 56×94 elements by using the C3D8R element type. The half-domain width is $L/2 = 7.5\text{m}$ and the depth is $H = 4.8\text{m}$. The half-footing width is $B/2 = 1\text{m}$. The problem is considered as a plane-strain problem. The bottom boundary is blocked in both \vec{x} and \vec{y} directions, whereas the left and right boundaries are only blocked in the \vec{x} direction but are free to move in the \vec{y} direction. The footing is modelled as a rough and rigid strip.

The loading program prescribed to the system consists of three stages. The first stage is the so-called geo-static stage, which means that the gravity is applied to the half-domain while the footing is fixed. After the initial geo-stress field is assigned to the half-domain, a displacement field is obtained. Then, the displacement field is removed after the consolidation stage. Figure 5.8 shows the undeformed mesh with geo-stress distribution at the end of the geo-static stage. As can be seen, the stress increases as the depth increases. The second stage is a velocity control loading stage, the footing goes down with the vertical velocity $v_f = 0.002$

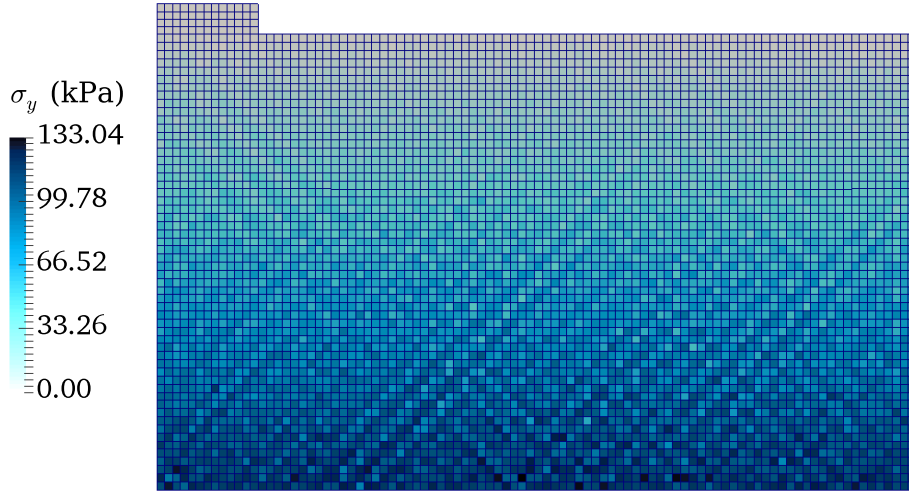


Figure 5.8 Undeformed mesh with geo-stress distribution at the end of geo-static stage.

m/s until the third stage starts. The third stage is a force control loading stage. The reaction force at the end of the second stage R'_f is recorded, and is applied to the footing top surface as an external force F^{ext} during the third stage.

Figure 5.9 shows the evolution of the vertical reaction force R_f versus the footing settlement d (normalized by the footing width B). The dashed line \otimes is the transition from the velocity control stage to the force control stage. Evidently, the curve increases (hardening regime) before the peak and decreases after (softening regime). Figure 5.11 depicts the deformed meshes with distribution of plastic strain ϵ_p at $d/B = 1\%, 2\%, 4\%$ and 8% , respectively. The plastic strain field (ϵ_p) initiates on the right-bottom corner of the footing and spreads to deeper zones. When $d/B = 4\%$ (the peak state in Figure 5.9), the strain progressively localizes, but no clearly shear band can be observed. As R_f goes through the peak ($d/B = 8\%$), the reaction force applied from the soil to the footing cannot accommodate the external loading due to the material softening. A triangular-shaped clod appears under the footing and an inclined shear band beneath the clod develops. Furthermore, the triangular-shaped clod can be clearly observed from the displacement field plotted in Figure 5.10.

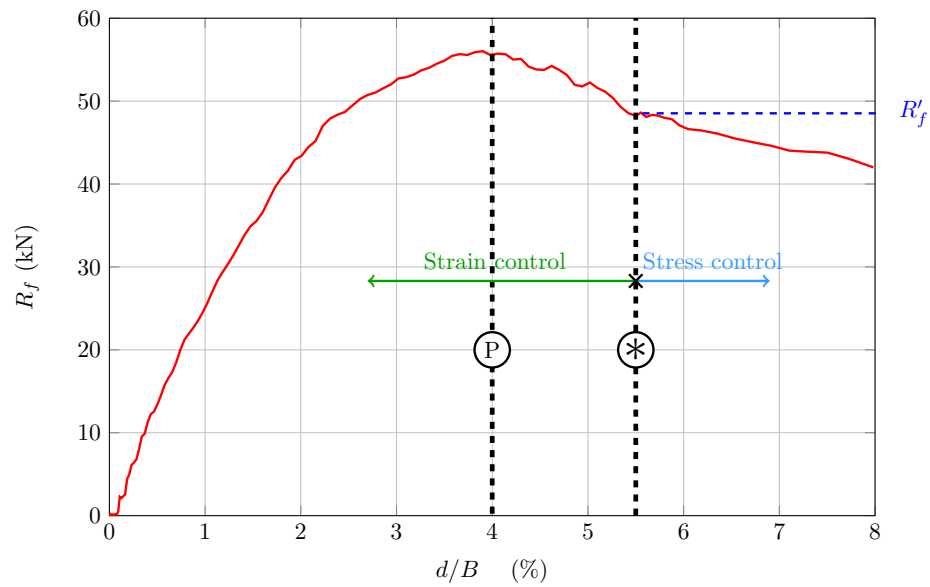


Figure 5.9 Evolution of the vertical reaction force R_f (kN) versus the footing settlement normalized by the footing width d/B (%).

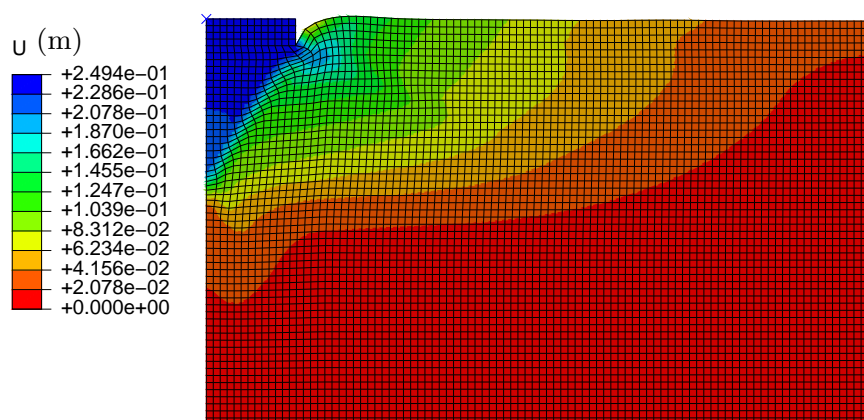


Figure 5.10 Displacement field $|\vec{u}|$ at the state $d/B = 8\%$.

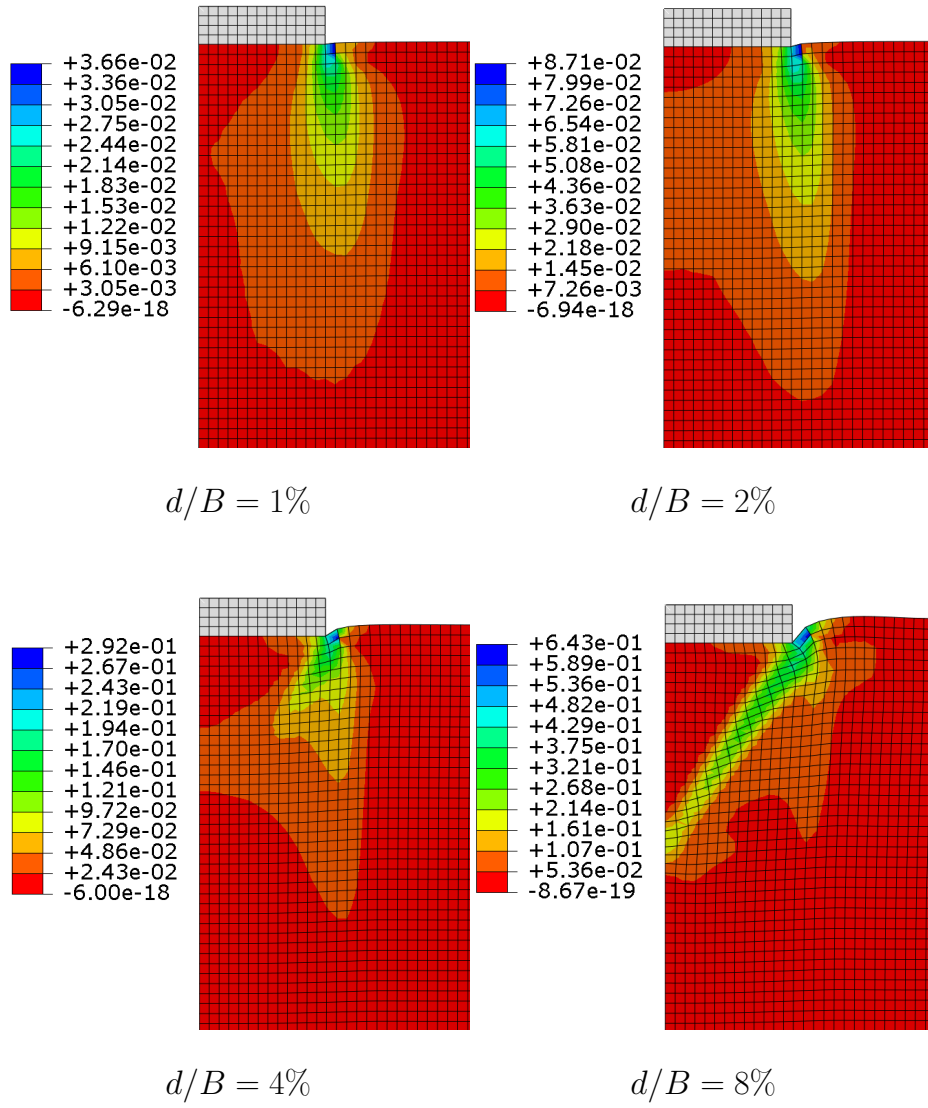


Figure 5.11 Deformed meshes with distribution of plastic strain (ϵ_p) at different states: $d/B = 1\%$, 2% , 4% and 8% .

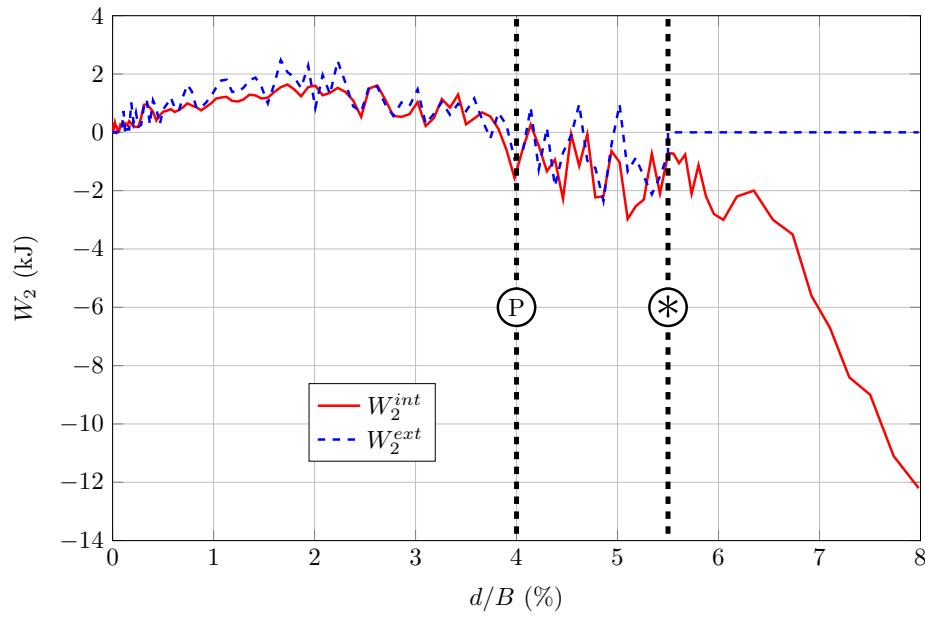


Figure 5.12 Evolution of internal and external second-order works versus the footing settlement normalized by the footing width d/B (%).

According to the prescribed loading program, the external second-order work is computed from Equation 5.5 as:

$$W_2^{ext} = d\dot{R}_f \quad (5.10)$$

As a non-homogeneous boundary value problem, the material points of the discretized system behave differently, leading to a spatial distribution of both stress and strain. The internal second-order work of the system is expressed as:

$$W_2^{int} = \sum_{i=1}^n (\dot{\sigma}_x^i \dot{\epsilon}_x^i + \dot{\sigma}_y^i \dot{\epsilon}_y^i) V_i \quad (5.11)$$

where i is the element number, n is the total number of elements, V_i is the volume of the element i .

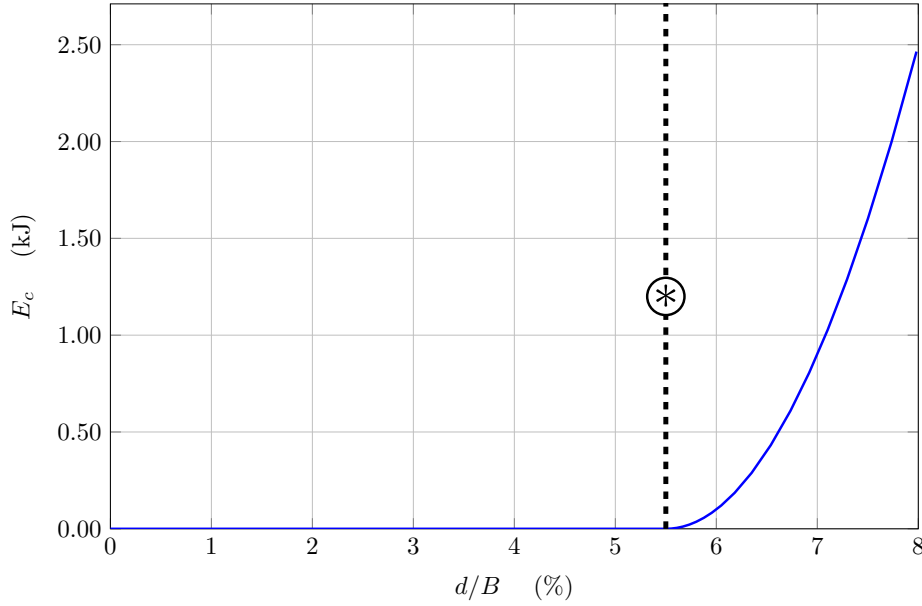


Figure 5.13 Evolution of kinetic energy E_c (kJ) of the whole system versus the footing settlement normalized by the footing width d/B (%).

Figure 5.12 gives the evolution of internal and external second-order works plotted against the normalized footing settlement. It is remarkable that the internal and external second-order works approximately coincide during the velocity-controlled loading regime ($0 < d/B < 5.5\%$). Since the velocity applied to the footing is small enough, the system can be considered as quasi-static. According to Equation 5.6, the difference between internal and external second-order works is related to the inertial term I_2 and to the second-order time derivative of the kinetic energy \ddot{E}_c , both negligible. It is worth noting that both internal and external second-order works are positive during the first loading stage. The vanishing of the second-order work corresponds the stress peak in Figure 5.9, around $d/B = 4\%$. As seen in Figure 5.12, the two second-order work curves become more and more divergent after $d/B = 4\%$, indicating that the system is no longer stable. Especially, after the transition from velocity control to force control (dash line \circledast), the internal second-order work is strictly negative whereas the external second-order work equals zero as $R_f = R'_f = \text{constant}$. The

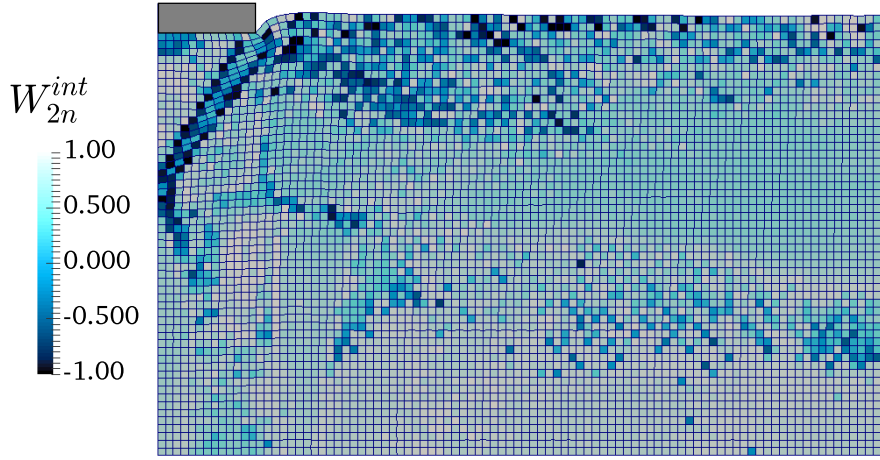


Figure 5.14 Deformed meshes with normalized internal second-order work distribution at the state $d/B = 8\%$.

difference between internal and external second-order works results in an abrupt increase in kinetic energy, which is evidently observed in [Figure 5.13](#).

For each element, the internal second-order work can be normalized as follows:

$$W_{2n}^{int} = \frac{\dot{\sigma}_x \dot{\epsilon}_x + \dot{\sigma}_y \dot{\epsilon}_y}{\sqrt{(\dot{\sigma}_x^2 + \dot{\sigma}_y^2)(\dot{\epsilon}_x^2 + \dot{\epsilon}_y^2)}} \quad (5.12)$$

[Figure 5.14](#) shows the deformed mesh with normalized internal second-order work distribution at the state $d/B = 8\%$. Negative values of W_{2n}^{int} mainly concentrate within two areas: A shear band area below the triangular-shaped clod and an arc-shaped area in the shallow soil. The former is due to the occurrence of a strain localization. The mechanical response of Gauss points inside this area follows a softening regime, which means that the term $\dot{\sigma}_x \dot{\epsilon}_x$ is negative and can vanish W_{2n}^{int} (see [Figure 5.15](#)). It should be noted that significant negative values of internal second-order works concentrate at the boundaries of shear bands. The latter is formed because of the dilatancy behavior of the material, resulting in $\dot{\sigma}_y \dot{\epsilon}_y$ to be negative.

Featuring a major advantage, the presented multiscale approach provides a straightforward way to perform both micro and meso scale analysis. The key microscopic behaviors hidden

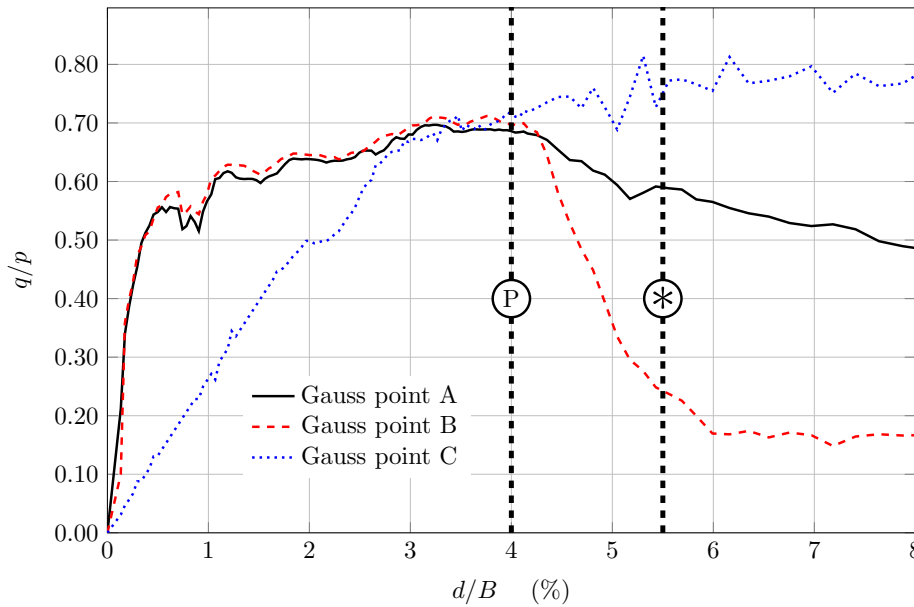


Figure 5.15 Evolution of deviatoric stress ratio versus normalized footing settlement corresponding to selected Gauss points seen in Figure 5.7.

behind the macroscopic scale are helpful to understand and interpret the micro-mechanisms governing the overall response. For the purpose of demonstration, several representative Gauss points are selected in Figure 5.7. They are located at the same depth to make sure that their initial states are same. Gauss point A locates inside the triangular-shaped clod, Gauss point B locates inside the shear band and Gauss point C locates outside the shear band. Figure 5.15 presents the evolution of deviatoric stress ratios q/p of these three Gauss points against the normalized footing settlement d/B . The three curves show increasing trend before $d/B = 4\%$, but the curves for Gauss points A and B decrease after that. The curves for Gauss points A and B cross at the same intersection point and bifurcate to different branches. It is remarkable that the intersection point locates on the dashed line \textcircled{P} ($d/B = 4\%$, corresponding to the stress peak in Figure 5.9). The curves of Gauss point A and B practically coincide before dashed line P, but they behave differently after that. Indeed, Gauss point B locates inside the shear band while Gauss point A does not. Moreover, this is the reason why the internal second-order work inside shear band is negative while it is positive outside

shear band (see [Figure 5.14](#)). Finally, these results confirm that the material response and the underpinning mechanisms are totally different inside shear band area and outside shear band area (Desrues et al., 1996; Vardoulakis, 1996; Vardoulakis et al., 1978; Zhu et al., 2016).

5.3 Closing remarks

This chapter has presented a novel effective multiscale approach to solve geotechnical boundary value problems. This multiscale approach is implemented within a FEM software to tackle macroscopic BVPs from a micromechanically-based model to build the stress-strain relations at the Gauss points of the FEM mesh.

In order to illustrate the capability of this approach, two examples are considered with homogeneous conditions and non-homogeneous conditions. The first example presents a cylindrical specimen subjected to a drained triaxial loading path under an isotropically confining stress whereas the second example illustrates a geotechnical boundary value issue. From a numerical point of view, both analyses verify that when no effective failure occurs, both internal and external second-order works coincide. This is a great advantage since the external second-order can be obtained in a straightforward manner from the boundary variables without requiring only internal information (internal stress or strain fields).

Furthermore, this multiscale approach utilizes an explicit-dynamic integral method so that the post-peak failure can be investigated. Thus, by switching the loading method from a strain control to a stress control at the limit state, the collapse of the system can be reflected in an abrupt increase with system kinetic energy, stemming from the difference between both internal and external second-order works.

Finally, taking advantage of the multiscale approach, the analysis can also be carried out on the REV scale. The vanishing of the second-order work, as a convenient indicator

of material instability, reveals a close correlation with the occurrence of strain localization. For the sake of illustration, three Gauss points were selected to examine local responses, illustrating the difference in the mechanical responses inside and outside shear band areas.

Chapter 6

Conclusions and recommendations

A great variety of numerical simulations were carried out in this research work as a means to delve further into the understanding and modeling the complex behavior of granular materials. A novel constitutive model was firstly formulated to describe the complex behavior of granular materials. This model is then implemented within a FEM code by using a multiscale approach in order to capture pertinent failure patterns and instability mode. After that, various boundary value problems ranging from laboratory tests to geotechnical engineering problems are considered. This last chapter concludes this rather extensive research work. The most salient findings from each Chapter are recalled and, finally, a general conclusion is elaborated. Despite great efforts have been made to explore recent theoretical, experimental and numerical studies of granular materials, this dissertation is far from being complete as many other aspects of the problem can still be explored. As such, recommendations for future research are presented.

6.1 Conclusions

The content of this thesis is systematically divided into three parts which are complementary to each other. With an appreciation of the microscopic origins and mechanisms that govern the macroscopic responses of the material, the first part is solely devoted to the development of a micromechanically-based constitutive model, which will be used in the subsequent simulations. In the second part, the microscopic and the macroscopic characterizations of granular media behavior are bridged under a unique framework called multiscale modeling. Various boundary value problems are examined using this approach, where macro-micro responses and occurrence of strain localization are carefully explored. In the last part, the method is further applied to solve practical geotechnical engineering problems.

6.1.1 Constitutive modeling of granular materials by considering microstructure

Granular materials are multiscale in nature. They are often modeled as a continuum, for which many advanced constitutive models have been developed. Having gained certain successes in reproducing some salient behaviors of granular media, these continuum models have various limitations as they overlook the discrete nature of the materials. For example, the fabric evolution and the particle rearrangement are two characteristics associated with granular media which are absent in most existing continuum constitutive models. These less-noticed characteristics, which have been evidenced to play a role in determining the macroscopic responses of a granular material, are encoded at the microscopic level of the material. Therefore, a multiscale investigation is indispensable to improve our understanding of the complex granular media behavior, which has been the main focus of this thesis.

In the first part, the micro-directional model and the H-directional model are firstly reviewed. Based on the homogenization scheme, the H-directional model is extended to 3D conditions by replacing the 2D hexagonal pattern with a 3D meso-structure. For this purpose, a decomposition and superimposition approach is introduced to analyze the local behavior of the meso-structure. The 3D-H model only introduces four parameters, wherein k_n , k_t and φ_g stem from the elastic-perfect plastic inter-particle contact law. The forth one (the opening angle α_0) is a key microscopic geometrical parameter which can be estimated from the initial void ratio. It is noteworthy that the granular assembly rearrangement can be reflected by the evolution of the opening angle α_0 .

By comparing with experimental results on Ticino sands, the calibration of the model is carried out and the predictive capabilities are examined along drained triaxial compression loading paths. The results obtained are both qualitatively and quantitatively satisfying. The hardening and softening regimes are well reproduced in terms of the stress-strain response. Meanwhile, the dilatant and contractant regimes are also well described with the volumetric strain curve. By adopting the calibrated parameters, two sets of numerical tests are run, including different confining stresses and initial void ratios. One of the most significant findings emerging from this study is that the critical state can be approximately described from void ratio evolution without involving any CSL formulations and parameters. The model mechanism is also analyzed from a microscopic point of view. The angular distributions of micro variables are plotted at different strain states under the drained triaxial loading paths. The conclusions of this micro-structural analysis are: (1) the force fabric within the material shows an anisotropy distribution after the deviatoric stress applied to the specimen; (2) the local stress $\tilde{\sigma}_n$ plays a major role along the axial compression direction ($\varphi = 0$ or 180°); (3) the opening angle α is a key geometrical parameter, which reveals the rearrangement of the specimen.

6.1.2 Finite element implementation procedure

For decades, FEM has been widely applied in modeling BVPs of granular media due to its efficiency and robustness, wherein the material is treated as a continuum. These considerations motivate the development of a multiscale modeling approach in this thesis which bypasses the phenomenological constitutive model by embedding a micromechanically-based model at the FEM Gauss points and retains the FEM computational efficiency in solving large scale BVPs. The proposed multiscale approach offers a straightforward way to establish the macro-micro relationship wherein the FEM is used to solve BVPs and the 3D-H model is employed as the constitutive relation taking place at Gauss points. By implementing the 3D-H model within a FEM code (ABAQUS), multiple (micro, meso and macro) scales are bridged in a unique framework. Many macroscopic observations such as strain localization could be tracked and explained coherently by their micro and mesoscopic behaviors.

Taking advantage of a micromechanically-based approach, only four parameters are involved. The model parameters were firstly calibrated from comparisons with the experimental data on Ticino sand. Then, tests along drained biaxial loading paths were carried out to investigate the occurrence of strain localization. A series of aspects were considered, including boundary conditions, material imperfections, initial void ratio and confining stress. A system of shear bands has naturally emerged from a homogeneous specimen, corresponding to a proper bifurcation in the mechanical response of the specimen. A shear band area definition was proposed, and the material response inside and outside the shear band was separately analyzed.

The directional analysis of the second-order work was performed. The sign of second-order work is considered as an indicator of material instability. Incremental strain probes were used to detect the vanishing of the second-order work at distinct stress-strain states along a biaxial loading path. An instability cone has been clearly observed in the polar

diagram of normalized second-order in both incremental strain and incremental stress spaces. Additionally, loading directions located inside the instability cone were also analyzed on the hexagon scale, to highlight the major influence of the anisotropic behavior emerging on this scale.

6.1.3 The occurrence of strain localization

The occurrence of strain localization is regarded as the precursor of many catastrophic failure of geomaterials and pertaining geostuctures. The multiscale approach has been proven to be an ideal tool which is compared with the experimental results by providing an integrated multiscale perspective. In addition, complex granular media characteristics such as local dilatancy and grain rearrangement can be naturally captured and conveniently incorporated by introducing a meso-structure. The most important findings are as follows:

- It is shown from the study that strain localization can occur in a uniform sample with symmetric smooth boundary conditions without introducing any artificial imperfection due to the numerical perturbation, which serves as a mechanism of symmetry breaker. Undoubtedly, the imperfection point or non-symmetric boundary point can initiate the strain localization, from which the shear band develops. At the occurrence of strain localization, the perfectly homogeneous specimen bifurcates at a bifurcation point, which occurs at around the stress limit, indicating the loss of uniqueness of the quasi-static solution of the BVPs. This loss of uniqueness corresponds to the violation of Rice's criterion (Rudnicki and Rice, 1975) at some points, illustrating the phases transition from homogeneity to inhomogeneity.
- When the specimen transforms from homogeneous conditions to non-homogeneous conditions along the biaxial loading path, significantly negative values of internal

second-order work distribute inside the shear band. It is illustrated in this study that the internal second-order work is a convenient indicator for analyzing material instabilities.

- The extra boundary constraint influences the global behaviors significantly. Noticeable resultant shear stress develops as the shear band initiates. In contrast to the single shear band pattern in the symmetric boundary conditions, X-shape shear bands are observed under the non-symmetric boundary conditions. In addition, the confining stress applied to the specimen and the initial density also influence the global behaviors and the shear band formation.
- A cross-scale is achieved to fully unleash the predictive power of this approach. Simulations of monotonic biaxial compression test and the axisymmetric triaxial test on sands highlight the advantages of the multiscale approach. When the occurrence of strain localization is observed in the monotonic biaxial compression test, local analyses show that the local Gauss points outside the shear band may undergo unloading and develop relatively small deformations, whereas those inside the shear band may experience substantial shear deformation and reach the critical state. It is also found that a small proportion of Gauss points fail along the edges of the shear band after very large deformation with unconfined dilation. The contact force at the Gauss points inside the shear band show more contact forces along the loading direction which is aligned with the major compression direction. These results are qualitatively consistent with observations from laboratory tests and other numerical simulations.

6.1.4 Simulation of geotechnical boundary value problems

In order to illustrate the capability of this approach, the multiscale approach is then applied to solve geotechnical boundary value problems. By using an explicit-dynamic integral

method, the responses of the system can be tracked the post-peak failure. Two examples are considered with a homogeneous condition and a non-homogeneous condition.

The former presented a cylindrical specimen subjected to a drained triaxial loading path under an isotropically confining stress. By switching the loading control mode from a strain control mode to a stress control mode at the stress peak, the system transforms from a quasi-static regime to a dynamic regime. The internal and external second-order works coincide during the strain-controlled regime. However, as the deviatoric stress reaches the peak, the internal and external second-order works both vanish. The difference between internal and external second-order works implies that the second-order time derivative of the kinetic energy is positive, resulting in an abrupt increase of system kinetic energy.

The latter illustrates a strip footing problem in plane strain conditions as a non-homogeneous boundary value problem. From a numerical point of view, it verifies that when no effective failure occurs, both internal and external second-order works coincide. This is a great advantage since the external second-order can be obtained in a straightforward manner from the boundary variables without requiring internal information (internal stress or strain fields), especially for the geotechnical engineering problem.

Finally, taking advantage of the multiscale approach, the analysis can also be carried out on the REV scale. The vanishing of the second-order work, as a convenient indicator of material instability, reveals a close correlation with the occurrence of strain localization. For the sake of illustration, three Gauss points were selected to examine local responses, illustrating the difference in the mechanical responses inside and outside shear band areas.

6.2 Recommendations

In this dissertation, great effort has been made to explore recent constitutive modeling of granular materials. However, the research work accomplished here is far from being complete as other aspects of the problem can still be investigated.

Although the current 3D-H model is shown to be robust, there are still some aspects to be considered in order to increase the performance of this model. For instance, more sophisticated mechanisms of particle rearrangement should be considered. The current version of 3D-H model only breaks meso-structures when there is more than one contact that open, but no creation mechanism of the meso-structure is included. As a result, the response of this model under large strains is imperfect. Thus, the first question to be addressed is: how and when to create new meso-structures in order to improve the behavior under large strains? More generally, instead of creating new meso-structures, more different forms of meso-structures can be considered, such as the tetrahedron made up of four particles. The particle rearrangement of the specimen can be reflected in the transition between different meso-structures, as it is a more natural phenomenon in granular materials.

Natural processes usually involve multiphysics phenomena, such as heat and mass transportation, electro-magnetic radiation and wave propagation inside a deformed solid body. For the case of a granular soil, granular particles usually coexist with water and air (even frozen ice, methane-hydrate, and oil). The multiphase character of soil actually has been well recognized by researchers and engineers, and unsaturated soil mechanics is one of the most actively explored areas on the subject. For simplicity, only two phases have been considered here: the solid skeleton and the pore water, i.e. the fully saturated granular media. In addition, the erosion and diffusion processes need to be considered. One possibility is to consider a non-fixed particle which can move into the meso-structure or remove from

it, resulting in the different behavior on the mesoscale. Thus, the erosion and diffusion processes can be considered.

Bibliography

- K. A. Alshibli, S. N. Batiste, and S. Sture. Strain localization in sand: plane strain versus triaxial compression. *Journal of Geotechnical and Geoenvironmental Engineering*, 129(6):483–494, 2003.
- A. Anandarajah. Modeling liquefaction by a multimechanism model. *Journal of geotechnical and geoenvironmental engineering*, 134(7):949–959, 2008.
- S. A. Anderson and M. F. Riemer. Collapse of saturated soil due to reduction in confinement. *Journal of geotechnical engineering*, 121(2):216–220, 1995.
- J. E. Andrade and X. X. Tu. Multiscale framework for behavior prediction in granular media. *Mechanics of Materials*, 41(6):652–669, 2009.
- J. E. Andrade, C. F. Avila, S. A. Hall, N. Lenoir, and G. Viggiani. Multiscale modeling and characterization of granular matter: from grain kinematics to continuum mechanics. *Journal of the Mechanics and Physics of Solids*, 59(2):237–250, 2011.
- S. J. Antony. Evolution of force distribution in three-dimensional granular media. *Physical Review E*, 63(1):011302, 2000.
- E. Azéma, F. Radjai, R. Peyroux, and G. Saussine. Force transmission in a packing of pentagonal particles. *Physical Review E*, 76(1):011301, 2007.
- K. Bagi. On the definition of stress and strain in granular assemblies through the relation between micro-and macro-level characteristics. *Powders & grains*, 93:117–121, 1993.
- K. Bagi. Stress and strain in granular assemblies. *Mechanics of materials*, 22(3):165–177, 1996.
- Z. P. Bažant. Endochronic inelasticity and incremental plasticity. *International Journal of Solids and Structures*, 14(9):691–714, 1978.
- R. P. Behringer, K. E. Daniels, T. S. Majmudar, and M. Sperl. Fluctuations, correlations and transitions in granular materials: statistical mechanics for a non-conventional system. *Philosophical Transactions of the Royal Society of London A: Mathematical, Physical and Engineering Sciences*, 366(1865):493–504, 2008.
- P. Bésuelle and J. W. Rudnicki. Localization: shear bands and compaction bands. *INTERNATIONAL GEOPHYSICS SERIES.*, 89:219–322, 2004.

- D. Bigoni. Bifurcation and instability of non-associative elastoplastic solids. In *Material instabilities in elastic and plastic solids*, pages 1–52. Springer, 2000.
- D. Bigoni and T. Hueckel. Uniqueness and localization—i. associative and non-associative elastoplasticity. *International Journal of Solids and structures*, 28(2):197–213, 1991.
- D. L. Blair, N. W. Mueggenburg, A. H. Marshall, H. M. Jaeger, and S. R. Nagel. Force distributions in three-dimensional granular assemblies: Effects of packing order and interparticle friction. *Physical review E*, 63(4):041304, 2001.
- E. W. Brand. Some thoughts on rain-induced slope failures. In *Proceedings of the 10th International Conference on Soil Mechanics and Foundation Engineering, Stockholm*, volume 3, pages 373–376, 1981.
- F. Calvetti, G. Combe, and J. Lanier. Experimental micromechanical analysis of a 2d granular material: relation between structure evolution and loading path. *Mechanics of Cohesive-frictional Materials*, 2(2):121–163, 1997.
- B. Cambou, P. Dubujet, F. Emeriault, and F. Sidoroff. Homogenization for granular materials. *European journal of mechanics. A. Solids*, 14(2):255–276, 1995.
- B. Cambou, M. Chaze, and F. Dedecker. Change of scale in granular materials. *European Journal of Mechanics-A/Solids*, 19(6):999–1014, 2000.
- B. Cambou, P. Dubujet, and C. Nougier-Lehon. Anisotropy in granular materials at different scales. *Mechanics of materials*, 36(12):1185–1194, 2004.
- B. Cambou, M. Jean, et al. *Micromechanics of granular materials*. John Wiley & Sons, 2013.
- A. Casagrande. Liquefaction and cyclic deformation of sands—a critical review. In *Fifth Panamerican Conference on Soil Mechanics and Foundation Engineering*, 1975.
- J. Casey and P. M. Naghdi. On the characterization of strain-hardening in plasticity. *Journal of Applied Mechanics*, 48(2):285–296, 1981.
- G. Castro. Liquefaction of sands. *ph. D. Thesis, Harvard Soil Mech.*, 1969.
- N. Challamel, F. Nicot, J. Lerbet, and F. Darve. On the stability of non-conservative elastic systems under mixed perturbations. *European Journal of Environmental and Civil Engineering*, 13(3):347–367, 2009.
- N. Challamel, F. Nicot, J. Lerbet, and F. Darve. A theoretical link between second-order work and stability under kinematics constraints. *Eng. Struct*, 32:3086–3092, 2010.
- C. S. Chang. Micromechanical modelling of constitutive relations for granular material. *Micromechanics of Granular Materials*, pages 271–278, 1987.
- C. S. Chang and A. Misra. Stress-strain behavior of sands—a microstructural approach. In *Proceedings, Fourth International Symposium on Interaction of Non-Nuclear Ammunition with Structures, Panama City Beach, Florida*, pages 354–459, 1989.

- C. S. Chang and Z. Y. Yin. Micromechanical modeling for inherent anisotropy in granular materials. *Journal of engineering mechanics*, 136(7):830–839, 2009.
- C. S. Chang, A. Misra, and S. S. Sundaram. Micromechanical modelling of cemented sands under low amplitude oscillations. *Geotechnique*, 40(2), 1990.
- C. S. Chang, Y. Chang, and M. G. Kabir. Micromechanics modeling for stress-strain behavior of granular soils. i: Theory. *Journal of geotechnical engineering*, 118(12):1959–1974, 1992.
- C. S. Chang, P. Y. Hicher, Z. Y. Yin, and L. R. Kong. Elastoplastic model for clay with microstructural consideration. *Journal of engineering mechanics*, 135(9):917–931, 2009.
- C. S. Chang, Z. Y. Yin, and P. Y. Hicher. Micromechanical analysis for interparticle and assembly instability of sand. *Journal of Engineering Mechanics*, 137(3):155–168, 2010.
- J. Christoffersen, M. M. Mehrabadi, and S. Nemat-Nasser. A micromechanical description of granular material behavior. *Journal of Applied Mechanics*, 48(2):339–344, 1981.
- J. Chu, S. Leroueil, and W. K. Leong. Unstable behaviour of sand and its implication for slope instability. *Canadian Geotechnical Journal*, 40(5):873–885, 2003.
- R. Courant. Variational methods for the solution of problems of equilibrium and vibrations. *Bulletin of the American mathematical Society*, 49(1):1–23, 1943.
- P. A. Cundall and R. D. Hart. Numerical modelling of discontinua. *Engineering computations*, 9(2):101–113, 1992.
- P. A. Cundall and O. D. L. Strack. A discrete numerical model for granular assemblies. *Géotechnique*, 29(1):47–65, 1979.
- P. Dantu. Etude statistique des forces intergranulaires dans un milieu pulvérulent. *Géotechnique*, 18(1):50–55, 1968.
- F. Darve. The expression of rheological laws in incremental form and the main classes of constitutive equations. *Geomaterials: Constitutive Equations and Modelling*, pages 123–148, 1990.
- F. Darve. Stability and uniqueness in geomaterials constitutive modelling. *Localisation and Bifurcation Theory for Soils and Rocks*, pages 73–88, 1994.
- F. Darve, E. Flavigny, and M. Meghachou. Yield surfaces and principle of superposition: revisit through incrementally non-linear constitutive relations. *International Journal of Plasticity*, 11(8):927–948, 1995.
- F. Darve, G. Servant, F. Laouafa, and H. D. V. Khoa. Failure in geomaterials: continuous and discrete analyses. *Computer methods in applied mechanics and engineering*, 193(27):3057–3085, 2004.
- F. Darve, L. Sibille, A. Daouadji, and F. Nicot. Bifurcations in granular media: macro-and micro-mechanics approaches. *Comptes Rendus Mécanique*, 335(9-10):496–515, 2007.

- G. De Saxcé, J. Fortin, and O. Millet. About the numerical simulation of the dynamics of granular media and the definition of the mean stress tensor. *Mechanics of Materials*, 36(12):1175–1184, 2004.
- J. Desrues and G. Viggiani. Strain localization in sand: an overview of the experimental results obtained in grenoble using stereophotogrammetry. *International Journal for Numerical and Analytical Methods in Geomechanics*, 28(4):279–321, 2004.
- J. Desrues, R. Chambon, M. Mokni, and F. Mazerolle. Void ratio evolution inside shear bands in triaxial sand specimens studied by computed tomography. *Géotechnique*, 46(3):529–546, 1996.
- A. Drescher and G. D. J. De Jong. Photoelastic verification of a mechanical model for the flow of a granular material. *Journal of the Mechanics and Physics of Solids*, 20(5):337–340, 1972.
- D. C. Drucker and W. Prager. Soil mechanics and plastic analysis or limit design. *Quarterly of applied mathematics*, 10, 2013.
- D. C. Drucker, W. Prager, and H. J. Greenberg. Extended limit design theorems for continuous media. *Quarterly of Applied Mathematics*, 9(4):381–389, 1952.
- F. Emeriault and B. Cambou. Micromechanical modelling of anisotropic non-linear elasticity of granular medium. *International Journal of Solids and Structures*, 33(18):2591–2607, 1996.
- J. M. Erikson, N. W. Mueggenburg, H. M. Jaeger, and S. R. Nagel. Force distributions in three-dimensional compressible granular packs. *Physical Review E*, 66(4):040301, 2002.
- R. J. Finno, W. W. Harris, M. A. Mooney, and G. Viggiani. Shear bands in plane strain compression of loose sand. *Geotechnique*, 47(1):149–165, 1997.
- J. Fonseca, W. W. Sim, T. Shire, and C. O’Sullivan. Microstructural analysis of sands with varying degrees of internal stability. *Géotechnique*, 64(5):405, 2014.
- A. Gajo and M. Wood. Severn–trent sand: a kinematic-hardening constitutive model: the q–p formulation. *Géotechnique*, 49(5):595–614, 1999.
- Z. W. Gao and J. D. Zhao. Constitutive modeling of artificially cemented sand by considering fabric anisotropy. *Computers and Geotechnics*, 41:57–69, 2012.
- Z. W. Gao, J. D. Zhao, X. S. Li, and Y. F. Dafalias. A critical state sand plasticity model accounting for fabric evolution. *International journal for numerical and analytical methods in geomechanics*, 38(4):370–390, 2014.
- N. Guo and J. D. Zhao. A hierarchical model for cross-scale simulation of granular media. In *AIP conference proceedings*, volume 1542, pages 1222–1225, 2013a.
- N. Guo and J. D. Zhao. The signature of shear-induced anisotropy in granular media. *Computers and Geotechnics*, 47:1–15, 2013b.

- N. Guo and J. D. Zhao. A coupled fem/dem approach for hierarchical multiscale modelling of granular media. *International Journal for Numerical Methods in Engineering*, 99(11): 789–818, 2014.
- N. Guo and J. D. Zhao. 3D multiscale modeling of strain localization in granular media. *Computers and Geotechnics*, 2016a.
- N. Guo and J. D. Zhao. Parallel hierarchical multiscale modelling of hydro-mechanical problems for saturated granular soils. *Computer Methods in Applied Mechanics and Engineering*, 305:37–61, 2016b.
- P. J. Guo. *Modelling granular materials with respect to stress-dilatancy and fabric: a fundamental approach*. PhD thesis, University of Calgary, 2000.
- N. Hadda, F. Nicot, F. Bourrier, L. Sibille, F. Radjai, and F. Darve. Micromechanical analysis of second order work in granular media. *Granular matter*, 15(2):221–235, 2013.
- C. Han and A. Drescher. Shear bands in biaxial tests on dry coarse sand. *Soils and Foundations*, 33(1):118–132, 1993.
- K. Hibbitt and Sorensen. *ABAQUS/Explicit: User's Manual*, volume 1. Hibbitt, Karlsson and Sorenson Incorporated, 2001.
- R. Hill. A general theory of uniqueness and stability in elastic-plastic solids. *Journal of the Mechanics and Physics of Solids*, 6(3):236–249, 1958.
- R. Hill. On the classical constitutive relations for elastic/plastic solids. *Recent Progress in Appl. Mech.(The Folke Odqvist Volume)*, pages 241–249, 1967.
- E. Hoque. *Elastic deformation of sands in triaxial tests*. PhD thesis, University of Tokyo, 1996.
- A. Hrennikoff. Solution of problems of elasticity by the framework method. *Journal of applied mechanics*, 8(4):169–175, 1941.
- K. Ishihara. Cyclic behaviour of sand during rotation of principal stress axes. *Mechanic of Granular Material: New Models and Constitutive Equations*, pages 53–73, 1983.
- R. M. Iverson. The physics of debris flows. *Reviews of geophysics*, 35(3):245–296, 1997.
- K. Iwashita and M. Oda. Micro-deformation mechanism of shear banding process based on modified distinct element method. *Powder Technology*, 109(1):192–205, 2000.
- H. M. Jaeger, S. R. Nagel, and R. P. Behringer. Granular solids, liquids, and gases. *Reviews of modern physics*, 68(4):1259, 1996.
- M. Jefferies. Plastic work and isotropic softening in unloading. *Géotechnique*, 47(5), 1997.
- M. Klisinski, Z. Mroz, and K. Runesson. Structure of constitutive equations in plasticity for different choices of state and control variables. *International journal of plasticity*, 8(3): 221–243, 1992.

- D. Kolymbas. An outline of hypoplasticity. *Archive of applied mechanics*, 61(3):143–151, 1991.
- L. Kondic, A. Goulet, C. S. O’Hern, M. Kramar, K. Mischaikow, and R. P. Behringer. Topology of force networks in compressed granular media. *EPL (Europhysics Letters)*, 97(5):54001, 2012.
- N. P. Kruyt. Statics and kinematics of discrete cosserat-type granular materials. *International journal of solids and structures*, 40(3):511–534, 2003.
- N. P. Kruyt and L. Rothenburg. Microinechanical definition of the strain tensor for granular materials. *Appi. Mech*, 118:706–711, 1996.
- N. P. Kruyt and L. Rothenburg. Probability density functions of contact forces for cohesionless frictional granular materials. *International journal of solids and structures*, 39(3):571–583, 2002.
- M. R. Kuhn and K. Bagi. Contact rolling and deformation in granular media. *International journal of solids and structures*, 41(21):5793–5820, 2004.
- P. V. Lade. Static instability and liquefaction of loose fine sandy slopes. *Journal of Geotechnical Engineering*, 118(1):51–71, 1992.
- P. V. Lade. Initiation of static instability in the submarine nerlerk berm. *Canadian Geotechnical Journal*, 30(6):895–904, 1993.
- P. V. Lade and Q Wang. Analysis of shear banding in true triaxial tests on sand. *Journal of Engineering Mechanics*, 127(8):762–768, 2001.
- W. K. Leong. *Instability behaviour of a granular fill material*. PhD thesis, Nanyang Technological University, 2002.
- M. Li and O. Richmond. Intrinsic instability and nonuniformity of plastic deformation. *International journal of plasticity*, 13(8-9):765–784, 1997.
- X. K. Li and K. Wan. A bridging scale method for granular materials with discrete particle assembly–cosserat continuum modeling. *Computers and Geotechnics*, 38(8):1052–1068, 2011.
- X. S. Li and Y. F. Dafalias. Anisotropic critical state theory: role of fabric. *Journal of Engineering Mechanics*, 138(3):263–275, 2011.
- X. S. Li, Y. F. Dafalias, and Z. L. Wang. State-dependant dilatancy in critical-state constitutive modelling of sand. *Canadian Geotechnical Journal*, 36(4):599–611, 1999.
- Y. N. Li and D. G. Karr. Prediction of ductile fracture in tension by bifurcation, localization, and imperfection analyses. *International Journal of Plasticity*, 25(6):1128–1153, 2009.
- S. C. R. Lo and I. K. Lee. Response of granular soil along constant stress increment ratio path. *Journal of Geotechnical Engineering*, 116(3):355–376, 1990.
- A. E. H. Love. *A treatise on the mathematical theory of elasticity*, volume 1. Cambridge University Press, 1927.

- M. P. Luong. Stress-strain aspects of cohesionless soils under cyclic and transient loading. In *Proc., Int. Symp. on Soils under Cyclic and Transient Loading*, volume 1, pages 315–324. Balkema Rotterdam, The Netherlands, 1980.
- T. S. Majmudar and R. P. Behringer. Contact force measurements and stress-induced anisotropy in granular materials. *Nature*, 435(7045):1079, 2005.
- J. Mandel. Cours de mécanique des milieux continus. *Physics Bulletin*, 1:82–83, 1966. URL <https://doi.org/10.1088/0031-9112/18/7/022>.
- M. T. Manzari and Y. F. Dafalias. A critical state two-surface plasticity model for sands. *Geotechnique*, 47(2):255–272, 1997.
- M. M. Mehrabadi, S. Nemat-Nasser, and M. Oda. On statistical description of stress and fabric in granular materials. *International Journal for Numerical and Analytical Methods in Geomechanics*, 6(1):95–108, 1982.
- H. A. Meier, P. Steinmann, and E. Kuhl. Towards multiscale computation of confined granular media—contact forces, stresses and tangent operators. *Technische Mechanik*, 28(1):32–42, 2008.
- H. A. Meier, P. Steinmann, and E. Kuhl. On the multiscale computation of confined granular media. In *ECCOMAS Multidisciplinary Jubilee Symposium*, pages 121–133. Springer, 2009.
- C. Miehe, J. Dettmar, and D. Zäh. Homogenization and two-scale simulations of granular materials for different microstructural constraints. *International Journal for Numerical Methods in Engineering*, 83(8-9):1206–1236, 2010.
- R. D. Mindlin. Elastic spheres in contact under varying oblique forces. *Trans. ASME, J. Appl. Mech.*, 20:327–344, 1953.
- N. W. Mueggenburg, H. M. Jaeger, and S. R. Nagel. Stress transmission through three-dimensional ordered granular arrays. *Physical Review E*, 66(3):031304, 2002.
- D. M. Mueth, H. M. Jaeger, and S. R. Nagel. Force distribution in a granular medium. *Physical Review E*, 57(3):3164, 1998.
- M. K. Neilsen and H. L. Schreyer. Bifurcations in elastic-plastic materials. *International Journal of Solids and Structures*, 30(4):521–544, 1993.
- N. S. Nguyen, H. Magoariec, B. Cambou, and A. Danescu. Analysis of structure and strain at the meso-scale in 2d granular materials. *International journal of solids and structures*, 46(17):3257–3271, 2009.
- N. S. Nguyen, H. Magoariec, and B. Cambou. Local stress analysis in granular materials at a mesoscale. *International Journal for Numerical and Analytical Methods in Geomechanics*, 36(14):1609–1635, 2012.
- T. Nguyen, G. Combe, D. Caillerie, and J. Desrues. Fem× dem modelling of cohesive granular materials: numerical homogenisation and multi-scale simulations. *Acta Geophysica*, 62(5):1109–1126, 2014.

- F. Nicot. Constitutive modelling of a snow cover with a change in scale. *European Journal of Mechanics-A/Solids*, 22(3):325–340, 2003.
- F. Nicot and F. Darve. A micro-mechanical investigation of bifurcation in granular materials. *International Journal of Solids and Structures*, 44(20):6630–6652, 2007.
- F. Nicot and F. Darve. Diffuse and localized failure modes: two competing mechanisms. *International Journal for Numerical and Analytical Methods in Geomechanics*, 35(5):586–601, 2011a.
- F. Nicot and F. Darve. The H-microdirectional model: accounting for a mesoscopic scale. *Mechanics of Materials*, 43(12):918–929, 2011b.
- F. Nicot, F. Darve, and RNVO Group. A multi-scale approach to granular materials. *Mechanics of materials*, 37(9):980–1006, 2005.
- F. Nicot, F. Darve, and H. D. V. Khoa. Bifurcation and second-order work in geomaterials. *International journal for numerical and analytical methods in geomechanics*, 31(8):1007–1032, 2007a.
- F. Nicot, L. Sibille, F. Donze, and F. Darve. From microscopic to macroscopic second-order work in granular assemblies. *Mechanics of materials*, 39(7):664–684, 2007b.
- F. Nicot, L. Sibille, and F. Darve. Bifurcation in granular materials: An attempt for a unified framework. *International Journal of Solids and Structures*, 46(22):3938–3947, 2009.
- F. Nicot, N. Hadda, M. Guessasma, J. Fortin, and O. Millet. On the definition of the stress tensor in granular media. *International Journal of Solids and Structures*, 50(14):2508–2517, 2013.
- F. Nicot, J. Lerbet, and F. Darve. Second-order work criterion: from material point to boundary value problems. *Acta Mechanica*, pages 1–16, 2017.
- M. Nitka, G. Combe, C. Dascalu, and J. Desrues. Two-scale modeling of granular materials: a dem-fem approach. *Granular Matter*, 13(3):277–281, 2011.
- R. Nova. Controllability of the incremental response of soil specimens subjected to arbitrary loading programmes. *Journal of the Mechanical behavior of Materials*, 5(2):193–202, 1994.
- R. Nova and D. M. Wood. A constitutive model for soil under monotonic and cyclic loading, 1982.
- M. Oda. Deformation mechanism of sand in triaxial compression tests. *Soils and Foundations*, 12(4):45–63, 1972a.
- M. Oda. Initial fabrics and their relations to mechanical properties of granular material. *Soils and foundations*, 12(1):17–36, 1972b.
- M. Oda. The mechanism of fabric changes during compressional deformation of sand. *Soils and foundations*, 12(2):1–18, 1972c.

- M. Oda and K. Iwashita. Study on couple stress and shear band development in granular media based on numerical simulation analyses. *International journal of engineering science*, 38(15):1713–1740, 2000.
- M. Oda, J. Konishi, and S. Nemat-Nasser. Some experimentally based fundamental results on the mechanical behaviour of granular materials. *Geotechnique*, 30(4):479–495, 1980.
- M. Oda, J. Konishi, and S. Nemat-Nasser. Experimental micromechanical evaluation of strength of granular materials: effects of particle rolling. *Mechanics of materials*, 1(4):269–283, 1982.
- M. Oda, K. Iwashita, and T. Kakiuchi. Importance of particle rotation in the mechanics of granular materials. *Powders and grains*, 97:207–210, 1997.
- H. Petryk. Theory of bifurcation and instability in time-independent plasticity. In *Bifurcation and stability of dissipative systems*, pages 95–152. Springer, 1993.
- W. Prager. The general theory of limit design. In *Proceedings of the 8th International Congress on theoretical and Applied Mechanics, Istanbul*, volume 19, pages 65–72, 1952.
- J. H. Prevost and K. Hoeg. Soil mechanics and plasticity analysis of strain softening. *Geotechnique*, 25(2):279–297, 1975.
- F. Prunier, F. Laouafa, S. Lignon, and F. Darve. Bifurcation modeling in geomaterials: From the second-order work criterion to spectral analyses. *International Journal for Numerical and Analytical Methods in Geomechanics*, 33(9):1169–1202, 2009a.
- F. Prunier, F. Nicot, F. Darve, F. Laouafa, and S. Lignon. Three-dimensional multiscale bifurcation analysis of granular media. *Journal of Engineering Mechanics*, 135(6):493–509, 2009b.
- F. Radjai and F. Dubois. *Discrete-element modeling of granular materials*. Wiley-Iste, 2011.
- F. Radjai and S. Roux. Friction-induced self-organization of a one-dimensional array of particles. *Physical Review E*, 51(6):6177, 1995.
- F. Radjai, M. Jean, J. J. Moreau, and S. Roux. Force distributions in dense two-dimensional granular systems. *Physical review letters*, 77(2):274, 1996.
- F. Radjai, D. E. Wolf, M. Jean, and J. J. Moreau. Bimodal character of stress transmission in granular packings. *Physical review letters*, 80(1):61, 1998.
- F. Radjai, S. Roux, and J. J. Moreau. Contact forces in a granular packing. *Chaos: An Interdisciplinary Journal of Nonlinear Science*, 9(3):544–550, 1999.
- A. L. Rechenmacher. Grain-scale processes governing shear band initiation and evolution in sands. *Journal of the Mechanics and Physics of Solids*, 54(1):22–45, 2006.
- O. Reynolds. Lvi. on the dilatancy of media composed of rigid particles in contact. with experimental illustrations. *The London, Edinburgh, and Dublin Philosophical Magazine and Journal of Science*, 20(127):469–481, 1885.

- J. R. Rice. On the structure of stress-strain relations for time-dependent plastic deformation in metals. *Journal of applied mechanics*, 37(3):728–737, 1970.
- J. R. Rice. Continuum mechanics and thermodynamics of plasticity in relation to microscale deformation mechanisms. *Constitutive Equations in Plasticity. Massachusetts Institute of Technology Press, Cambridge*. 1975, 23-79, 1975.
- J. R. Rice. The localization of plastic deformation. *Theoretical and Applied Mechanics*, pages 207–220, 1976.
- K. H. Roscoe, A. N. Schofield, and A. Thurairajah. Yielding of clays in states wetter than critical. *Geotechnique*, 13(3):211–240, 1963.
- L. Rothenburg and R. J. Bathurst. Analytical study of induced anisotropy in idealized granular materials. *Geotechnique*, 39(4):601–614, 1989.
- P. W. Rowe. The stress-dilatancy relation for static equilibrium of an assembly of particles in contact. In *Proceedings of the royal society of London a: mathematical, physical and engineering sciences*, volume 269, pages 500–527. The Royal Society, 1962.
- P. W. Rowe. The relation between the shear strength of sands in triaxial compression, plane strain and direct. *Geotechnique*, 19(1):75–86, 1969.
- J. W. Rudnicki and J. R. Rice. Conditions for the localization of deformation in pressure-sensitive dilatant materials. *Journal of the Mechanics and Physics of Solids*, 23(6):371–394, 1975.
- K. Runesson and Z. Mroz. A note on nonassociated plastic flow rules. *International journal of plasticity*, 5(6):639–658, 1989.
- S. Sasitharan, P.K. Robertson, D. C. Sego, and N. R. Morgenstern. Collapse behavior of sand. *Canadian Geotechnical Journal*, 30(4):569–577, 1993.
- M. Satake. A discrete-mechanical approach to granular materials. *International journal of engineering science*, 30(10):1525–1533, 1992.
- Y. Shigeto and M. Sakai. Parallel computing of discrete element method on multi-core processors. *Particuology*, 9(4):398–405, 2011.
- L. Sibille, F. Nicot, F. V. Donze, and F. Darve. Material instability in granular assemblies from fundamentally different models. *International Journal For Numerical and Analytical Methods in Geomechanics*, 31(3):457–481, 2007.
- L. Sibille, F. Donzé, F. Nicot, B. Chareyre, and F. Darve. Bifurcation detection and catastrophic failure. *Acta Geotechnica*, 3(1):14–24, 2008.
- L. E. Silbert, G. S. Grest, and J. W. Landry. Statistics of the contact network in frictional and frictionless granular packings. *Physical Review E*, 66(6):061303, 2002.
- C. M. Song, P. Wang, and H. Makse. A phase diagram for jammed matter. *Nature*, 453(7195):629, 2008.

- A. J. M. Spencer. Isotropic polynomial invariants and tensor functions. In *Applications of tensor functions in solid mechanics*, pages 141–169. Springer, 1987.
- J. Stránský and M. Jirásek. Open source fem-dem coupling. *Engineering Mechanics*, page 18, 2012.
- J. Sulem and I. G. Vardoulakis. *Bifurcation analysis in geomechanics*. CRC Press, 2004.
- D. W. Taylor. *Fundamentals of soil mechanics.*, volume 66. Wiley: New York, 1948.
- D. W. Taylor. *Fundamentals of soil mechanics*. J. Wiley & Sons; London: Chapman & Hall, 1956.
- K. Terzaghi. *Theory of consolidation*. Wiley: New York, 1943.
- C. Thornton and S. J. Antony. Quasi-static deformation of particulate media. *Philosophical transactions-royal society of London series a mathematical physical and engineering sciences*, pages 2763–2782, 1998.
- A. Tordesillas. Force chain buckling, unjamming transitions and shear banding in dense granular assemblies. *Philosophical Magazine*, 87(32):4987–5016, 2007.
- K. C. Valanis. On the uniqueness of solution of the initial value problem in softening materials. *Journal of applied mechanics*, 52(3):649–653, 1985.
- K. C. Valanis. Banding and stability in plastic materials. *Acta mechanica*, 79(1):113–141, 1989.
- R. Valentino, G. Barla, and L. Montrasio. Experimental analysis and micromechanical modelling of dry granular flow and impacts in laboratory flume tests. *Rock Mechanics and Rock Engineering*, 41(1):153–177, 2008.
- I. Vardoulakis. Shear band inclination and shear modulus of sand in biaxial tests. *International Journal for Numerical and Analytical Methods in Geomechanics*, 4(2):103–119, 1980.
- I. Vardoulakis. Deformation of water-saturated sand: I. uniform undrained deformation and shear banding. *Géotechnique*, 46(3):441–456, 1996.
- I. Vardoulakis, M. Goldscheider, and G. Gudehus. Formation of shear bands in sand bodies as a bifurcation problem. *International Journal for numerical and analytical methods in Geomechanics*, 2(2):99–128, 1978.
- R. Verdugo and K. Ishihara. The steady state of sandy soils. *Soils and foundations*, 36(2): 81–91, 1996.
- G. Viggiani, R. J. Finno, and W. W. Harris. Experimental observations of strain localisation in plane strain compression of a stiff clay. *Localization and bifurcation theory for soils and rocks*, pages 189–198, 1994.
- W. Voigt. Ueber die beziehung zwischen den beiden elasticitätsconstanten isotroper körper. *Annalen der Physik*, 274(12):573–587, 1889.

- R. Wan, M. Pinheiro, A. Daouadji, M. Jrad, and F. Darve. Diffuse instabilities with transition to localization in loose granular materials. *International Journal for Numerical and Analytical Methods in Geomechanics*, 37(10):1292–1311, 2013.
- P. Wang, C. M. Song, Y. L. Jin, K. Wang, and H. Makse. Distribution of volumes and coordination numbers in jammed matter: mesoscopic ensemble. *Journal of Statistical Mechanics: Theory and Experiment*, 2010(12):P12005, 2010.
- Q. Wang and P. V. Lade. Shear banding in true triaxial tests and its effect on failure in sand. *Journal of Engineering Mechanics*, 127(8):754–761, 2001.
- C. Wellmann and P. Wriggers. A two-scale model of granular materials. *Computer Methods in Applied Mechanics and Engineering*, 205:46–58, 2012.
- Z. X. Wu, Z. Y. Yin, Y. F. Jin, and X. Y. Geng. A straightforward procedure of parameters determination for sand: a bridge from critical state based constitutive modelling to finite element analysis. *European Journal of Environmental and Civil Engineering*, pages 1–23, 2017.
- Y. P. Yao, D. A. Sun, and H. Matsuoka. A unified constitutive model for both clay and sand with hardening parameter independent on stress path. *Computers and Geotechnics*, 35(2): 210–222, 2008.
- Z. Y. Yin, C. S. Chang, P. Y. Hicher, and M. Karstunen. Micromechanical analysis of kinematic hardening in natural clay. *International Journal of Plasticity*, 25(8):1413–1435, 2009.
- Z. Y. Yin, C. S. Chang, and P. Y. Hicher. Micromechanical modelling for effect of inherent anisotropy on cyclic behaviour of sand. *International Journal of Solids and Structures*, 47(14):1933–1951, 2010a.
- Z. Y. Yin, C. S. Chang, M. Karstunen, and P. Y. Hicher. An anisotropic elastic–viscoplastic model for soft clays. *International Journal of Solids and Structures*, 47(5):665–677, 2010b.
- Z. Y. Yin, M. Hattab, and P. Y. Hicher. Multiscale modeling of a sensitive marine clay. *International Journal for Numerical and Analytical Methods in Geomechanics*, 35(15): 1682–1702, 2011a.
- Z. Y. Yin, M. Karstunen, C. S. Chang, M. Koskinen, and M. Lojander. Modeling time-dependent behavior of soft sensitive clay. *Journal of Geotechnical and Geoenvironmental Engineering*, 137(11):1103–1113, 2011b.
- Z. Y. Yin, Q. Xu, and P. Y. Hicher. A simple critical-state-based double-yield-surface model for clay behavior under complex loading. *Acta Geotechnica*, 8(5):509–523, 2013.
- Z. Y. Yin, J. D. Zhao, and P. Y. Hicher. A micromechanics-based model for sand-silt mixtures. *International journal of solids and structures*, 51(6):1350–1363, 2014.
- J. D. Zhao and N. Guo. Unique critical state characteristics in granular media considering fabric anisotropy. *Géotechnique*, 63(8):695, 2013.

- H. N. Zhu, M. M. Mehrabadi, and M. Massoudi. Three-dimensional constitutive relations for granular materials based on the dilatant double shearing mechanism and the concept of fabric. *International journal of plasticity*, 22(5):826–857, 2006.
- H. X. Zhu. *Including a meso-structure in multi-scale modeling of granular soils*. PhD thesis, Université Grenoble Alpes, 2015.
- H. X. Zhu, H. N. G. Nguyen, F. Nicot, and F. Darve. On a common critical state in localized and diffuse failure modes. *Journal of the Mechanics and Physics of Solids*, 95:112–131, 2016.

Appendix A

Detailed formulation in the 3D-H model

A.1 Inter-particle contact law

This elastic-perfect plastic model includes a Mohr-Coulomb criterion and can be expressed under the following incremental formalism by employing the notations depicted in [Figure 3.6](#) and [Figure 3.7](#):

$$\begin{cases} \delta N_i = k_n \delta u_n^i \\ \delta T_i = \min \left\{ \|T_i + k_t \delta u_t^i\|, \tan \varphi_g (N_i + k_n \delta u_n^i) \right\} \times \frac{T_i + k_t \delta u_t^i}{\|T_i + k_t \delta u_t^i\|} - T_i \end{cases} \quad (\text{A.1})$$

where: $i = 1, 2, 3, 4$ denotes the contact number.

According to [Equations 3.21](#), [Equations A.1](#) can be rewritten as follows:

$$\begin{cases} \delta N_i = -k_n \delta d_i \\ \delta T_i = k_t d_i \delta \alpha_j & \text{elastic regime} \\ \delta T_i = \tan \varphi_g (N_i - k_n \delta d_i) \xi_i - T_i & \text{plastic regime} \end{cases} \quad (\text{A.2})$$

where: ξ_i is the sign of $T_i + k_t d_i \delta \alpha_j$; $j = 1$ when $i = 1, 2$; $j = 2$ when $i = 3, 4$; plastic regime is reached when $\|k_t d_i \delta \alpha_j + T_i\| \geq \tan \varphi_g (N_i - k_n \delta d_i)$, otherwise elastic regime holds.

For the sake of convenience, I_i^p and I_i^e are introduced as indicator functions of the contact state, expressed as below:

$$I_i^p = \begin{cases} 1 & \text{in plastic regime} \\ 0 & \text{in elastic regime} \end{cases} ; \quad I_i^e = 1 - I_i^p \quad (\text{A.3})$$

Thus, the constitutive relations can be expressed as follows:

$$\begin{cases} \delta N_i = -k_n \delta d_i \\ \delta T_i = B_i \delta \alpha_j - A_i \delta d_i + C_i \end{cases} \quad (\text{A.4})$$

$$\text{where: } \begin{cases} A_i = I_i^p k_n \xi_i \tan \varphi_g \\ B_i = I_i^e k_t d_i \\ C_i = I_i^p (\xi_i \tan \varphi_g N_i - T_i) \end{cases}$$

A.2 Stiffness matrix on the mesoscopic scale

For Hexagon A, combining [Equations 3.21](#) and [Equations 3.26](#) gives:

$$\begin{cases} \delta F_1^a = -k_n \cos \alpha_1 \delta d_1 + (k_t \sin \alpha_1 d_1 - F_2) \delta \alpha_1 \\ \delta F_2 = -k_n \sin \alpha_1 \delta d_1 + (F_1^a - k_t \cos \alpha_1 d_1) \delta \alpha_1 \end{cases} \quad (\text{A.5})$$

Based on [Equation 3.25](#), δd_1 and $\delta \alpha_1$ can be expressed as follows:

$$\begin{cases} \delta d_1 = \frac{1}{|D|^a} \left(2d_1 \cos \alpha_1 \delta l_1 + \frac{B_1}{k_n} \sin \alpha_1 \delta l_2 + \frac{B_1}{k_n} \delta l_2 - \frac{F_2}{k_n} \delta l_2 + 2d_1 \sin \alpha_1 \delta l_2 \right) \\ \delta \alpha_1 = \frac{1}{|D|^a} \left(-2 \sin \alpha_1 \delta l_1 + \frac{A_1}{k_n} \sin \alpha_1 \delta l_2 + \frac{A_1}{k_n} \delta l_2 + 3 \cos \alpha_1 \delta l_2 \right) \end{cases} \quad (\text{A.6})$$

where: $|D|^a = \frac{2}{k_n} [(B_1 \sin \alpha_1 + A_1 d_1 \cos \alpha_1)(\sin \alpha_1 + 1) - F_2 \sin \alpha_1 + k_n d_1 \cos^2 \alpha_1 + 2k_n d_1]$

Then, [Equations A.6](#) is substituted into [Equations A.5](#):

$$\begin{bmatrix} K_{11}^a & K_{12}^a \\ K_{21}^a & K_{22}^a \end{bmatrix} \begin{bmatrix} \delta l_1 \\ \delta l_2 \end{bmatrix} = \begin{bmatrix} \delta F_1^a \\ \delta F_2 \end{bmatrix} \quad (\text{A.7})$$

where:

$$\begin{cases} K_{11}^a = \frac{2}{|D|^a} (F_2 \sin \alpha_1 - k_n d_1 \cos^2 \alpha_1 - k_t d_1 \sin^2 \alpha_1) \\ K_{12}^a = \frac{1}{|D|^a} (k_t d_1 \sin \alpha_1 - F_2) \left(\frac{A_1}{k_n} \sin \alpha_1 + \frac{A_1}{k_n} + 3 \cos \alpha_1 \right) \\ \quad - \frac{1}{|D|^a} \cos \alpha_1 (B_1 \sin \alpha_1 + B_1 - F_2 + 2k_n d_1 \sin \alpha_1) \\ K_{21}^a = \frac{2}{|D|^a} (k_t - k_n) d_1 \sin \alpha_1 \cos \alpha_1 - 2F_1^a \sin \alpha_1 \\ K_{22}^a = \frac{1}{|D|^a} (F_1^a - k_t d_1 \cos \alpha_1) \left(\frac{A_1}{k_n} \sin \alpha_1 + \frac{A_1}{k_n} + 3 \cos \alpha_1 \right) \\ \quad - \frac{1}{|D|^a} \sin \alpha_1 (B_1 \sin \alpha_1 + B_1 - F_2 + 2k_n d_1 \sin \alpha_1) \end{cases} \quad (\text{A.8})$$

Similarly, for Hexagon B:

$$\begin{bmatrix} K_{11}^b & K_{12}^b \\ K_{21}^b & K_{22}^b \end{bmatrix} \begin{bmatrix} \delta l_1 \\ \delta l_3 \end{bmatrix} = \begin{bmatrix} \delta F_1^b \\ \delta F_3 \end{bmatrix} \quad (\text{A.9})$$

where:

$$\left\{ \begin{array}{l} K_{11}^b = \frac{2}{|D|^b} (F_3 \sin \alpha_2 - k_n d_3 \cos^2 \alpha_2 - k_t d_3 \sin^2 \alpha_2) \\ K_{12}^b = \frac{1}{|D|^b} (k_t d_3 \sin \alpha_2 - F_3) \left(\frac{A_3}{k_n} \sin \alpha_2 + \frac{A_3}{k_n} + 3 \cos \alpha_2 \right) \\ \quad - \frac{1}{|D|^b} \cos \alpha_2 (B_3 \sin \alpha_2 + B_3 - F_3 + 2k_n d_3 \sin \alpha_2) \\ K_{21}^b = \frac{2}{|D|^b} (k_t - k_n) d_3 \sin \alpha_2 \cos \alpha_2 - 2F_1^b \sin \alpha_2 \\ K_{22}^b = \frac{1}{|D|^b} (F_1^b - k_t d_3 \cos \alpha_2) \left(\frac{A_3}{k_n} \sin \alpha_2 + \frac{A_3}{k_n} + 3 \cos \alpha_2 \right) \\ \quad - \frac{1}{|D|^b} \sin \alpha_2 (B_3 \sin \alpha_2 + B_3 - F_3 + 2k_n d_3 \sin \alpha_2) \end{array} \right. \quad (\text{A.10})$$

with: $|D|^b = \frac{2}{k_n} [(B_3 \sin \alpha_2 + A_3 d_3 \cos \alpha_2)(\sin \alpha_2 + 1) - F_3 \sin \alpha_2 + k_n d_3 \cos^2 \alpha_2 + 2k_n d_3]$

Finally, [Equation 3.29](#) is recovered, with:

$$\left\{ \begin{array}{l} \delta F_1 = (K_{11}^a + K_{11}^b) \delta l_1 + K_{12}^a \delta l_2 + K_{12}^b \delta l_3 \\ \delta F_2 = K_{21}^a \delta l_1 + K_{22}^a \delta l_2 \\ \delta F_3 = K_{21}^b \delta l_1 + K_{22}^b \delta l_3 \end{array} \right. \quad (\text{A.11})$$

Appendix B

Abaqus and VUMAT

This appendix briefly overviews the main framework of Abaqus, a finite element method software package designed for solving general purpose engineering problems numerically. The aim here is how Abaqus works and how it is organized. The structure of the user-defined material subroutine for the dynamic problem, VUMAT, is also introduced and explained in more details. The content put forward in this appendix was retrieved from Abaqus' manuals, to which it is here simply referred to as (Hibbitt and Sorensen, 2001). Readers familiar with Abaqus and VUMAT operating frameworks may skip this appendix.

B.1 Framework

Abaqus is a commercial package of FEM-based programs designed to simulate a wide variety of engineering problems ranging from relatively simple linear analysis to more complex nonlinear ones. Some of the engineering areas Abaqus engages in are stress-displacement problems, heat transfer, mass diffusion, coupled thermal-electrical analysis, acoustics, soil mechanics and piezoelectric analysis. As expressed before, our sole interest here is in the soil mechanics analysis mostly involving the geotechnical aspects (Hibbitt and Sorensen, 2001)

There are two main solvers or analysis products: the Standard and the Explicit. The former (Abaqus/Standard) is used to perform general-purpose analysis of either linear or nonlinear static, dynamic, thermal and electrical response. The latter (Abaqus/Explicit) is used in the specific-purpose analysis that is suitable for modelling transient dynamic events of short duration such as impact and instabilities. Another fundamental feature distinguishes these two solvers. At each increment, Standard implicitly solves the system of equations, whereas Explicit does it directly through an explicit dynamic finite element formulation.

These two analysis products work together with a larger environment or entity called Abaqus/CAE (Complete Abaqus Environment). CAE is Abaqus controlling system, the interface whence the user creates models, chooses analysis method, submits and monitors jobs (simulates), visualizes and evaluates results. Each of these phases is organized as an individual module making it easier to manage the entire modeling phase.

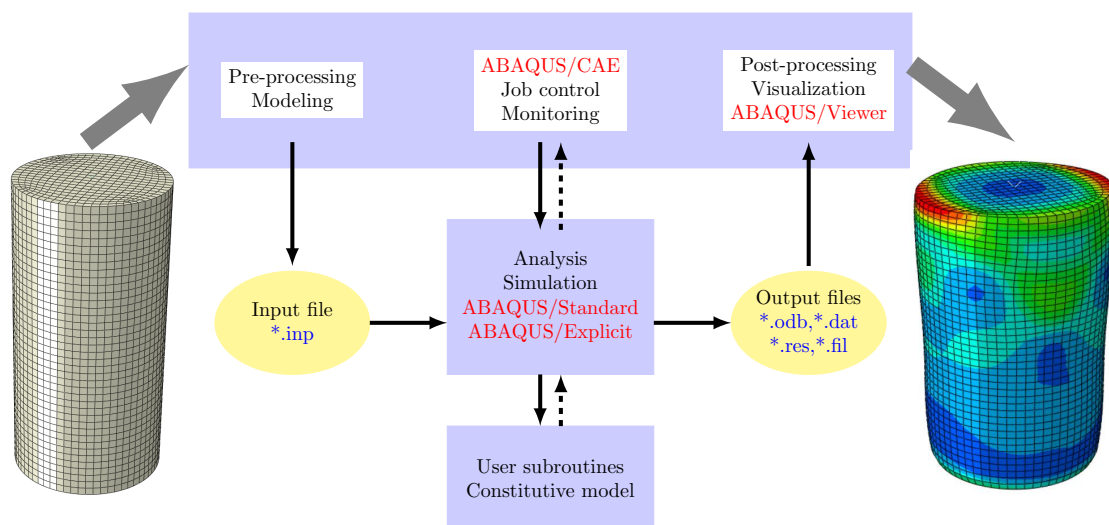


Figure B.1 Abaqus framework.

Figure B.1 shows the organization-flowchart of Abaqus framework. In a regular boundary value problem analysis, the user defines the geometry, material properties, boundary conditions, etc in the CAE, who then sends an execution command to either Standard or Explicit solvers. The chosen analysis product, then, reads the input file, performs the core

analysis and sends output database (file *.odb, *.dat, *.res, *.fil) back to CAE. Finally, the raw results generated from the analysis are post-processed by Abaqus/Viewer, a visualization subset of CAE interface.

B.2 User Subroutine: VUMAT

Abaqus/Explicit allows users to define their own constitutive model through a facility subroutine called VUMAT. This is also feasible for Abaqus/Standard, although the name of the user material subroutine is slightly different, called UMAT. This subroutine may interact with other utility subroutines or functions built-in in Abaqus. These auxiliary functions involve, for example, finding the invariants of stress and strain tensors as well as their principal values and directions. Other important subroutines include reading prescribed non-linear distribution of initial conditions (stress, pore pressure, solution-dependent state variables and void ratio) to run the analysis. All these user subroutines enable the definition of initial values according to coordinates and number for element and node variables. Users may also employ their own bank for utility functions. The VUMAT code can be written in either FORTRAN or C++ programming language.

Abaqus calls the user-material subroutine at each Gauss point for which a user-defined material behavior is assigned. Particularly for the class of problems studied here, the arrays of strain increments (STRAININC), user-material properties (PROPS) and current/updated values of stresses (STRESSOLD/STRESSNEW) and current/updated solution-dependent state values (STATEOLD/STATENEW) are passed on to VUMAT over a finite time increment, along with their corresponding dimensions. [Figure B.2](#) shows the general interface of a VUMAT subroutine code in FORTRAN language.

```

SUBROUTINE VUMAT (
C READ ONLY (UNMODIFIABLE) VARIABLES -
1  NBLOCK, NDIR, NSHR, NSTATEV, NFIELDV, NPROPS, LANNEAL,
2  STEPTIME, TOTALTIME, DT, CMNAME, COORDMP, CHARLENGTH,
3  PROPS, DENSITY, STRAININC, RELSPININC,
4  TEMPOLD, STRETCHOLD, DEFGRADOLD, FIELDOLD,
5  STRESSOLD, STATEOLD, ENERINTERNOLD, ENERINELASOLD,
6  TEMPNEW, STRETCHNEW, DEFGRADNEW, FIELDNEW,
C WRITE ONLY (MODIFIABLE) VARIABLES -
7  STRESSNEW, STATENEW, ENERINTERNNEW, ENERINELASNEW )
C
C      INCLUDE 'VABA_PARAM.INC'
C
C      DIMENSION PROPS (NPROPS) , DENSITY (NBLOCK) , COORDMP (NBLOCK,*) ,
1  CHARLENGTH (NBLOCK) , STRAININC (NBLOCK,NDIR+NSHR) ,
2  RELSPININC (NBLOCK,NSHR) , TEMPOLD (NBLOCK) ,
3  STRETCHOLD (NBLOCK,NDIR+NSHR) ,
4  DEFGRADOLD (NBLOCK,NDIR+NSHR+NSHR) ,
5  FIELDOLD (NBLOCK,NFIELDV) , STRESSOLD (NBLOCK,NDIR+NSHR) ,
6  STATEOLD (NBLOCK,NSTATEV) , ENERINTERNOLD (NBLOCK) ,
7  ENERINELASOLD (NBLOCK) , TEMPNEW (NBLOCK) ,
8  STRETCHNEW (NBLOCK,NDIR+NSHR) ,
8  DEFGRADNEW (NBLOCK,NDIR+NSHR+NSHR) ,
9  FIELDNEW (NBLOCK,NFIELDV) ,
1  STRESSNEW (NBLOCK,NDIR+NSHR) , STATENEW (NBLOCK,NSTATEV) ,
2  ENERINTERNNEW (NBLOCK) , ENERINELASNEW (NBLOCK)
C
!user coding to define constitutive relations

RETURN
END

```

Figure B.2 User-material subroutine interface in FORTRAN language.